Journal of Electronic Systems and Programming

Editorial:
8th Issue – Journal of Electronic Systems and Programming

We are delighted to announce the publication of the 8th issue of the Journal of Electronic Systems and Programming (JESP).

First of all, we would like to welcome the new Editorial Board members and we want to take this opportunity to express our gratitude to the outgoing members of the Editorial Board for their important contributions to the JESP journal over many years, and have worked hard to achieve our goals.

Numerous number of original submissions has received, all of which have gone through a rigorous review process. The accepted articles have been published in 8th issue.

Finally, we thank our reviewers and authors for their fundamental contribution to the 8th release of the Journal. We still hope authors could consider JESP to be a place where to publish their work.

Editorial Board

Table of Contents:

Control of DC Motor Using Radial Basis Function Neural Network

1

Control of DC Motor Using Radial Basis Function Neural Network

A.Shebani

College of computer technology – Zawia

amershebani@gmail.com

Abstract

The control of nonlinear systems is a fundamental problem in control engineering. This paper presents the development of a radial basis function neural network applied to the control of DC motor speed control. The proposed control scheme is used a radial basis neural network and it is implemented in MATLAB. The design requirements are achieved with the optimum number of centres being determined using K-means clustering algorithm. The optimum value for the learning factor is determined through simulation tests. Least mean square method is used to calculate the weight values for output. The proposed control scheme shows that the radial basis neural network is an effective tool to control of DC motor system.

Keywords: control, DC motor, radial basis function neural networks, centers, weights, feedforward control.

1. Introduction

Radial basis function neural network (RBFNN) has a simple architecture consisting of one input layer, one output layer and only one array of hidden nodes called centers The training of the RBF network is very fast because the learning in the hidden layer means selection of centers and widths and the learning in the output layer means selection of the weights. The RBFN has good nonlinear function approximation ability so it is widely used to solve many problems related to modeling and control of nonlinear systems. The Euclidean distance method could be employed to measure the width of the Gaussian function for RBFNN. The centres can select randomly, and using K-Means algorithm; the K-Means algorithm is reliable, simple, offers fast convergence and can handle large data sets. The weights of RBFNN can adapt using least mean square algorithm. The least mean squares (LMS) algorithm used to adapt the weights of RBFN because of its simplicity and reasonable performance [1-5].

The ability to learn is the main advantage of an artificial neural network, this characteristic is the main difference between the neural network techniques and statistical approaches [6], [7].

The most important stage during working on artificial neural network is a training of the neural network, supervised and unsupervised algorithm used to train the network, but the supervised algorithm is commonly used to reduce the error between the network output and

actual output; supervised algorithm used in this paper to control of DC motor [8].

Figure 1 shows the supervised learning algorithm, here, the network weights adjusted based on comparison between the network output and the target until the network output equals the target, where the error is computed using mean square error (MSE).
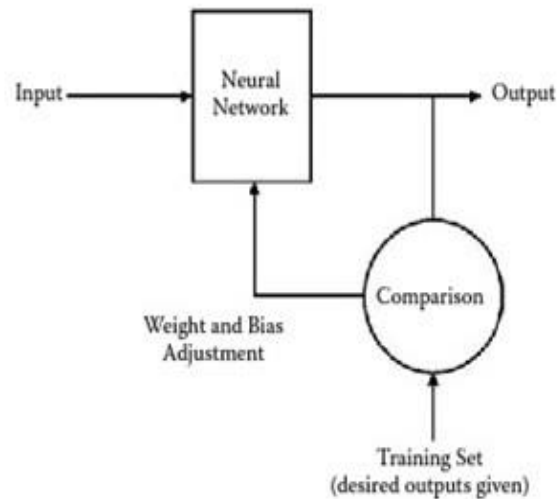
Figure 1: Supervised learning network

This paper presents the development of the control scheme using RBF neural network to control of DC motor speed control model. Supervised algorithm used in this work to train the neural network. The DC motor is developed and implemented in MATLAB.

2. Radial Basis Function Neural Network (RBFNN)

The radial basis functions neural network is a feed forward network type, and it consists of a three layers in the following order: the input layer, the hidden layer, and the output layer such as shown in Figure 2 [9].
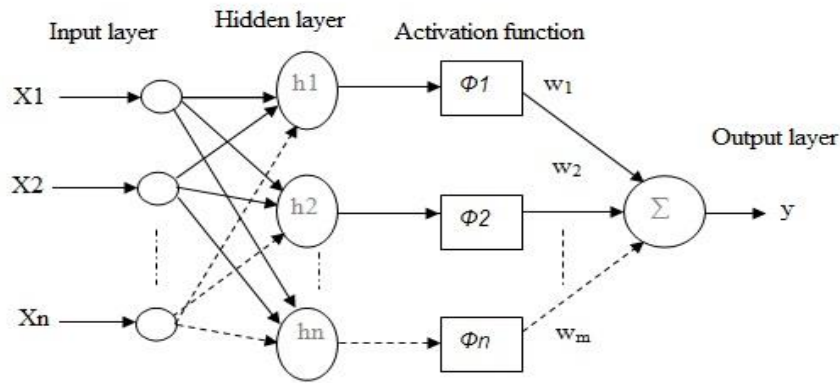
Figure 2: Radial Basis Function Network Structure [9]

$$y = \sum_{j=1}^{N} W_j \ \emptyset_j \tag{1}$$

Where y is the network output, (W_j) is the weight of the (j^{th}) node, and ($\emptyset_j$) is an activation function.

The Gaussian activation function can be written as:

$$\emptyset_j(x) = exp \frac{-\sum_{j=1}^{n}(X_i - C_j)^2}{\sigma_j^2} \tag{2}$$

$i = 1,2,3,....,n$, $j = 1,2,3,....,m$

Where $\emptyset_j$ is the output of hidden layer, X_i is the input, C_j is the center, and σ_j is the width.

The K-means algorithm steps are shown in Figure 3 [10], [11]:
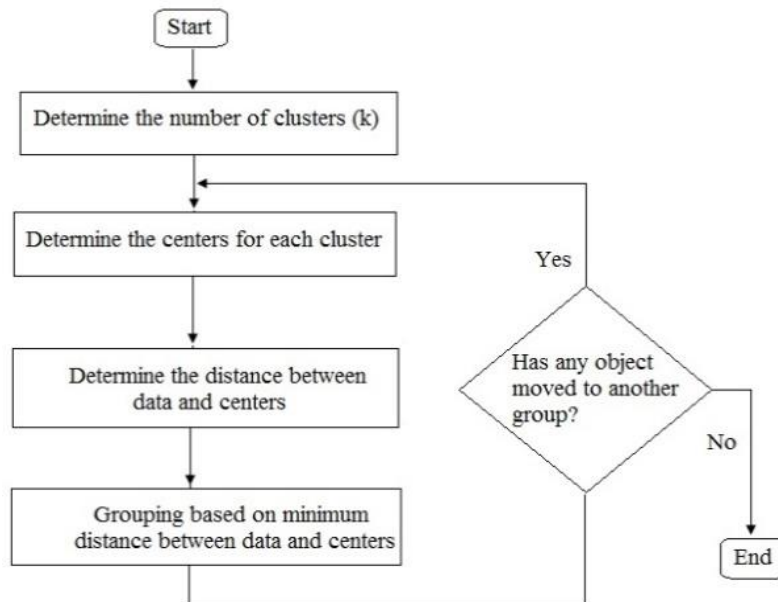
Figure 3: K-means clustering algorithm

The K-Means clustering algorithm for selecting the centres of RBFNN such as in the following steps [10], [11]:

1. From data set select random k points as initial cluster centers.

2. To the cluster centers, calculate the distance of each sample.

3. Recalculate the cluster center according, this to the clustering result.

4. According to the new center, re-cluster all the elements of the data set.

5. Step 4 repeated until the clustering does not change.

6. Final result.

The next step would be the correct selection of the width between the centers. The Euclidean distance measure is the most common method used to calculate the width of Gaussian function such as [12]:

$$E_{dist} = \sqrt{\sum_{i=1}^{n}(Xi - cj)^2} \qquad (3)$$

Where n the vector dimension, and E_{dist} is the Euclidean distance.

To adjust the weights of the network, the least mean square algorithm (LMS) is used such as [12]:

$$W(t+1) = W(t) + \mu\,(y(t) - y_m(t))\Phi^T(t) \qquad (4)$$

Where: $W(t+1)$ is the new weights, $W(t)$ is the old weights, $y(t)$ is the actual output, $y_m(t)$ is the network output, and $\Phi^T(t)$ is the Gaussian output, and μ is the learning factor, where μ normally lays between 0 to 1.

The network weights adapted until actual output becomes closer to the network output, this mean the network has completed the learning, and this step carried out normally used supervised training algorithm.

3. Control of DC motor using RBFNN

A feedforward control method used in this work to control of DC motor system is based on using the radial basis function neural network learns during feed-forward control [12], [13]. As shown in Figure 4, the controller network is placed in front of the plant, whereby the net output control signal $Uc(t)$ is an input to the plant.
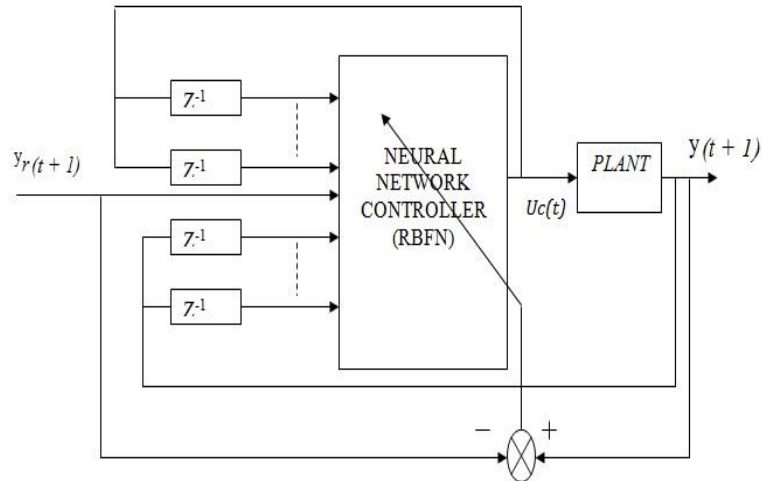
Figure 4: control configuration using RBFNN

The control signal can be realized as:

$$Uc(t) = RBFNC[X(t)] \tag{5}$$

Where: $Uc(t)$ is the control signal, while the desired reference signal is $y_r(t + 1)$:

$$X(t) = [y_r(t + 1), y(t), \dots, y(t - n + 1), U(t - 1), \dots, U(t - m + 1)]^T \tag{6}$$

The control method is considered in this work for controlling the non-linear dynamic model (DC motor) due its simplicity and robustness, especially when the proper parameters are selected.

DC motor speed control system:

The radial basis function neural network (RBFNN) used in this paper to control of DC motor. An electric equivalent circuit of the armature and the free-body diagram of the rotor shown in the Figure 5 [14].
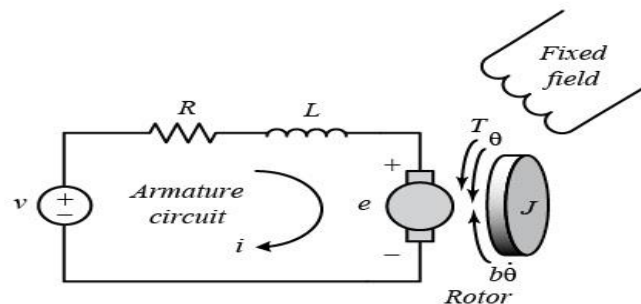
Figure 5: Electric circuit of DC motor speed control

The DC motor parameters are:

- $(J = 0.01$ kg.m^2) moment of inertia of the rotor
- $(b= 0.1$ N.m.s) motor viscous friction constant
- $(Ke= 0.01$ V/rad/Sec) electromotive force constant
- $(Kt= 0.01$ N.m/Amp) motor torque constant
- $(R = 1$ Ohm) electric resistance
- $(L= 0.5$ H) electric inductance

The following transfer function describes the DC motor speed control:

$$\frac{\dot{\theta}(s)}{V(s)} = \frac{K}{(J\,S+b)(L\,S+R)+K^2} \quad \left(\frac{rad/sec}{v}\right) \tag{7}$$

Convert the equation (7) to z domain, and then find the difference equation to the DC motor model as:

$$\dot{\theta}(k) = 1.885\,\dot{\theta}(k-1) - 0.8868\,\dot{\theta}(k-2) + 0.00009\,V(k-1) + 0.0000092\,V(k-2) \tag{8}$$

Where: $\dot{\theta}$ is the rotational speed (output), and V is the armature voltage (input).

The design requirements in this paper are:

- The speed of DC motor steady at 1 rad/sec
- Settling time 0.2 Sec
- Overshoot less than 2%

4. Simulation Tests

Test 1: Figure 6 shows the simulated results for three cases applied on the DC motor speed control system, where the centers of RBFNN selected randomly, and calculated using K-means algorithm with 3 RBFs, and 5 RBFs.
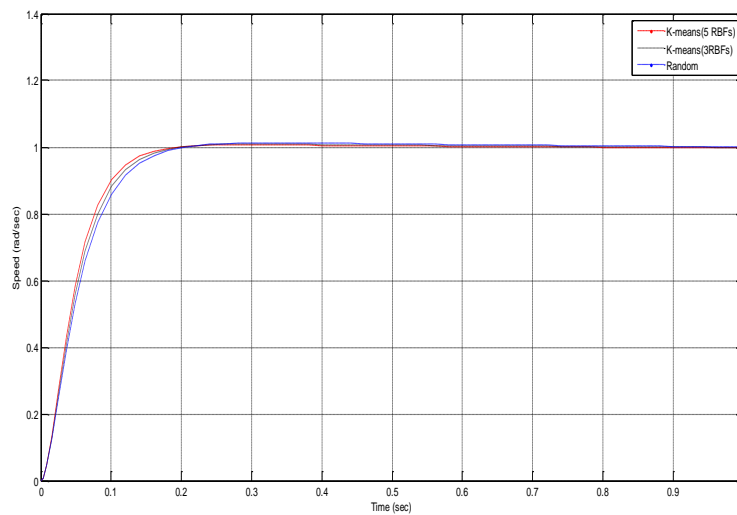
Figure 6: DC motor control using RBFNN

Test 2: Figure 7 shows the simulated results for three cases applied on the DC motor speed control system, where the centers of RBFNN selected randomly, and calculated using K-means algorithm with 7 RBFs, and 10 RBFs.
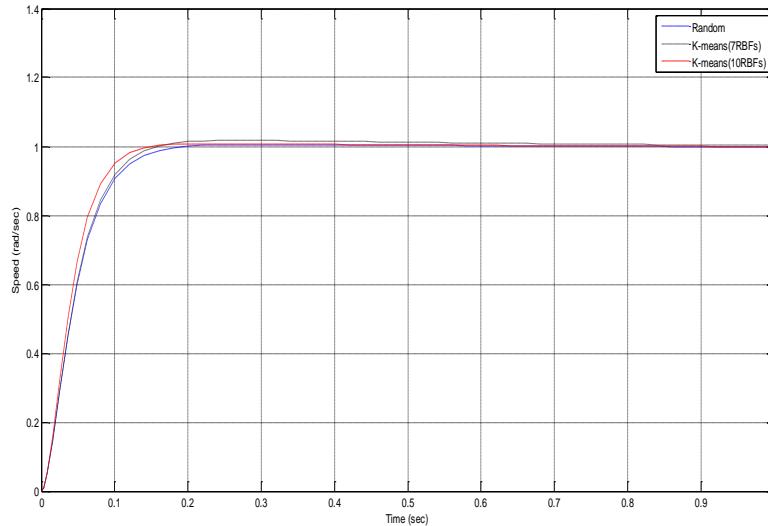
Figure 7: DC motor control using RBFNN

Simulation results shown in Figure 6 and Figure 7 exhibits good results; but the system response with random centers was slow, and the settling time was large; therefore, thee design requirements are not satisfied with random centers. The best result obtained with the case considers with 10 centers determined using K-means clustering algorithm, the system response became faster and the settling time was small (0.15 sec), furthermore, the steady value for the DC motor speed was 1 rad/sec, and the overshoot was zero, therefore the design requirements were satisfied. The case of 10RBFs is the best compared with random selection, 3RBFs, 5Rbfs, and 7RBFs; then, this situation which should be used for the selection of centers to control of DC motor using RBFNN.

5. Conclusion

This paper presents the using of radial basis function network to control of DC motor system. The optimum number of centres of RBFNN is determined randomly, and calculated using K-means algorithm. Simulation results show that the using 10 centers determined using K-means clustering algorithm is the best case which should be used for the selection of centers to control of DC motor, where the design requirements were satisfied. Finally, the simulated results show that the adaptation of the weights of the RBFN output layer has significant effects on the performance of the controller. Simulation results show that the radial basis function neural network can control of DC motor efficiently. A neural network model for control of DC motor exhibits good result that is as a result of the adaptivity of the radial basis function neural network. Therefore, the neural network model gave promising results for control of nonlinear systems.

References

[1]   L. Jinkun, "Radial Basis Function (RBF) Neural Network control for Mechanical Systems", Springer Verlag, 2013.

[2]   A. Tamer, "Direct Adaptive Control of Unknown Nonlinear Systems Using Radial Basis Function Networks with Gradient Descent and K-means", International Journal of Computer Theory and Engineering, Vol. 3, No.6, pp. 775-784, December 2011.

[3]   L. Dac, H. Nguyen and L. Luong, "Adaptive Control of Nonlinear Dynamics Systems Based on RBF Network", 2005.

[4]   S. Haykin, "Neural Networks, a comprehensive foundation", Prentice- Hall Inc., second edition, 1999.

[5]   K. L. Priddy and P. E. Keller, "Artificial neural networks: an introduction", vol. 68: SPIE Press, 2005.

[6]   D. Michie, D.J. Spiegelhalter, C.C. Taylor ,"Machine Learning, Neural and Statistical Classification" , February 17, 1994

[7]   D. Graupe ,"PRINCIPLES OF ARTIFICIAL NEURAL NETWORKS", 2nd Edition, World Scientific Publishing Co. Pte. Ltd, University of lllinois, Chicago, USA, 2007

[8]   Hanrahan and Grady, "Artificial Neural Networks in Biological and Environmental Analysis ",CRC Press, USA, 2011.

[9]   M. Sivanandam, "Introduction to artificial neural networks", Vikas Publishing House PVT LTD, 2009.

[10]   A. Bashar and M. Sung,"Initializing K-Mean using Genetic algorithms", World academy of science, Engineering and technology, 2009.

[11]   Z. Chunf and F. Zhiyi, "An improve K-means clustering Algorithm, College of computer since and technology", Jilin University, China, Journal of computational science, Vol. 10, pp. 193–199, 2013.

[12] G. Fathala, "Analysis and implementation of radial basis function neural network for controlling nonlinear dynamical systems", PhD thesis, Newcastle UK, 1998.

[13] S. George and L. Feng, "Adaptive neural network control by adaptive Interaction", Farmington Hills, Michigan 48335, Detroit, Michigan 48202, USA, 2000.

[14] C. Jongeun, "Control systems, modeling of DC motors, Department of mechanical engineering, University of British Columbia", Lecture 8, ME451, pp. 1-15, Fall 2008.

Enhancement Mammogram Image Technique For Breast Cancer Detection

2

Enhancement Mammogram Image Technique For Breast Cancer Detection

Fareda Ali Almaremi
University of Zawia, Zawia, Libya
fareda.a@zu.edu

Hend Abdelgader Eissa
Electronic Technology College Tripoli, Libya
 haseissa@icloud.com

Haitham S. Ben Abdelmula
College of Computer Technology Zawia, Libya
hsaa8383@gmail.com

Khari Amer Armih
College of Computer Technology Zawia, Libya
khari.armih@gmail.com

Abstract

In the last decades, breast cancer considered as the most common dangerous types of cancer that attack female gender in the world. In order to minimize the death rate among affected women and saves their live, the early detection process is the best solution to curbing these serious diseases. The rapid development of digital image processing techniques provides an effective role in the field of medical imaging. One of the effective techniques that used in early detection of breast cancer is a mammography method. In this paper, an optimized mammogram image technique is presented by deploying spatial domain image transformations to help the radiologist in breast cancer early detection and diagnosis. Extensive simulation outcomes demonstrated that our deployment enhancement technique offers

significantly better diagnosis and more precisely to detect lumps and various cancerous lesions affecting breast tissue.

Keywords: Breast cancer – mammogram image – spatial domain image transformation.

1. Introduction

Breast cancer has become a global nightmare that affects all female gender around the world. It is a common public health problem in many countries, and remains the leading cause of death for females aged 35–55 years [1]. Masses are the most frequent abnormalities that could be breast cancer. According to statistics of the World Health Organization (WHO), the prevalence of breast cancer among females is 1 in 8 in the United States, 1 in 12 in Europe, and 1 in 40 in Asia. Moreover, more than (500,000) females worldwide lose their lives due to breast cancer each year [2].

In Libya, breast cancer denotes of 11.9 % of total prevalence of cancers in females and is accountable for 5.3 % of mortality. Libya has a 23.2% cancer incidence rate, according to the International Agency for Research on Cancer (IARC) in 2020 [3]. According to data from the National Cancer Institute-Sabratha (NCI) for the years 2012 to 2020, there were 2,645 new cases of breast cancer in females and the majority of whom were under 35.

In order to reduce the mortality rates, the screening mammography technique is utilized to detect early warning signs and symptoms of breast cancer, such as masses and calcifications.

Studies illustration that screening technique aids to detect and diagnosis of breast cancer in early stage and increases the chances for successful treatment and complete recovery of the patient [4]. Mammography is a specialized medical imaging technique that relies on low-dose x-ray imaging for routine breast cancer screening [5].

The main issue with mammography is the visual detection of early signs of breast cancer, particularly in dense breast tissue. Furthermore, due to low count X-ray photons and electrical fluctuation, a quantum noise may appear in mammography images, which has a major influence on the quality of the images. Image processing enhancement techniques such as histogram equalization, median filters, gamma correction, and logarithmic transformation have been deployed to overcome these problems. Thus, optimizing mammography images will increase the ability to diagnose the disease. This paper shows how to apply an enhancement technique to digital mammographic images to improve their quality and assist radiologists in both screening and diagnosis phases.

The rest of the paper is structured as follows: the literature review is presented in section 2. In section 3, a brief review of the mammography technique is demonstrated. After that, the mammogram classifications are depicted in section 4. Section 5 analyzes the enhancement mammogram image schemes in detail. In section 6, the simulation setup and outcomes are explained. Finally, conclusions are made in7.

2. Literature Review

Several research studies have been conducted on image enhancement and have proposed many schemes in order to achieve the desired image quality.

An indirect contrast enhancement technique in low contrast mammographic images was proposed [6]. These methods were utilized to get the best brightness and noise removal in the photos. The performance can be improved by applying an edge preservation filter to the image.

Two-stage adaptive histogram equalization has been proposed for image improvement, as demonstrated by K. Akila [7]. The adaptive histogram equalization (AHE) uses two different histogram specifications. However, the proposed technique offers better performance in terms of enhancement measurement entropy (EME) than standard AHE.

For the purpose of improving medical images, authors in [8] presented an accomplished non-linear method utilizing discrete wavelet transform and histogram equalization. This method maintains the original image quality while improving an image's lower and higher contrast areas in both the spatial and frequency domains. In the instance of the preprocessed histogram approach, it provides better mean square error and peak signal to noise ratio results. Furthermore, discrete wavelet Transform enhanced the edges of the image.

In [9], the authors proposed a novel technique based on wavelet transformations and homomorphic filtering for the improvement and restoration of mammography images. Initially, a homomorphic filter is used to filter the approximation coefficients that the wavelet transformations produced. Then, using Gaussian and Laplacian variables, the detail coefficients of the wavelet transformations related to noise and edges are modeled. Most of the fine details of the mammogram images are retained after compressing all of the approximations and details coefficients and then enhancing the image using adaptive thresholding.

While the study presented in [10] has described an approach that used image preprocessing in the mammogram analysis due to its poor picture quality. There are various types of sifting systems available for pre-processing mammography images. Moreover, Filters are used to

improve and smoothen images, remove noise, preserve internal edges in photos, and improve picture quality.

To compensate for any acquisition challenges, the authors in [11] proposed a novel method that enhanced the digital mammography's visual representation by using a peripheral correction. The goal is to increase visualization and image quality for better evaluation. As a result, it has been established that peripheral augmentation improves visualization and will be critical in the progress of mammography computer aided diagnosis systems.

A novel breast cancer detection model described in [12]. First, median filtering and contrast limited adaptive histogram equalizations (CLAHE) are applied to the input mammography image. The preprocessed image is then segmented using the region expanding technique. The segmented image is then utilized to extract geometric properties, texture details, and gradient data. The best features are chosen using a hybrid optimization strategy. After selecting the best attributes, they are subjected to a classification technique utilizing a neural network (NN) classifier. The weight of NN is selected to improve the accuracy of diagnosis (both benign and malignant).

Finally, [13] created a unique DenseNet121-based Extreme Learning Machine Model (ELM) hybrid for diagnosing breast cancer from mammography pictures. The mammography images were preprocessed and augmented with data. After pooling and flattening the layer, the characteristics were gathered independently in the first stage of classification. The features are also input into the planned DenseNet121-ELM model's fully connected layer. An extreme learning machine model is now playing the fully connected layer. By

adjusting the weights of the extreme learning machine, the AdaGrad optimization approach increased its robustness and efficiency. The AdaGrad algorithm optimization shows a faster convergence speed than other optimization techniques.

3. Mammography Technique

Mammography is the main technique that examines female breasts by employing a low-dose x-ray system. In order to early detection and diagnosis of any change in the breast, a mammogram image is utilized [17]. To obtain images inside the body, x-ray imaging involves exposing a section of the body to a low dose of ionizing radiation.

Currently, mammography equipment is designed to reduce radiation exposure to the breast by substituting electronics for x-ray film, which transforms x-rays into images of the breast. Therefore, the radiologist can examine these pictures on a computer after they are transferred. Figure 1 depicts the basic components of a conventional mammography machine and screening of the right breast [16].
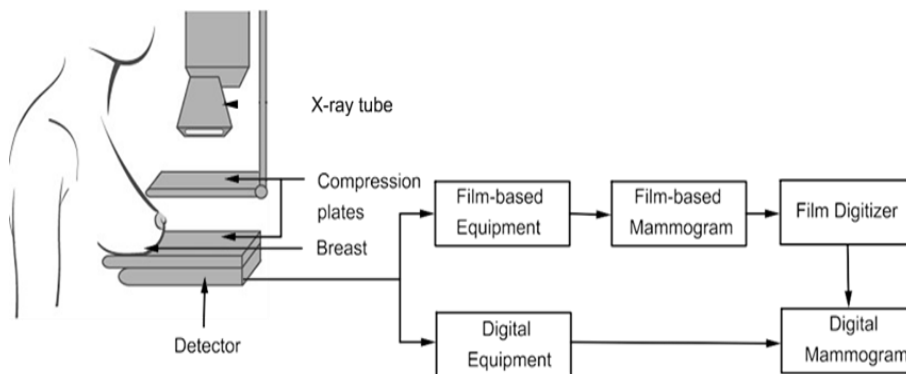

Figure 1: Main parts of mammography and right breast screening

4. Mammograms Classifications

Mammograms can be classified into two types: screening mammograms and diagnostic mammograms.

4.1. Screening Mammogram (SM)

Screening mammography periodically for a woman's breast who has no symptoms of breast cancer leads to the discovery of early breast cancer signs, which considerably increases a woman's chances of effective treatment.

4.2. Diagnostic Mammogram (DM)

A diagnostic mammogram is conducted on a woman who has a clinical finding that is abnormal, such as a breast lump or nipple discharge. Moreover, diagnostic mammography may be conducted to identify the size of the cancer.

5. Mammogram Image Enhancement Processing

In order to enhance the image's visual appeal or transform it into a format that can be analyzed by machine or human, an image enhancement process should be employed [18].

In this section, the enhancement method, which is based on the spatial domain is applied to the mammogram image to enhance it without spoiling. Spatial domain image enhancement techniques involve changing an image's pixel values to increase its visual quality [21].

Firstly, in spatial domain, a transformation function is defined for transforming the original image's pixel to a pixel in the processed image, as described in equation 1.

$$g(x) = T[f(x)] \qquad\qquad 1$$

Because this function can deal with 2-dimensional images as follows:

$$g(x, y) = T[f(x, y)] \qquad\qquad 2$$

where g (x, y) is the processed image, f (x, y) is the original image, and T is the transformation.

The transformation T is defined over the neighborhood of the point (x, y) in the original image f (x, y). This neighborhood of a point (x, y) is usually a square sub-image that is centered at the point (x, y) as exposed in Figure 2.
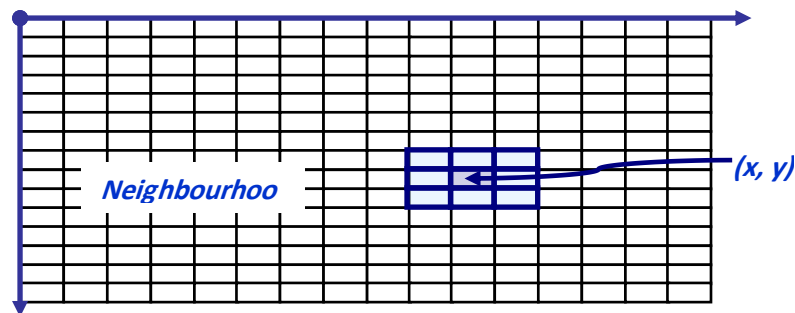
Figure 2: Mask 3x3 neighborhood around a point (x, y) in an image

For enhancing mammogram images, the proposed method is made up of seven stages: acquisition stage, negative transformation, logarithmic transformation, histogram equalization, contrast limited adaptive histogram equalization, feature extraction, and mammogram image classification.

5.1   Mammogram image acquisition

The mammogram image is sent to the computer in digital format in an acquisition phase. In order to enhance the image for further

processing, other processing methods such as morphological processing, edge detection and compression are utilized to obtain desired object of image.

5.2   Negative image transformation

If the mammogram images that outcome from the acquisition stage contain white or gray levels of information embedded in black pixels, the original image should be transformed into a negative image. In this process, all white pixels are inverted to darker and gray pixels are transformed to brighter, resulting in a negative image that makes extracting information more convenient than in the original image [19].

The negative transformation can be done through a mathematical function as follows:

$$S = (L - 1) - r \hspace{4cm} 3$$

Where $(L - 1)$ represents the maximum intensity value, (S) represents the output pixel value, and (r) represents the input pixel value.

5.3   Logarithmic image transformations

The logarithm transform consists of two kinds of transformations, log transformation and the inverse log transformation. In order to improve the contrast of objects in dark images, the logarithmic transformation is applied, while the inverse log transformation is needed to minimize the dynamic range of the mammogram image. An equation that represents the general form of the log transformation mathematically is as follows:

$$s = c * \log(1 + r) \qquad\qquad\qquad 4$$

When c is a constant and (r) is assumed to be more than zero.

5.4   Histogram Equalization

Information may be lost in areas of a mammogram image that are overly bright or dark. In order to address this issue, the female breast structure is visualized as a two-dimensional digital monochromatic image, which is represented by an array of pixels, each of which has a numerical value that indicates a gray level. Histogram equalization is then used to reduce these effects.

Mammogram images are commonly 8-bit grayscale images with a gray-level range from zero (black) to 255 (white). Consequently, the histogram measures the brightness level of images and finds whether the image has a good contrast or not.

Each pixel in the histogram is replaced during the histogram equalization process by the integral of the histogram, such as (r), which represents the image's gray level. Moreover, every pixel values in the image are continuous and normalized in the range [0,1], where zero indicates a black pixel, and one indicates a white pixel. For image processing, transformation function is applied.

$$s = T(r) \qquad\qquad\qquad 5$$

Where (r) is the intensity of the original image, s is the intensity of the process image, and T is the transformation function that satisfy two conditions.

The first condition is the $T(r)$ should be a single valued and monotonically increasing in the range $0 \leq r \leq 1$ to maintain the order of the gray levels in the processed image, while the second condition $T(r)$

must be $0 \leq T(r) \leq 1$ for $0 \leq r \leq 1$ to ensure the processed image does not lead to a pixel value which is higher than the maximum intensity value that is allowed.

5.5   Contrast limited adaptive histogram equalization

For mammogram image enhancement by using standard histogram equalization, there is a possibility of noise enhancement as well that leading to large values in the final image as a result of integration. Thus, the contrast limited adaptive histogram equalization (CLAHE) is implemented for limiting the amount of contrast enhancement at every pixel, which is achieved by clipping the original histogram to a limit. In this technique, four processing steps should be completed as follows:

1. The neighborhood of each pixel in the local histogram is being obtained.
2. The histogram should be cropped to the given limit.
3. Redistributing pixels to alter the histogram in accordance with equation 2.
4. To get the final value, integrate the histogram up to the pixel value.

5.6   Mammogram Image Feature extraction

One of the main steps that utilized for breast abnormality detection is feature extraction, which extracts unique features from the original image to use them in the classification stage. It aims to reduce an extensive amount of accurate data by computing the characteristics that can be employed to distinguish between varies samples. Due to the simplicity of the analysis of geometrical features, which consist of radius, perimeter, and area. It is utilized in the process of finding the image attributes. Generally, radiologists can recognize this feature by looking at mammograms.

5.7   Mammogram Image Classification

For mammogram image classification, one of the simplest machine learning algorithms has been applied, namely the K-Nearest Neighbor algorithm. The input for this process is the set of k closest training samples in the feature space, which are utilized by the K-NN technique to identify the features in the dataset. Furthermore, the classifier computes a weight for each feature and then multiplies it by the respective feature. Finally, all values of each feature are added in order to get a single number that can be utilized to make the final decision.

6. Results and Discussion

In this section, the enhancement mammography images are investigated for introduced spatial domain image transformations namely, negative transformation, logarithmic transformation, histogram equalization transformation, and clahe transformation.

To test the efficiency of the proposed technique, various tests are conducted to assess the impact of the proposed method on the mammogram images. These experiments are carried out on a computer equipped with an Intel Quad-Core i7-8550U CPU, and 16G RAM running on Windows 10 using MATLAB.

Negative image transformation:

Figure 3 (a) demonstrates the original image with the conservative appearance of an x-ray mammogram, where the density in the center of the breast is ill-defined. While in the Figure 3 (b), the density is better defined due to applying negative transformation technique on the conventional image.
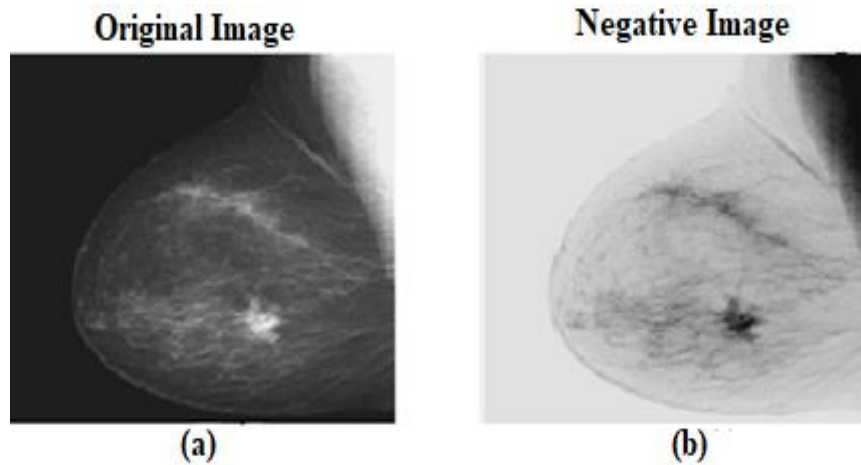
Figure 3: Negative transformation

(a) input image, (b) negative image outcome

Through this process, the inverse image was obtained by simply swapping the intensities of the pixels surrounding the central intensity of an image. This made the image easier to read and included important features like micro calcification.

Logarithmic transformations:
Figure 4 (b) shows the outcome of the log transformation performed to the original mammography image that is presented in Figure 4 (a), where the values of dark pixels in an image have been expanded.
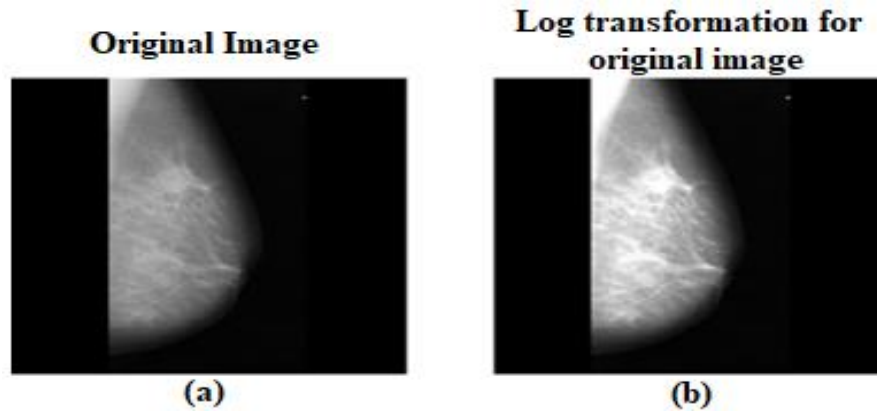
Figure 4: Logarithmic transformation
(a) Input image, (b) Logarithmic image outcome

Histogram equalization transformations:

It is employed for optimizing the contrast of a mammography image, as revealed in Figure 5. As a result, low contrast and bright improvement are applied, altering the quality of the mammography image as shown in Figure 5(b). This clearly demonstrates that the processed image contains more features than the original image.
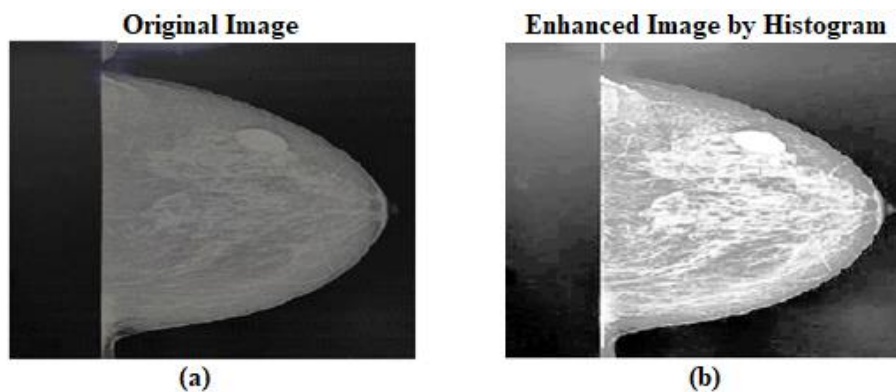
Figure 5: Histogram equalization transformation:
(a) Input image, (b) Histogram image outcome

CLAHE filter:

In Figure 6, the efficient outcome produced by passing the mammography image through the CLAHE filter has been presented, where the noise and edge shadowing effects are reduced, especially in a homogeneous area.
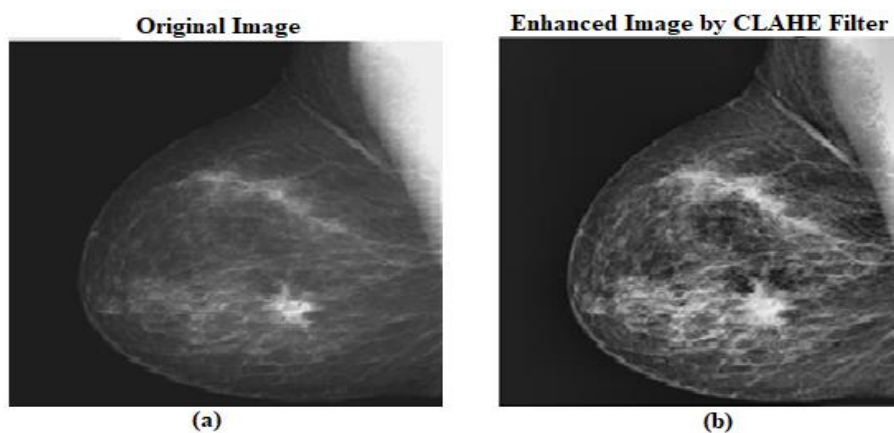
Figure 6: CLAHE filter:
(a) Input image, (b) CLAHE filter image outcome

7. Conclusion

We propose a novel framework for classifying breast cancer based on mammography pictures. The suggested framework includes critical processes, beginning with image capture and categorization. A contrast enhancement strategy is proposed in the first phase. The results were compared to the original image's deep feature accuracy. The results demonstrate that the proposed enhancement strategy improves accuracy, but the previously acquired accuracy is not met; so, a new fusion technique is presented. The proposed fusion technique was utilized to fuse the original image and augmented image features, resulting in a considerable improvement in accuracy.

References

[1]   M. Muštra and A. Štajduhar, "Segmentation Masks for the Mini-Mammographic Image Analysis Society (mini-MIAS) Database," in IEEE Consumer Electronics Magazine, 2020.

[2]   WHO, "Breast cancer: prevention and control," World Health Organization, 2016.

[3]   J. Ferlay, I. Soerjomataram, M. Ervik, R. Dikshit, S. Eser, C. Mathers, M. Rebelo, D. Forman, and F. Bray. "Globocan Cancer Incidence and Mortality Worldwide: IARC CancerBase, 2020.

[4]   P. Vineis and CP. Wild, "Global cancer patterns: causes and prevention", Lancet, 2014.

[5]   M. Heath, K. Bowyer, D. Kopans, R. Moore, and P. Kegelmeyer Jr., "Current status of the digital database for screening mammography", Kluwer Academic Publishers, 1998.

[6]   K.Akila et al. , "Mammographic image enhancement using indirect contrast enhancement techniques – A comparative study' , 2015.

[7]   A. Swaminathan and S. Gayathri,"Mammogram image enhancement by two-stage adaptive histogram equalization", Optik - International Journal for Light and Electron Optics, 2015.

[8]   Y. Rajput, "Advanced image enhancement based on wavelet & histogram equalization for medical images", Journal of Electronics and Communication Engineering, 2012.

[9]   P. Görgel, A. Sertbaş, and O. Ucan, "Wavelet-Based mammographic image denoising and enhancement with homomorphic filtering, Journal of medical systems, 2010.

[10]   J. George and A. Dhas, "Preprocessing filters for mammogram images", 2017.

[11]   N. Abubacker, et al. "An improved peripheral enhancement of mammogram images by using filtered region growing segmentation", Journal of Theoretical & Applied Information Technology, 2017.

[12]   M. Heath, et al, "Current status of the digital database for screening mammography",   In Digital Mammography, Kluwer Academic Publishers, 1998.

[13]   D'Orsi CJ, Sickles EA, Mendelson EB, Morris EA, et al. ACR BI-RADS® Atlas, Breast Imaging Reporting and Data System. Reston, VA, American College of Radiology; 2013

[14]   R. C. Gonzalez and R. E. Woods, "Digital Image Processing", Prentice Hall, 2nd edition, 2001.

[15]   E. Baidoo and A. Kontoh, "Implementation of Gray Level Image Transformation Techniques",   International Journal of Modern Education and Computer Science, 2018.

[16]   C. Feng., et al, "Log-transformation and its implications for data analysis",Shanghai archives of psychiatry, 2014.

[17]   V. Komal and S. Yaduvir, "Enhancement of Images using Histogram Processing Techniques", International Journal of Computer Technology and Applications, 2011.

[18]   Ekta Shivhare, "Breast cancer diagnosis from mammographic images using optimized feature selection and neural network architecture", 2020.

[19]   R.Pattanaik, S.Mishra, M.Siddique," Breast cancer classification from mammogram images using extreme learning machine-based denseNet121 Model. Journal of Sensors, 2022.

IoT as A Supporting Solution to Desertification

3

IoT as A Supporting Solution to Desertification

Nadia Abulgasem Bashir
Computer Department
College of Engineering Technology, Zanzor, Libya
nadia_mo2003@yahoo.com

Amer Daeri (IEEE S.M)
Computer Department
Engineering Faculty
Zawia University
amer.daeri@zu.edu.ly

Abstract

The Internet of Things (IoT) is a modern technology that has become increasingly important in all aspects of life, particularly in sustainable development programs due to its speed, cost-effectiveness, and accuracy in execution. IoT has become an effective tool to assist and accelerate the implementation of the United Nations' Sustainable Development Program. One of the most important programs that IoT can contribute to is the fight against desertification, by increasing agricultural and animal production and providing food and water for many drought-prone areas. This research focuses on how to leverage IoT to combat desertification, whether in urban or desert areas, by looking at sustainable solutions to this phenomenon while considering the economic and social factors that affect the implementation of these solutions. The study also examines some of the solutions that some countries have implemented to combat desertification, as well as the expected challenges and infrastructure requirements needed for the implementation of sustainable solutions. The results of this research

show that many countries have implemented this technology and have achieved encouraging results in both urban and desert areas. These solutions include various countries in all continents, with the most notable being the United States, China, Japan, and African coastal countries.

Keywords: IoT, desertification, sustainable development, technology.

1. Introduction

Society is currently facing significant and widespread environmental problems such as rising temperatures, extreme weather conditions, and declining air and water quality. Climate change plays a critical role in exacerbating these issues by disrupting seasonal patterns and leading to natural disasters such as floods, droughts, and forest fires. Therefore, it is essential to have systems that can continuously monitor and record data in real-time while predicting potential natural hazards.

The Internet of Things (IoT) is a technology that connects physical objects equipped with hardware such as sensors and network connectivity to facilitate the collection and transmission of measured data. The environmental field is considered an excellent candidate for implementing IoT solutions as continuous control and monitoring are efficiently facilitated through IoT adoption [1].

IoT technology enables the connection of various devices and things in a single network, allowing for the collection and analysis of data for multiple purposes, including combatting desertification. There are numerous ways that IoT can help combat desertification, since IoT devices have the potential to monitor and improve various aspects of desertification. For example, Environmental Monitoring using IoT devices can assess factors leading to desertification such as high temperatures, low humidity, and changes in soil water levels. This

information can be used to improve natural resource management and identify areas that require corrective action [2]. Similarly, Crop monitoring using IoT devices can analyze growth and productivity data of crops to improve cultivation processes and identify plant species that thrive in dry environments [3]. Water monitoring using IoT devices can help manage water resources and identify areas that require improvements in irrigation and drip irrigation [2]. Weather forecasting using IoT devices can collect and analyze atmospheric data to improve weather forecasting and identify atmospheric patterns that lead to desertification [4]. This information can improve agricultural planning and identify plant species that grow well under specific weather conditions. Additionally, IoT devices can be used to monitor environmental pollutants, noise pollution, and other harmful factors to improve overall environmental care.

The data collected and analyzed through IoT devices can also aid in improving waste management and identifying areas that require clean-up and improvement. Therefore, IoT can contribute significantly to combating desertification by enhancing natural resource management, identifying areas that need corrective action, improving weather forecasting and water monitoring, and promoting environmental stewardship. However, to achieve these benefits, the necessary infrastructure, such as installing IoT devices and communication networks, must be in place. Additionally, the design and implementation of IoT solutions to combat desertification must take into account socio-economic and environmental factors [5].

Combatting desertification can be approached in two parts, namely combating desertification in urban areas and desert areas. Therefore, social and economic factors must be considered in designing IoT solutions to ensure that the solutions meet the actual needs and challenges faced by people in urban or desert areas. Among the factors to consider are local needs, which require solutions appropriate to the

environmental and economic characteristics of the target area and compatible with local cultures and practices. Sustainability is another factor to consider, where proposed solutions must be sustainable enough to conserve natural resources and improve living conditions in the long term while maintaining the balance of the local ecosystem. Financing is also vital, and necessary investments must be made to implement solutions and ensure their long-term sustainability. Partnerships between governments, NGOs, the private sector, and local communities should be encouraged to achieve the set goals faster, while training and awareness-raising should be provided to local communities and stakeholders on issues related to combating desertification and the use of available technologies [5].

2. Economic factors

Economic factors play a crucial role in implementing sustainable solutions to combat desertification. Some of the key economic factors that must be considered include:

1. Cost-effectiveness: The chosen solutions to combat desertification must be cost-effective, affordable, and provide long-term economic benefits. This includes considering the initial investment required, ongoing maintenance costs, and potential economic returns from the solution.
2. Financing: Financing sustainable solutions is critical to their success. Governments, international organizations, private sector investors, and other stakeholders must provide financing to ensure the effective implementation of solutions and the availability of the necessary resources to maintain them over the long term.
3. Economic development: The implementation of sustainable solutions to combat desertification can help create economic opportunities and improve the livelihoods of local communities. This includes creating job opportunities and

4. Market demand: It is important to consider market demand for products or services resulting from sustainable solutions. This includes identifying potential markets and ensuring that products or services meet the necessary quality and safety standards.

5. Resource availability: The availability of resources, such as water, land, and energy, is a crucial economic factor that must be considered when implementing sustainable solutions. The chosen solutions must effectively utilize available resources and promote their use to reduce waste.

In general, economic factors are critical to the success of sustainable solutions to combat desertification. By considering these factors, stakeholders can identify the most cost-effective and efficient solutions and ensure their sustainable implementation to support economic development and improve the livelihoods of local communities.

3. Sustainable solutions

There are numerous successful examples of sustainable solutions implemented to combat desertification. According to the United Nations Convention to Combat Desertification (UNCCD) in 2013, 168 countries are affected by desertification, and by 2030, nearly half of the world's population will live in areas suffering from significant water shortages. Some of these sustainable solutions include:

1. The Great Green Wall: The Great Green Wall is a project aimed at planting a wall of trees and plants throughout the coastal region of Africa, which suffers from severe desertification. The project has already planted over 15 billion trees and aims to restore 100 million hectares of degraded land by 2030. The project not only helps combat desertification but

also provides job opportunities and economic benefits for local communities.

2. Drip Irrigation: Drip irrigation is a highly efficient method of irrigation where water is delivered directly to the plant roots, minimizing water loss due to evaporation and surface runoff. This irrigation method has been successfully implemented in areas with limited water resources, such as the Middle East and North Africa, to improve crop yields and conserve water.

3. Agroforestry: Agroforestry is a land-use system that integrates trees with crops and/or animals and provides multiple benefits, such as improving soil health, increasing biodiversity, and reducing soil erosion. Agroforestry has been successfully implemented in many areas, including the coastal region, to combat desertification and improve food security.

4. Renewable Energy: Renewable energy, such as solar and wind energy, is a sustainable solution that can help reduce reliance on fossil fuels and provide clean energy to remote areas. Many countries in the Middle East and North Africa have implemented solar energy projects to provide energy to homes and communities in rural areas.

5. Soil and Water Conservation Measures: Various measures have been implemented to conserve soil and water, such as terracing, contour plowing, and soil stabilization, to reduce soil erosion and improve soil health in areas affected by desertification.

These are just a few examples of the successful sustainable solutions implemented to combat desertification. By implementing these and other sustainable solutions, we can help protect the environment, support economic development, and improve the livelihoods of local communities.

IoT technology has been utilized to combat desertification with a range of innovative and effective solutions, such as:

1. Utilizing moisture sensors: Moisture sensors are used to measure soil moisture levels, with data being sent to the cloud for analysis and conversion into recommendations for farmers to manage water and soil. [2]

2. Implementing smart irrigation: Smart irrigation employs sensors and control devices to accurately regulate the amount of water used in irrigation. Data analysis and recommendations are provided to farmers to enhance water use efficiency. [7]

3. Conducting air monitoring: Atmospheric sensors are used to monitor weather conditions and forecasts, which aids in determining the optimal time for planting, watering, and harvesting. [4]

4. Tracking pastures: GPS devices are used to track animals in pastures and ensure they do not exceed the maximum allowable use of the pasture. This helps maintain soil health and the ecological balance of the environment. [10]

5. Utilizing agricultural robots: Agricultural robots are used to enhance farming efficiency and reduce human labor, ultimately improving water use efficiency and productivity. [11]

The effectiveness of these solutions relies on precise data analysis, effective interaction with the surrounding environment, and providing appropriate recommendations to farmers and stakeholders.

4. Examples of IoT applications to combat desertification in specific countries

There are numerous examples of IoT applications being used to combat desertification in various countries, including the United States, Japan, and parts of the Arab region. Some of these examples include:

1. The United States is a leader in the research and deployment of agricultural IoT, with over 75% of US farms using IoT in agriculture. This technology has helped American agriculture

avoid pests, diseases, natural disasters, and livestock and poultry diseases [5].

2. Japan's agricultural industry has become a model of efficiency and sustainability thanks to IoT technology. More than half of farmers in Japan are already using IoT to make up for the shortage of workers and grow more crops [12].

3. The Arab region has recently seen the emergence of an agro-technology ecosystem based on data analytics, IoT, and artificial intelligence. Efforts from both new companies and governments in the region have propelled it to the forefront of the agricultural technological revolution [13].

4. The "Green Wall Sahara" project in Algeria aims to construct a 7,000-kilometer green wall along Algeria's desert border, using IoT technologies to monitor soil moisture levels, temperatures, and soil quality to promote plant growth.

5. "The Great Green Wall" project in Africa aims to construct a green line that spans 11 African countries from west to east to combat desertification, using IoT technologies to monitor moisture, soil and water levels, and provide recommendations to farmers.

6. The "Smart Agriculture" project in China uses IoT technologies such as sensors and smart irrigation systems to improve water use efficiency in agriculture and combat desertification.

These examples demonstrate the effectiveness of IoT applications in combating desertification and improving the efficiency of agriculture and environmental conservation.

5. Using IoT technologies to combat desertification in urban areas

The application of IoT technologies can prove effective in combating desertification in urban areas, contingent upon the availability of a suitable environment for their implementation. Some solutions that

can be utilized in urban areas with IoT technologies to combat desertification include:

1. Smart gardens: Smart sensors can be used to monitor soil moisture levels, temperatures, and air quality, providing recommendations to urban growers to maintain effective irrigation and improve plant growth. [2]
2. Green roofs: Smart irrigation systems and sensors can be employed to enhance the water use efficiency of green roofs, improve plant growth, and reduce heat emitted from roofs. [7]
3. Smart trees: Smart sensors can be used to monitor soil moisture levels and the health status of urban trees, providing recommendations for tree care and improvement. [2]
4. Vertical farming: Smart vertical farming techniques can be employed in urban areas to grow indoor plants, improve water use efficiency, and provide green spaces in urban areas. [7]

These technologies can improve air quality, enhance public health in urban areas, and improve the quality of life for residents. It is important to note that the use of IoT technologies to combat desertification in urban areas requires the availability of appropriate infrastructure and resources to implement these solutions.

There are several examples of IoT applications being used to combat desertification in urban areas, including:

1. The "Smart Greenhouse" project in China utilizes IoT technologies to monitor humidity levels, temperature, and light levels in greenhouses, improving water use efficiency and plant growth. [18]
2. The "GreenRoofs" project in the United States uses IoT technologies to enhance water use efficiency in green roofs, improve plant growth, and reduce heat emission from roofs. [19]
3. The "Urban Farming" project in Japan employs IoT technologies to improve the effectiveness of vertical farming

in urban areas, improve water use efficiency, and provide green spaces in cities. [20]

These examples demonstrate the effectiveness of IoT technologies in combating desertification in urban areas, enhancing the efficiency of agriculture, and contributing to environmental conservation in cities.

6. The use of IoT technology in combating desertification in desert areas

The application of IoT technology can aid in combating desertification in desert areas through the implementation of smart irrigation systems, smart trees, smart vertical farming, and other solutions that employ smart sensors and data analysis to enhance water use efficiency and improve plant growth in the desert environment.

IoT technology for combating desertification in desert areas involves the use of smart sensors to monitor variables such as soil moisture levels, temperatures, soil and air quality, and other environmental factors. Data collected by these sensors is then analyzed by cloud computing and artificial intelligence to determine the specific requirements for water and other resources, identify changes in environmental conditions, and take action to conserve plants, trees, and crops.

1. Smart irrigation systems in desert areas utilize drip and sprinkler irrigation technology to provide water more efficiently. These systems are controlled by smart sensors that measure soil moisture levels, temperatures, and other environmental variables.
2. Smart trees are utilized in desert areas to improve productivity and enhance the surrounding environment, with smart sensors used to monitor the growth, health, and productivity of trees and provide them with necessary care.
3. Smart vertical farming is employed in desert areas to increase productivity in small spaces, with smart sensors used to

determine the precise needs of plants and provide them with necessary care.

In summary, IoT technology can be utilized to combat desertification in desert areas, improve water and other resource use efficiency, and enhance productivity and quality in agriculture and forestry in these regions. [2, 7]

The application of these solutions to combat desertification in desert areas is feasible with the provision of adequate infrastructure and resources to implement these IoT technologies.

However, the application of IoT technologies in desert areas is faced with some challenges, including:

1. Water shortage: Water is a critical challenge in desert areas, and the use of IoT technologies to combat desertification necessitates the availability of sustainable and efficient water sources to supply the required water for plant growth.
2. Harsh environment: Desert areas are characterized by severe environments and significant temperature fluctuations, necessitating the deployment of smart sensors that can withstand these harsh conditions.
3. Sustainable energy: The operation of IoT technologies requires sustainable energy, and the availability of sustainable energy sources in desert areas may pose a challenge.
4. Social challenges: The implementation of IoT projects to combat desertification in desert areas may face social challenges, such as a lack of funding or resistance to change.

Nevertheless, IoT technologies can be employed to combat desertification in desert areas through the utilization of smart irrigation systems, smart trees, smart vertical farming, and other solutions that apply smart sensors and data analysis to improve water use efficiency and enhance plant growth in the desert environment [2, 7].

Smart vertical farming offers numerous benefits in desert areas, which is I think it is very important in the Libyan case to combat desertification and this includes:

1. Efficient use of space: Smart vertical farming maximizes the use of available space in desert areas, enabling farmers to grow crops in small spaces.
2. Water conservation: Smart sensors can be used to monitor the moisture level in the soil and provide recommendations for watering, resulting in water conservation.
3. Reduced carbon footprint: Smart vertical farming can help reduce the carbon footprint associated with traditional farming practices by minimizing the use of tractors and other equipment.
4. Improved crop yield: Smart sensors can be used to monitor the precise needs of crops, enabling farmers to provide the necessary care, resulting in higher crop yields.
5. Year-round farming: Smart vertical farming enables farmers to grow crops year-round, regardless of the season or weather conditions.
6. Reduced transportation costs: Smart vertical farming eliminates the need for long-distance transportation of crops, reducing transportation costs and minimizing the carbon footprint.

In summary, smart vertical farming in desert areas offers a sustainable and efficient way to grow crops, with benefits including efficient use of space, water conservation, reduced carbon footprint, improved crop yields, year-round farming, and reduced transportation costs.

7. Challenges for sustainable solutions to combat desertification

There are numerous challenges associated with implementing sustainable solutions to combat desertification. Some of these challenges include:

1. Funding: Securing the necessary funding to implement and maintain sustainable solutions can be challenging, particularly in developing countries where resources are limited.
2. Lack of political will: The lack of political will to prioritize environmental issues and invest in sustainable solutions can hinder progress.
3. Limited knowledge and awareness: Limited knowledge and awareness of sustainable solutions and their benefits can impede effective implementation.
4. Climate change: Climate change exacerbates the problem of desertification, making it more difficult to implement sustainable solutions.
5. Land tenure issues: Disputes over land ownership and use can make it difficult to implement sustainable solutions that require collaboration and teamwork.
6. Limited access to technology and resources: The limited availability of technology and resources, such as irrigation systems and fertilizers, can make it challenging to implement sustainable solutions effectively.

Despite these challenges, sustainable solutions have been successfully implemented in various regions worldwide. Addressing these challenges requires collaboration between governments, international organizations, local communities, and other stakeholders to secure funding, create political will, increase knowledge and awareness, and provide access to technology and resources needed to implement sustainable solutions effectively.

8. IoT Infrastructure

To effectively operate IoT applications for combatting desertification, appropriate infrastructure is required, which includes:

1. Strong and reliable communication networks: IoT applications necessitate robust and dependable communication networks to ensure smooth and efficient data transmission.
2. Advanced sensors: Sophisticated and precise sensor systems are required for IoT technologies to monitor variables such as humidity levels, temperatures, soil and air quality, and other environmental factors.
3. Cloud computing: Data collected from sensors is stored in the cloud, where it is analyzed and interpreted using machine learning and artificial intelligence techniques.
4. Smart software: The use of smart software is essential for IoT technologies to analyze data, manage devices, and enhance the effectiveness of solutions.
5. Sustainable energy: The operation of IoT devices requires sustainable energy sources such as solar, wind, or hydrogen energy to ensure environmental sustainability and reduce operating costs.
6. Experts and specialists: Engineers and experts with knowledge and expertise in modern technologies, agriculture, environment, and water are required to effectively manage and operate these IoT applications.

In addition, the availability of necessary resources such as funding, training, and community support is essential for the full implementation of these solutions.

9. Conclusions

Based on this study, the following conclusions can be drawn:
The Internet of Things technology plays a crucial role in combating desertification effectively.

This technology is applicable in both urban and desert areas. Economic and social factors are essential in harnessing the potential of this technology for sustainable solutions to combat desertification. Many countries are utilizing this technology to find sustainable solutions to combat desertification and drought, such as smart irrigation, green roofs, vertical farming, and pasture monitoring. The effective use of this technology requires appropriate infrastructure, including sensors, smart software, and specialized experts. Awareness and training are crucial for the successful application and development of this technology.

10. Recommendations

To contribute to combating desertification, particularly in countries like Libya that are threatened by drought, the following recommendations should be considered:

1. State officials must allocate the necessary resources to leverage IoT technology in both urban and desert areas.
2. Emphasis should be placed on training individuals to effectively utilize these techniques.
3. Learning from the experiences of other countries with similar environmental conditions that have implemented sustainable solutions using this technology.
4. The provision of necessary infrastructure to implement sustainable solutions, which can help combat desertification and drought while also creating job opportunities in fields such as agriculture and grazing.

5. In the Libyan case, the Internet of Things technology can be employ several methods to combat desertification, such as:

   a. Smart Irrigation Systems: Smart irrigation systems use sensors to monitor soil moisture levels, weather conditions, and other factors to optimize irrigation schedules and

reduce water waste. This can help conserve water resources and prevent soil degradation.

b. Weather Monitoring Systems: Weather monitoring systems use sensors and other technology to collect data about temperature, humidity, wind speed, and other weather conditions. This data can be used to improve agricultural practices and prevent soil degradation.

c. Precision agriculture by improving agricultural practices such as planting, fertilizing and harvesting. This can help reduce water use, prevent soil degradation, and increase yields.

d. Soil monitoring systems: Soil monitoring systems use sensors and other technologies to collect data on soil moisture, nutrient levels, and other factors. This data can be used to improve agricultural practices and prevent soil degradation.

e. Livestock Monitoring Systems: Livestock surveillance systems use sensors and other technologies to track the health and behavior of livestock. This can help prevent overgrazing and other activities that can lead to soil degradation.

f. Air Quality Monitoring Systems: Air quality monitoring systems use sensors to measure levels of pollutants such as dust and particulate matter. This data can be used to develop strategies to reduce air pollution and prevent soil degradation.

References

[1] Sofia Polymeni, Evangelos Athanasakis, Georgios Spanos, Konsta ntinos Votis, Dimitrios Tzovaras, "IoT-based prediction models in the environmental context: A systematic Literature Review", SinceDirect Internet of Things Volume 20, November 2022, 100612

[2] Partha Pratim Ray, "Internet of things for smart agriculture: Technologies, practices and future direction", Journal of Ambient Intelligence and Smart Environments 9 (2017) 395–420

[3] UN environment program, "A green wall to promote peace and restore nature in Africa's Sahel region", 2023.

[4] Liu, Y., Zhang, X., Wang, X., & Li, H. (2020). IoT-based monitoring and early warning system for desertification. Journal of Sensors, 2020.

[5] Ahmed Tawfiq Jamil, " A Systematic Literature Review of Internet of Things Applications in Agriculture" Journal of Research Technology & Engineering, JRTE, October 2022

[6] Shivam Pathak , Shivam , Tarun Yadav , Ashish Gupta, "Remote monitoring of Agriculture sector using IOT", International Journal of Aquatic Science ISSN: 2008-8019 Vol 12, Issue 02, 2021

[7] Pei Yang , Lifeng Wu , , Minghui Cheng , Junliang Fan , Sien Li , Haidong Wang and Long Qian," Review on Drip Irrigation: Impact on Crop Yield, Quality, and Water Productivity in China", Water 2023, 15, 1733. https://doi.org/10.3390/w15091733

[8] Shah Fahad , Sangram Bhanudas Chavan , Akash Ravindra Chichaghare , Appanderanda Ramani Uthappa , Manish Kumar , Vijaysinha Kakade , Aliza Pradhan , Dinesh Jinger , Gauri Rawale , Dinesh Kumar Yadav , Vikas Kumar , Taimoor Hassan Farooq , Baber Ali , Akshay Vijay Sawant , Shah Saud , Shouyue Chen and Peter Poczai ," Agroforestry Systems for Soil Health Improvement and Maintenance", Sustainability 2022, 14, 14877. https://doi.org/10.3390/su142214877

[9] Saeed H Aldulaimi and Marwan M Abdeldayem, "Examining the impact of renewable energy technologies on sustainability development in the middle east and north Africa region", International Journal of Engineering Business Management, Volume 14: 1–13, 2022

[10] Bernard Ijesunor Akhigbe , Kamran Munir , Olugbenga Akinade , Lukman Akanbi and Lukumon O. Oyedele, "IoT Technologies for Livestock Management: A Review of Present Status, Opportunities, and Future Trends. Big Data Cogn. Comput. 2021, 5, 10. https://doi.org/10.3390/bdcc5010010

[11] Chrysanthos Maraveas, "Incorporating Artificial Intelligence Technology in Smart Greenhouses: Current State of the Art", Appl. Sci. 2023, 13, 14. https://doi.org/10.3390/app13010014

[12] D. Li, T. Nanseki, Y. Chomei, and J. Kuang, "A Review of Smart Agriculture and Production Practices in Japanese Large-Scale Rice Farming," J. Sci. Food Agric., vol. 1, no. 1, pp. 24–31, 2022.

[13] S. Paul, B. Sunil, and A. A. A. M. Ali, "Green IoT and sustainability in the UAE post pandemic for an eco-friendly and sustainable smart agriculture," in 2022 8th International Conference on Information Technology Trends (ITT), 2022, pp. 124–129.

[14] N. Alrobah and N. Khan, "Proposing Guideline for Conclusive use of Smart Agriculture Application in KSA," in 2020 International Conference on Computing and Information Technology (ICCIT-1441), 2020, pp. 1–5.

[15] K. E. Abd El Mowla and H. H. Abd El Aziz, "Economic analysis of climate-smart Agriculture in Egypt," Egypt. J. Agric. Res., vol. 98, no. 1, pp. 52–63, 2020.

[16] S. El-Shawa, M. Alzurikat, J. Alsaadi, G. Al Sona, and Z. A. Shaar, "Jordan Space Research Initiative: Societal Benefits of Lunar Exploration and Analog Research," Acta Astronaut., vol. 200, no. 2, pp. 574–585, 2022.

[17]   S. Note, "The role of food and agriculture for job creation and poverty reduction in Jordan and Lebanon," World Bank Agric. Sect. Note, vol. 1, no. 1, pp. 11–20, 2018.

[18]   Pinar Kirci *, Erdinc Ozturk and Yavuz Celik, "A Novel Approach for Monitoring of Smart Greenhouse and Flowerpot Parameters and Detection of Plant Growth with Sensors", Agriculture 2022, 12, 1705. https://doi.org/10.3390/agriculture12101705

[19]   Giouli Mihalakakou , Manolis Souliotis , Maria Papadaki , Penelope Menounou , Panayotis Dimopoulos , Dionysia Kolokotsa , John A. Paravantis , Aris Tsangrassoulis , Giorgos Panaras , Evangelos Giannakopoulos , Spiros Papaefthimiou," Green roofs as a nature-based solution for improving urban sustainability:Progress and perspectives", Renewable and Sustainable Energy Reviews ,Volume 180, July 2023, 113306

[20]   Soojin Oh and Chungui Lu, "Vertical farming - smart urban agriculture for enhancing resilience and sustainability in food security", The Journal of Horticultural Science and Biotechnology 2023, Vol. 98, No. 2, 133–140

Design of Microstrip MIMO Antenna for X-band

4

Design of Microstrip MIMO Antenna for X-band

Prof. Marai M. Abousetta
department of electronics and communication engineering
The Libyan academy
Gianzur, libya
m. Abousetta@academy.edy.ly

Eiman A. Wahman
department of electronics and communication engineering
The Libyan academy
Gianzur, libya
eng94emy@gmail.com

Abstract

Microstrip patch antennas are used in satellite imaging systems, wireless communication equipment, military radios, GPS (Global Positioning System) and GSM (Global System for Mobile Communications) applications.   This paper describes rectangular patch antennas. It is designed for a frequency of 10.25 GHz, and is used for X-band applications. The antenna consists of an FR4 substrate, with a dielectric constant of 4.3 and a small strip line is used as the designer's air feed technique. The antenna performance at 10.25 GHz was established, several designs were implemented, and the return loss, bandwidth, gain and directivity were optimized. The best results were obtained in the Two-Element design, where the return loss was -36.686 dB, the bandwidth was 2050 MHz, and the gain was 7.13 dB Also, when simulating a 2*4 antenna, successful results were obtained, as the gain value was 10 dB and the bandwidth was 791 MHz Simulation results were obtained using CST Studio Suite software.

Keywords: Micro-strip, x-band, Patch, VSWR, Return loss.

1. Background

A micro-strip Multiple-Input Multiple-Output (MIMO) antenna is a type of antenna system used in wireless communication applications to enhance the performance and capacity of the wireless link. MIMO technology uses multiple antennas at both the transmitter and receiver ends to improve data throughput, increase spectral efficiency, and enhance signal quality by exploiting the spatial dimensions of the wireless channel.

A micro-strip MIMO antenna consists of an array of micro-strip antenna elements integrated onto a single substrate.

Each antenna element operates independently and is designed to radiate and receive electromagnetic waves in a specific pattern. The elements are placed close to each other, allowing for spatial diversity and exploiting the multi-path propagation characteristics of the wireless channel.

The micro-strip MIMO antenna design offers several advantages. First, it provides spatial multiplexing, enabling multiple data streams to be transmitted and received simultaneously using the same frequency band. This results in higher data rates and improved system capacity. Second, it offers diversity gain by exploiting the spatial diversity of the antennas, mitigating the effects of fading and improving the reliability of the wireless link. Third, the micro-strip configuration allows for compact and low-profile antenna designs, making them suitable for integration into portable devices and compact wireless systems.

The design of a micro-strip MIMO antenna involves careful consideration of various factors, including the operating frequency, bandwidth, gain, radiation pattern.

Optimization techniques, such as impedance matching, radiation pattern shaping, and isolation between the elements, they are used to obtain the desired performance.

2. Review of Previous Works

The antenna is designed with a copper patch and ground layer design. The antenna is designed to consist of a rectangular patch with a small strip with a probe feed and a ground plane marked in the form of an inverted U-shaped printed slot used for 4 different frequencies. The following results were obtained: a return loss of -15.71 dBm at 6.72414 GHz, -26.33 dBm at 8.27 GHz, -20.79 dBm at 11.38 GHz, and -14.46 dBm. At a frequency of 14.48 GHz. This slot-coupled antenna for satellite communications covers the C and X [3].

This paper presents the rectangular patch antenna.

In this paper high gain micro-strip array antennas have been designed and analysed for X band RADAR application. The array elements are excited by using inset feeding technique. Interestingly, all the array antennas are tuned exactly at centre operating frequency of 10 GHz. Rogers RT/duroid 5880™ having relative permittivity of 2.2 has been used as substrate for all the array antennas. The results show that the studied antenna array attained an operating band ranging from 9.77 GHz – 10.15 GHz with a bandwidth 380 MHz It also revealed that the proposed 2×4 element array achieved a peak gain of 15.5 dB, a directivity of 15.82 dBi and a return loss of – 30.27 dB Beam steering antenna shows return loss of -33.28 dB, very good VSWR of 1.04 and high bandwidth of 880 MHz .The ANSYS high frequency structural simulator (HFSS) has been used to perform all the simulations works. [4].

In this study, an E shaped micro-strip patch antenna is proposed. Which is designed using FR4 - epoxy substrate. The designed antenna has a return loss of -29.21 dB and works with X band. The design is

simulated using a software tool called HFSS (High Frequency Structure Simulator). The antenna has been designed for 10.3 GHz frequency applications and the return loss, VSWR and the radiation plot of the designed antenna has been evaluated. The aim is to achieve a high directivity with better gain and reduced losses particularly for X band applications [5].

In this study, micro-strip antenna design operating at 10 GHz frequency for X band applications has been made. X band is used for air traffic control, weather traffic control, vessel traffic control, defence tracking and vehicle speed detection, terrestrial communications and networking, space communications and amateur radio. HFSS program was used in antenna design. AWR program was used to find transmission line parameters. In addition, MATLAB program was used to calculate some parameters. First of all, information is given about the working principle of the antenna, the selected dielectric layer and the working frequency. Schematic drawings of the designed antenna were made from above and from the side. S11 reflection coefficient magnitude graphs are drawn below and above the operating frequency. The radiation pattern is drawn for the E-plane and H-plane at the operating frequency. 3-D (dimensional) plot of antenna gain at operating frequency is drawn [6].

3. Antenna Design

Several designs have been made for antennas that operate within the X band. Single element type, 2×2, 1×2, 1×4 and 2×4 antennas were designed and analyzed via CST software.

Using a program from CST Studio Suite, the antenna was designed. The design components were displayed, namely the dimensions of each layer, the materials it is made of, and the way the feeding process was done, to obtain some parameters such as VSWR, return loss, directivity, gain, and bandwidth. The ground layer is considered the

basis for the design. The second layer is the substrate and is connected to the ground. Choosing the type of substrate is very important. An FR4 insulating material was used. The relative permittivity value is 4.3 and the dielectric loss value is 0.02. The last layer is the patch emission antenna. The feeding method used is micro strip line feeding.

3.1 Design of Microstrip single Patch Antenna

 The antenna was designed using (CST) software. The dimensions for rectangular patch to operate at 10.25 GHz frequency. Choose a suitable insulating substrate material and determine its dimensions using the Micro-strip antenna program to be the same as the dimensions of the ground layer by entering the material permittivity value and frequency, to give me the width and length value of the substrate layer and the floor layer. in addition to Determine the height of the substrate (H) so that it is suitable for the design, and calculate the appropriate patch dimensions (width and length) using some mathematical equations (1) and (2).

Determine the feeding method and choose the appropriate feeding It is suggested to design the antenna for better performance by adding another patch. Performance is also improved by making differences in the inset feed to obtain greater matching between the feed line and the patch.

Hence, the suggested antenna gives better results for both variables such as improved gain, efficiency and bandwidth.

Location.

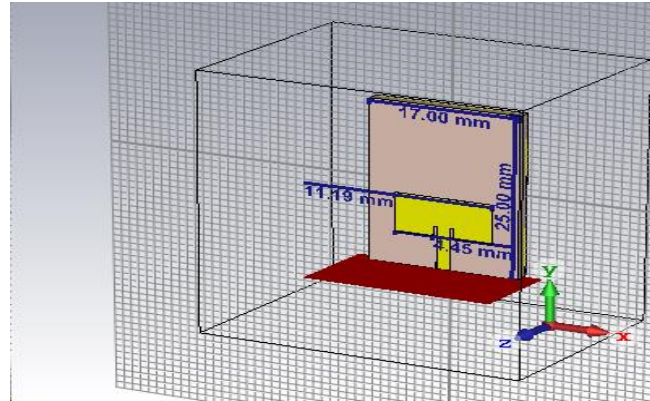$$Lg = L+6h \tag{1}$$

$$Wg = w+6h \tag{2}$$

Figure 1: 3D design of Micro-strip Single Patch Antenna

The Table I shows the measurement parameters.

TABLE I. DIMENSIONS OF THE ANTENNA

parameter	Value in mm
Length of the ground	Lg=15.81
Length of the substrate	LS=15.81
Length of the patch	Lp=6.33
Width of the ground	Wg=18.46
Width of the substrate	Wg=18.46
Width of the patch	Wp=8.98
Thickness of the ground	t=0.035
Thickness of the substrate	hs=1.58
Thickness of the patch	hp=1.615

Using the Microstrip Line program, the length and width of the feed line are calculated by entering an impedance value equal to 50 ohms. The following table shows the dimensions.

TABLE II. MEASUREMENT OF THE FEED LINE

parameter	Value in mm
Length of the feed line	Lf=4.04
Width of the feed line	Wf=3
Thickness of the feed line	h= 1.615

The schematic antenna is shown in Figure 1 as being composed of The ground is in the first layer, and the substrate is placed between the ground layer and the last layer, which is the patch with a conductive patch on the upper side.

3.2 Design of Microstrip two Patch Antenna

The antenna design was proposed by adding another correction. The antenna was designed to consist of two patches and an individual feeding technique was used for each patch. Hence, the proposed antenna provides better output in improving gain, directivity and efficiency.
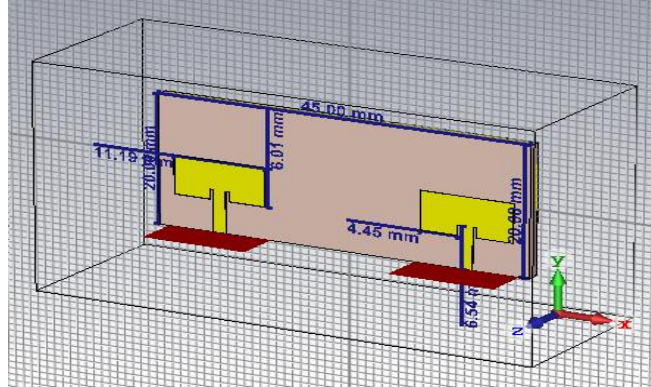
Figure 2: 3D design of Micro-strip Two Patch Antenna

TABLE I I I: DIMENSIONS OF THE ANTENNA

parameter	Value in mm
Length of the ground	Lg=20
Length of the substrate	Lg=20
Length of the patch	Lp= 6.013
Width of the ground	Wg=45
Width of the substrate	Wg=45
Width of the patch	Wp= 11.19
Thickness of the ground	t=0.035
Thickness of the substrate	hs=1.58
Thickness of the patch	hp=1.615

Length of the feed line	Wf=1.5
Width of the feed line	Lf=5
Thickness of the feed line	h=1.615

3.3 Design of Microstrip two Patch Antenna and One Port

The 1×2 elements micro-strip array antenna has been designed by using two elements was proposed by adding another patch. The dimensions of the patches were designed according to the table, a spacing of is used between two successive elements of the array antenna to reduce mutual coupling effects, the spacing between two patches is of 11 mm. Internal changes were made to the feed to obtain a greater match between the feed line and the patch. The antenna was designed to consist of two patches and a co-feeding technique was used. Hence, the proposed antenna provides better output in improving gain, directivity and efficiency. The following table displays measuring parameters.

TABLE IV: DIMENSIONS OF THE ANTENNA

parameters	Value in mm
Length of the ground	Lg=22
Length of the substrate	Lg=22
Length of the patch	Lp= 5
Width of the ground	Wg=22.5

Width of the substrate	Wg=22.5
Width of the patch	Wp= 7.77
Thickness of the ground	t=0.035
Thickness of the substrate	h=1.58
Thickness of the patch	h=1.615
Length of the feed line	Wf=1.5
Width of the feed line	Lf=5
Thickness of the feed line	h=1.615
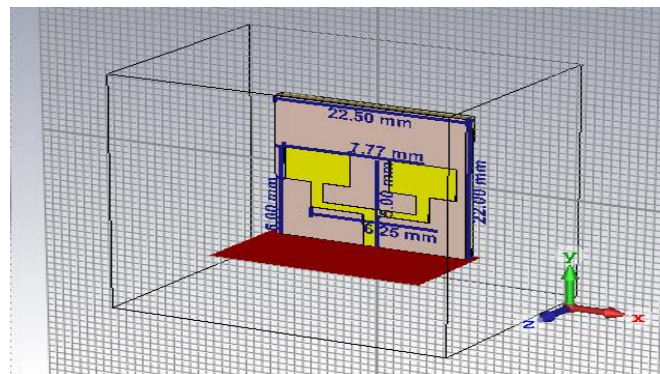
Figure 3: 3D design of Micro-strip Two Patch Antenna and one port

3.4 Design of Microstrip four Patch and one port Antenna

It is proposed to design a small chipset of 1×4 elements by adding other patches. Performance is also improved by making internal feed changes for a greater match between feed and patch line, the length

and width of the feed line are entered Adjusted for better resistance matching. The antenna is designed to have four patches and one feed port. The company's proprietary nutrition method is a method used to activate all elements, It was used in this design. The patch elements are connected using a small tape line, the patch elements are connected using a quadrant Wavelength micro-strip line and T-shaped power divider.

The width of the feed lines 50 ohm. The following table displays the measurement parameters obtained after the procedure Optimization process.

TABLE V: DIMENSIONS OF THE ANTENNA

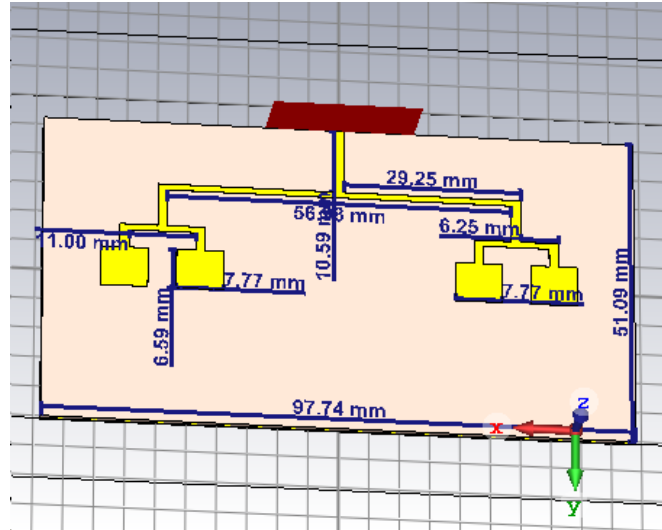| parameters	Value in mm
Length of the ground	Lg= 51.09
Length of the substrate	Lg= 51.09
Width of the ground	Wg= 97.74
Width of the substrate	Wg= 97.74
Thickness of the ground	t=0.035
Thickness of the substrate	h=1.58
Thickness of the patch	h=1.615
Length of the feed line	Wf=1.5
Width of the feed line	Lf=10.59
Thickness of the feed line	h=1.615

Figure 4: 3D design of Micro-strip four Patch Antenna And one port

3.5 Design of Microstrip four patch and two ports antenna

The antenna design was proposed to add other corrections to improve performance, in addition to making internal changes to the feed to achieve greater matching between the feed and the correction line, the impedance of the feed lines 50 ohm. The antenna is designed to have two feed lines. The following table displays measuring parameters.

TABLE VI: DIMENSIONS OF THE ANTENNA

parameters	Value in mm
Length of the ground	Lg=22
Length of the substrate	Lg=22
Length of the patch	Lp= 5

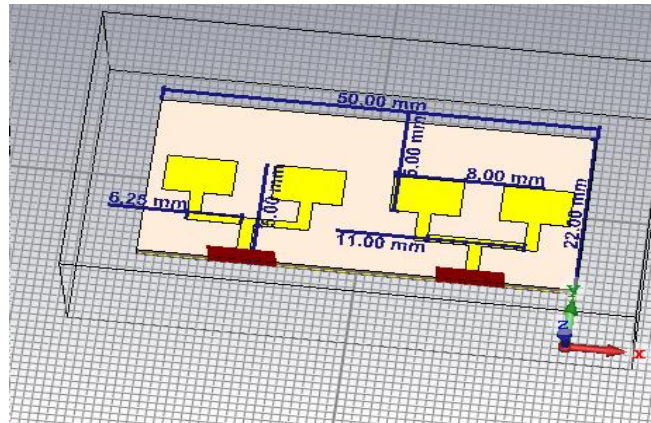| Width of the ground	Wg=50
Width of the substrate	Wg=50
Width of the patch	Wp= 8
Thickness of the ground	t=0.035
Thickness of the substrate	h=1.58
Thickness of the patch	h=1.615
Length of the feed line	Wf=1.5
Width of the feed line	Lf=5
Thickness of the feed lin	h=1.615

Figure 5: 3D design of Micro-strip four Patch Antenna and Two port.

4. Simulation Result Analysis

Using the CST program, the proposed antenna was built and simulated, and results were obtained. It is shown by analysis how different parameters affect the frequency. Depending on the length of the correction, it has been shown that the operating frequency starts to decrease, and as the length of the correction decreases, it is observed that it starts to climb. The resonant frequencies move according to the ever-changing patch magnitude. The required resonance frequency is 10.25GHz after adjusting for patch length and other variables.

4.1 Simulation and Analysis single element Micro-strip single Patch Antenna

The value of S11 is relative to Antennas the reflection coefficient and represents the value of power reflected by the antenna.

The antenna shows return loss of (-53.460dB) and less than -10dB at the operating frequency of 10.248GHz, which means that power has been delivered to the antenna.
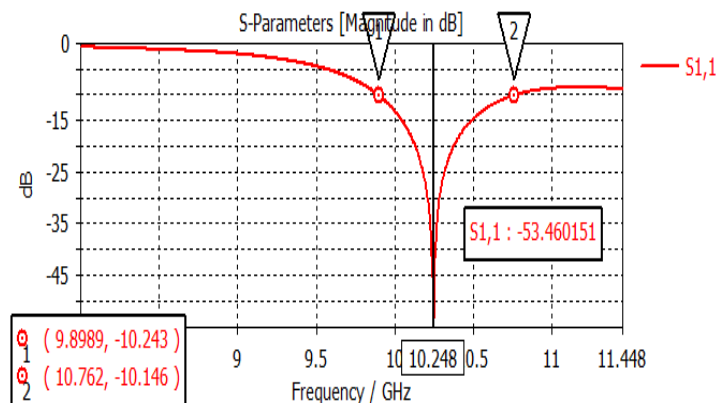

Figure 6: S-Parameters of the designed Patch Antenna.

$$Bandwidth = FH\text{-}FL \qquad\qquad (3)$$

The bandwidth value was calculated using Equation No. (1), and its value is equal to (0.8631GHZ), Equivalent 863.1MHz as shown in Fig.6.
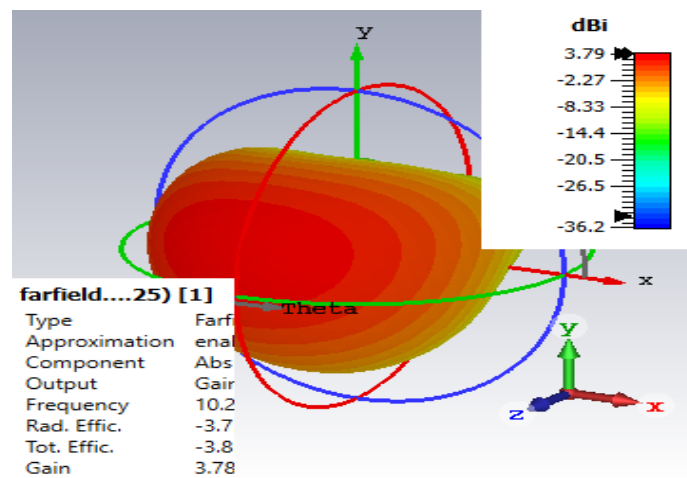

Figure 7: Gain of the designed Patch Antenna.

The antenna gain value is evidence of the radiation efficiency. The obtained gain value is equal to (3.79dB), while the antenna directivity is the amount of radiation that it radiates and directs in one direction. The obtained directivity value is equal to (7.51dBi), at the operating frequency of 10.25 GHz.
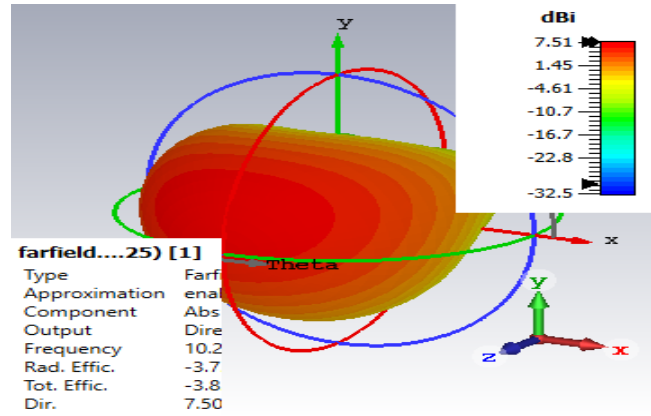
Figure 8: Directivity of the designed Patch Antenna.

The VSWR value is important to be between 1 and 2 to ensure that the antenna and feed line match.
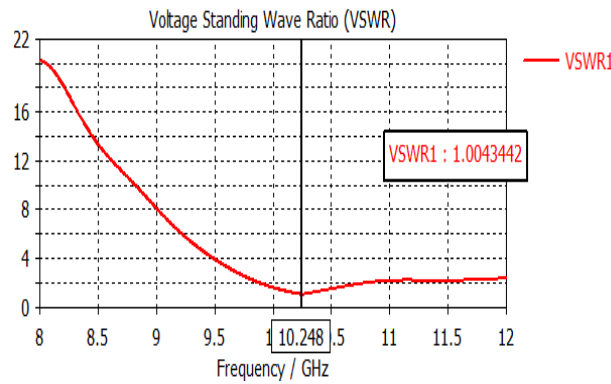

Figure 9: VSWR of the designed Patch Antenna.

According to Figure 9 of the curve, we notice that the value of VSWR is equal to (1.004), which means that the reflection coefficient value is very weak.

The value of the total efficiency is equal to (-3.828dB), and the radiation efficiency value is (-3.71dB).

4.2 Simulation and Analysis 2 x 2 element Microstrip Patch Antenna

When designing two patches at 10.25 GHz, the S11 value for the antennas is represents the amount of energy reflected by the antenna. The array its return loss to (-36.686dB) at the same centre frequency of 10.34GHz, and less than -10dB of which means that power has been delivered to the antenna.
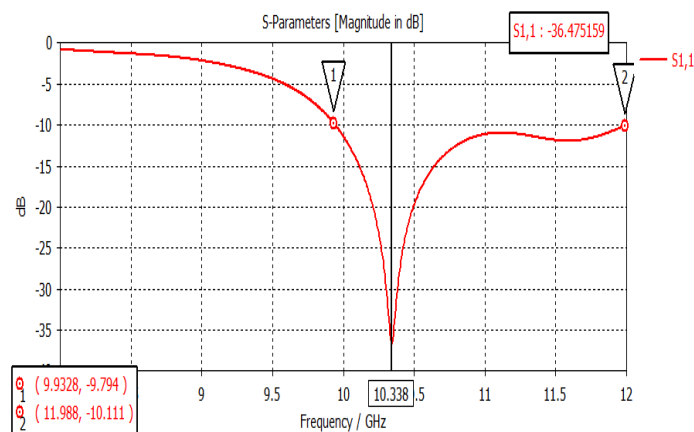

Figure 10: S-Parameters of the designed Two Patch Antenna

The bandwidth value was calculated using Equation No. (1), and its value is equal to (2.05GHZ).

The frequency ranges at which the antenna operates is from 9.9328 GHz to 11.988 GHz.

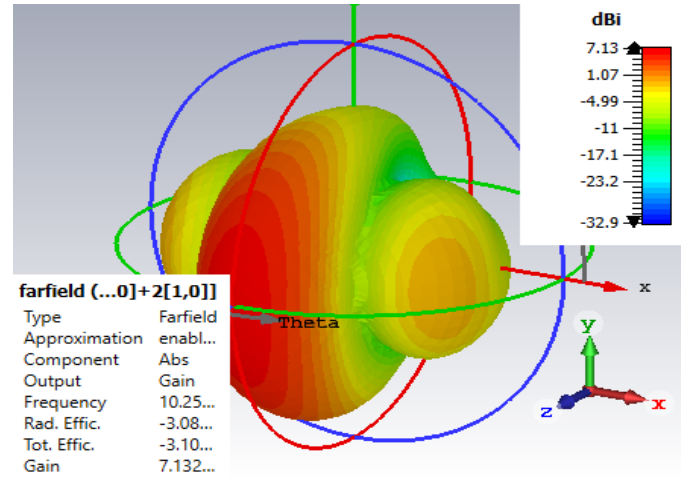This means it has a wide bandwidth of 2050MHz.

Figure 11: Gain of the designed two Patch Antenna.

As for the value of gain, it is equal to (7.13 dB), and the value of directivity is equal to (10.2dBi).
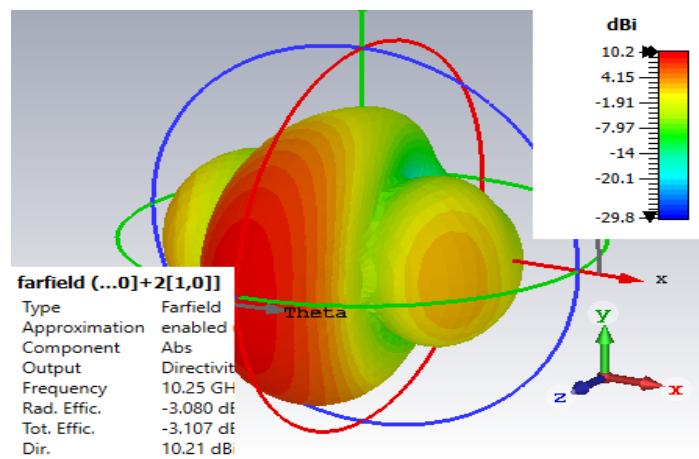

Figure 12: Directivity of the designed Two Patch Antenna.

From the curve, we notice that the value of the VSWR at the operating frequency is equal to (1.029), and this means that the value of the reflection coefficient is very small.
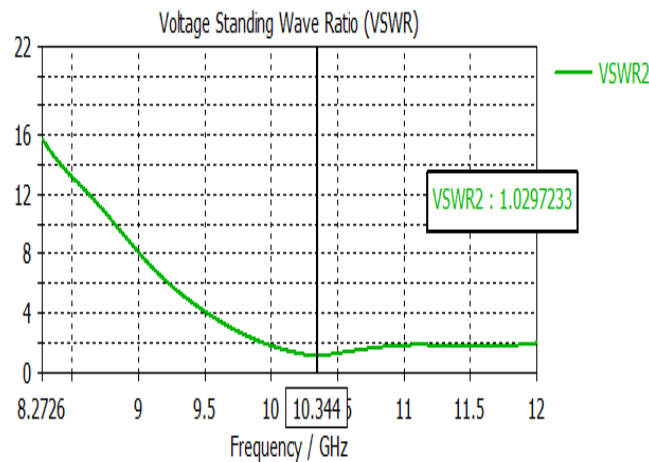

Figure 13: VSWR of the designed Two Patch Antenna

The value of the total efficiency is equal to (-3.107dB), and the radiation efficiency value is (-3.080dB).

4.3 Simulation and Analysis 1 x 2 element Microstrip Patch Antenna

Fig. 15 shows the S-parameter curve. When four 10.25GHz patches are designed and fed into a single feed line, the S11 value of the antennas is the represents the amount of power reflected by the antenna. When the S11 is equal (-25.494dB) and less than -10dBm at the operating frequency of 10.37GHz, it means that power has been applied to the antenna.
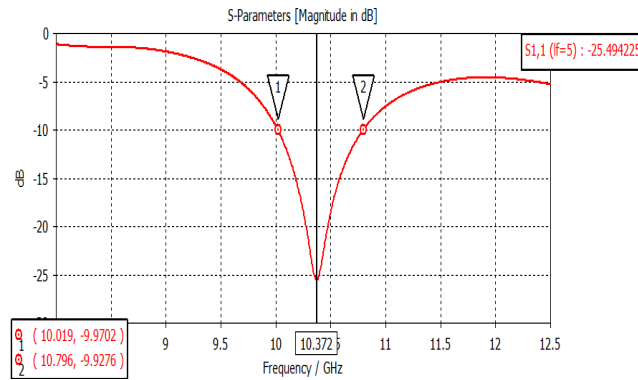
Figure 14: S-Parameters of the designed Two Patch Antenna and one port

The bandwidth value was calculated using Equation No. (1), and its value is (0.777 GHz).

From the curve we notice that the antenna radiates a signal over a frequency range, It ranges from 10.019 GHz to 10.796 GHz with an operating frequency of 10.25 GHz. The bandwidth of the array antenna is 777 MHz.
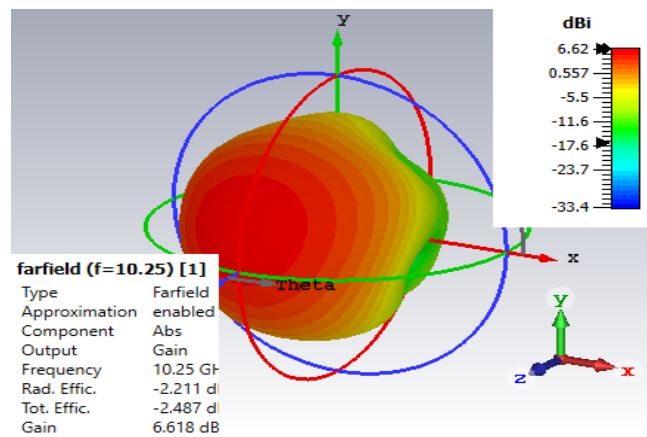

Figure 15: Gain of the designed two Patch Antenna and one port

Antenna gain is evidence of radiation efficiency. The gain value is equal to (6.62 dB). The value of directivity is equal to (8.83dBi).
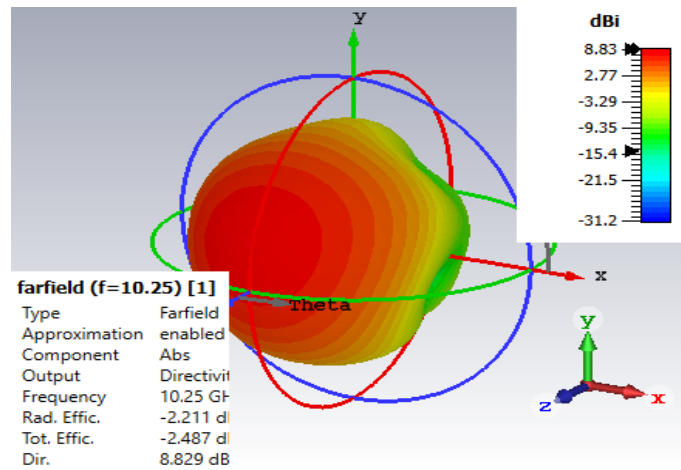

Figure 16: Directivity of the designed Two Patch Antenna and one port
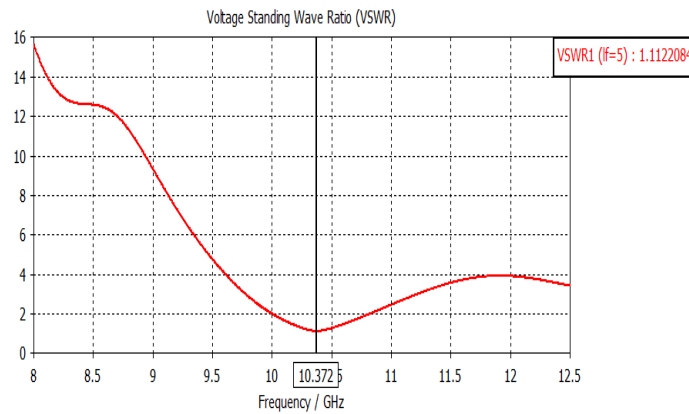
Figure 17: VSWR of the designed Two Patch Antenna and one port

From the curve, we notice that the value of the VSWR at the operating frequency is equal to (1.112), A VSWR value between 1 and 2 means that there is a physical match between the antenna and the feed line.

The value of the total efficiency is equal to (-2.487dB), and the radiation efficiency value is (-2.211dB).

4.4 Simulation and Analysis 1 x 4 element Microstrip Patch Antenna

The return loss of (-21.34dB) was obtained at 10.66 GHz.

It operates over 10.486 GHz – 10.904 GHz frequency range.
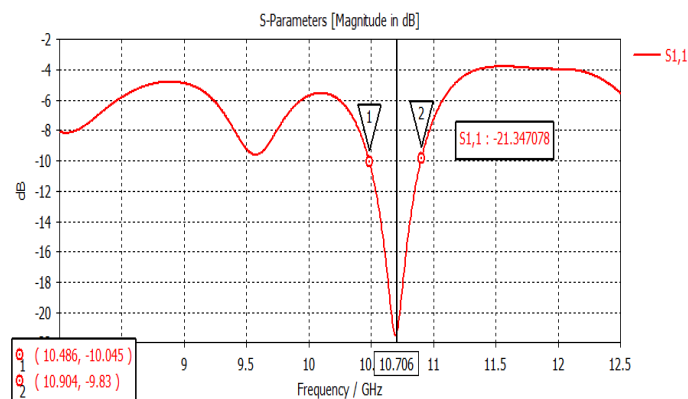
Figure 18: S-Parameters of the designed Four Patch Antenna and one port

The bandwidth value was calculated using Equation No. (1), and its value is (0.418 GHz). The bandwidth of 418 MHz.
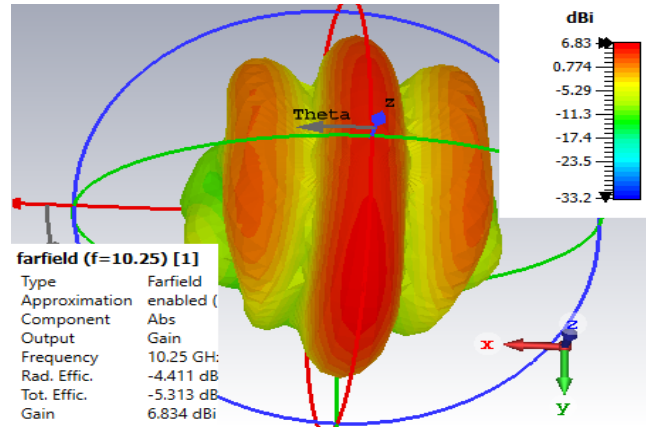
Figure 19: Gain of the designed four Patch Antenna and one port.

The gain and directivity of the suggested 1 x 4 antenna is (6.83 dB) and (11.2 dBi) at the frequency of 10.25 GHz.
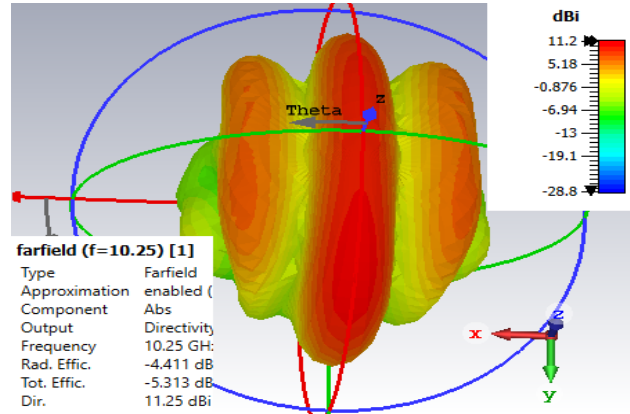
Figure 20: Directivity of the designed Four Patch Antenna and one port.

The curve shows a very good VSWR value of 1.18 (Figure 21).
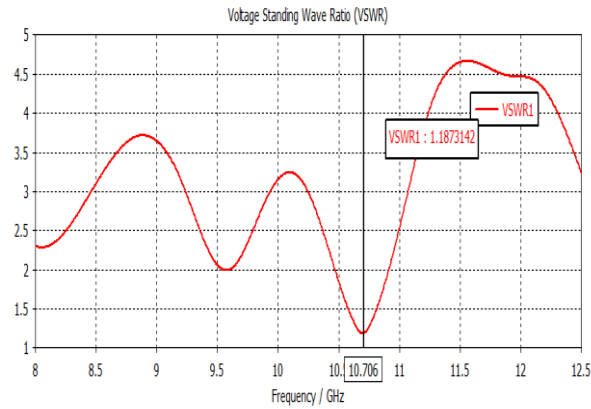
Figure 21: VSWR of the designed four Patch Antenna and one port.

The value of the total efficiency is equal to (-5.313dB), and the radiation efficiency value is (-4.230dB).

4.5 Simulation and Analysis 2 x 4 element Micro-strip Patch Antenna

When the S11 is equal (-22.404dB) and less than -10dBm at the operating frequency of 10.45GHz, it means that power has been applied to the antenna.
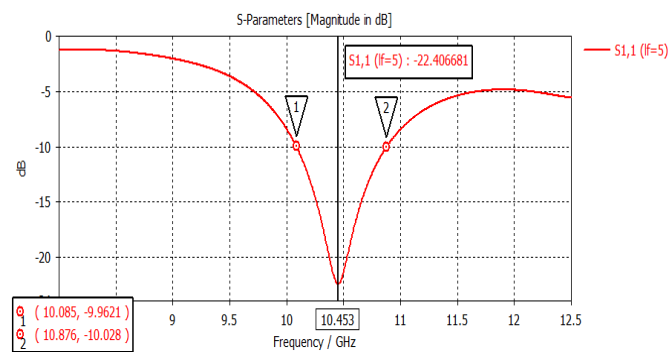
Figure 22: S-Parameters of the designed four Patch Antenna and two port.

When $S11$ is plotted between 791 MHz below and above the determined operating frequency of the antenna 10.45 GHz, as seen in Figure .23. the bandwidth at -10 dB is found as in equation 1. The bandwidth value was calculated using Equation No. (1) and its value is (0.791GHz).
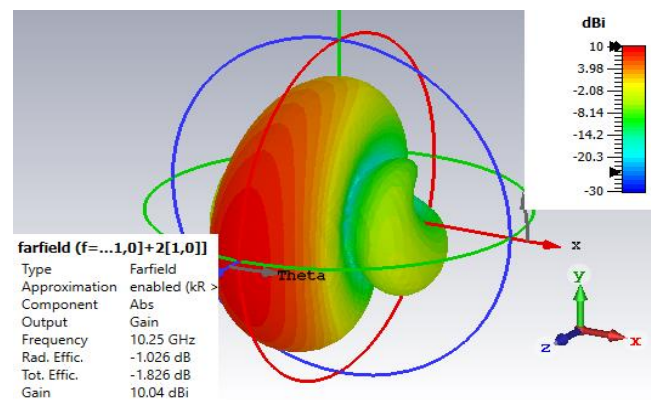
Figure 23: Gain of the designed four Patch Antenna and two port.

The obtained antenna gain value is equal to (10dB), while the obtained directivity value is equal to (11.1dBi).
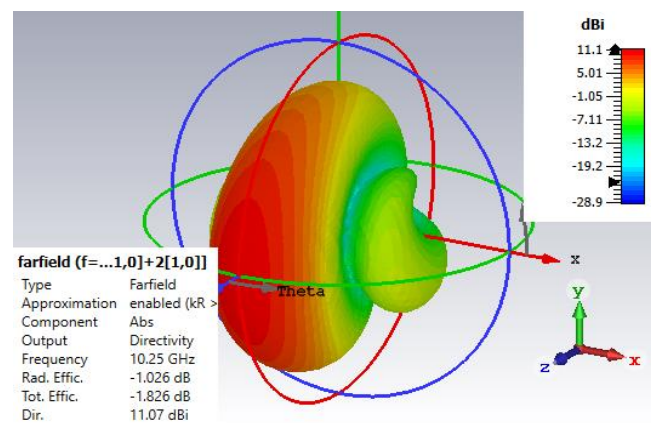
Figure 24: Directivity of the designed Four Patch Antenna and Two port.
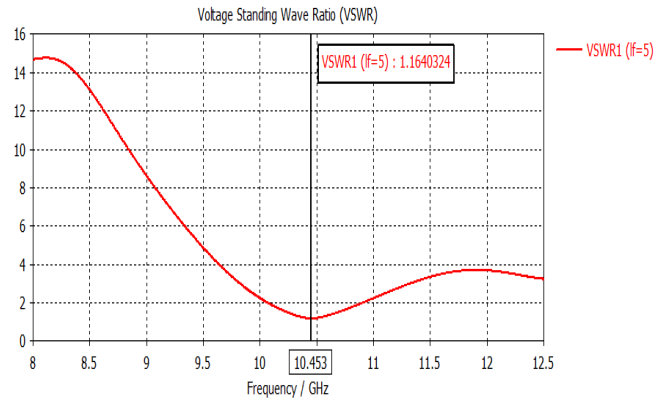
Figure 26: VSWR of the designed four Patch Antenna and Two port.

From the curve, we notice that the value of the VSWR at the operating frequency is equal to (1.164), and this means that the value of the reflection coefficient is very small.

The value of the total efficiency is equal to (-1.733dB), and the radiation efficiency value is (-1.026dB).

TABLE VII: COMPARATOR OF PARAMETERS PERFPRMANCE

parameters	Single element	2×2 element	1×2 element	1×4 element	2×4 element
Return loss (dB)	-53.460	-36.686	-25.494	-21.34	-22.404
Gain (dB)	3.79	7.13	6.62	6.94	10
Directivity (dBi)	7.51	10.2	8.83	11.2	11.1
-10 dB	863.1	2050	777	418	791

Bandwidth (MHZ)					
VSWR	1.004	1.029	1.112	1.18	1.16
BW%	8.35%	18.75%	7.46%	3.90%	7.54%
Efficiency%	42.55%	49.20%	60.10%	37.75%	78.95%

When comparing the results of the antenna parameters, the highest return loss value is in the case of Single Element and is -53.460 dB with a bandwidth of 863.1 MHz, and the antenna efficiency is 42.55%. As for the highest bandwidth, which was in the Two Element antenna, it was 2050 MHz, the return loss value was -36.686 dB, and the antenna efficiency was 49.20%.

The value of the return loss in the 1×2 antenna was -25.494 dB, and the bandwidth was 777 MHz. The overall efficiency of the antenna was 60.10%, which is better compared to the 1×4 antenna, where its efficiency was 37.75%. The return loss value was -21.34 dB, and the bandwidth was 418MHz, while the 2×4 antenna outperformed, as its efficiency reached 78.95%, and the bandwidth was 791 MHz, which is better compared to the previous antenna, as well as the return loss value amounted to -22.404 dB.

5. CONCLUSION

This paper presents the design of patch antennas at 10.25 GHz operating between 8.5 GHz and 12 GHz. Small ribbon line was used for feeding. The proposed antenna will work better in radar applications and some communications satellites. Comparing a single-spot antenna with a dual-spot antenna indicates the superiority of a dual-spot antenna on the basis of gain value, directivity, and bandwidth. Likewise, comparing a single-spot antenna with a quad-spot antenna indicates the superiority of a quad-spot antenna on the basis of gain value and directivity. By adding other corrections, gain and directionality are increased, which is important in an antenna because it improves its performance when used in applications.

References

[1] Merlin Teresa, P., and G. Umamaheswari. "Compact slotted microstrip antenna for 5G applications operating at 28 GHz." *IETE Journal of Research* 68.5 (2022): 3778-3785.

[2] Hossain, Sifat, et al. "Design and Analysis of 3.5 GHz Rectangular Patch Microstrip Antenna for S-Band Applications." *2023 IEEE International Conference on Integrated Circuits and Communication Systems (ICICACS)*. IEEE, 2023. https://www.researchgate.net/publication/319042764_DESIGN_AND_ANALYSIS_OF_MULTI_BAND_RECTANGULAR_MICROSTRIP_PATCH_ANTENNA_FOR_C_BAND_AND_X_BAND_APPLICATIONS

[3] Paul, Liton Chandra, et al. "Design of high gain microstrip array antenna and beam steering for X Band RADAR application." *2020 joint 9th international conference on informatics, electronics & vision (ICIEV) and 2020 4th international conference on imaging, vision & pattern recognition (icIVPR)*. IEEE, 2020.

[4] Sudhaman, K., T. Godhavari, and R. Anusha. "Design of Microstrip Patch Antenna at 10.3 GHz for X-Band Applications." *IOP Conference Series: Materials Science and Engineering*. Vol. 993. No. 1. IOP Publishing, 2020.

[6] Karahan, Mehmet, et al. "Microstrip Patch Antenna Design at 10 GHz for X Band Applications." *arXiv preprint arXiv:2303.09963* (2023).

[7] Genç, Abdullah, Mehmet Fatih Çağlar, and Bilge Şenel. "Comparison of design parameters of corporate feed 10GHz rectangular microstrip array antennas." *2014 22nd Signal Processing and Communications Applications Conference (SIU)*. IEEE, 2014.

Enhancing Precision and Stability of Two-Axis Platform Control with PID Controller Technology: Experimental Validation and Comparative Analysis

5

Enhancing Precision and Stability of Two-Axis Platform Control with PID Controller Technology: Experimental Validation and Comparative Analysis

Najeb Koni Omran
Higher Institute of Science and Technology -Zawia
r9_nono@yahoo.com

Khari A. Armih
Electronic Systems and Programing Center
Libya – Tripoli
khari.armih@gmail.com

Abstract

Within the ever-changing technological landscape, control systems play a pivotal role in diverse applications. This study extends prior research, examining the application of PID (Proportional-Integral-Derivative) controller technology in regulating a bi-directional moving platform. Leveraging a specialized program from EPOS designed for MAXON DC motors, previous findings are integrated into this framework, facilitating the subsequent implementation of the control system.The research aims to analyse the practical application of PID controller technology for achieving precise and comprehensive system stability. Through a thorough examination of the obtained results, this paper assesses their proximity to realizing complete and accurate system stability. The outcomes have the potential to advance control systems, particularly in the context of bi-directional platforms, providing valuable insights for engineers and researchers seeking to optimize system control through PID controller technology.

Keywords: PID Controller, multi-axis, MATLAB, brushless DC motors MAXON.

1. Introduction

The precise control of two-axis platforms holds critical importance across a spectrum of engineering and industrial applications. These platforms serve as integral components in systems ranging from manufacturing processes to robotic systems, demanding a high degree of accuracy and stability in their control mechanisms. In pursuit of advancing the state-of-the-art in control technology, this study focuses on the application of Proportional-Integral-Derivative (PID) controllers to enhance the precision and stability of two-axis platforms [1].

PID controllers have emerged as versatile tools in the field of control engineering, offering a balanced approach by incorporating proportional, integral, and derivative components. Their effectiveness in regulating dynamic systems has made them a cornerstone in control system design. Theoretical understanding of PID controllers has been well-established, showcasing their ability to address complex and dynamic scenarios. However, their practical application and performance in the specific context of two-axis platform control warrant empirical investigation [2].

The overarching goal of this paper is to experimentally validate the efficacy of PID controllers in the context of two-axis platforms. The study aims to contribute empirical evidence supporting the theoretical foundations of PID controllers, emphasizing their potential to enhance both precision and stability in real-world applications. To achieve this, a comprehensive experimental setup has been devised, integrating PID controllers into the control system of a two-axis platform [2].

This investigation is not limited to a standalone assessment of PID controllers; rather, it encompasses a comparative analysis with alternative control methods. By subjecting the two-axis platform to a series of controlled maneuvers and disturbances, we aim to discern the specific advantages and limitations of PID controllers in comparison

to traditional and modern control strategies. This comparative approach adds depth to our understanding of the PID controller's performance under varying conditions and provides insights into its optimal application domains [1].

As technology continues to evolve, the demand for precision control in dynamic systems escalates. This study, therefore, addresses a pertinent need in the realm of control engineering by exploring the practical implications of PID controller technology in the nuanced domain of two-axis platform control. The findings of this research are poised to contribute not only to the optimization of two-axis platforms but also to the broader discourse on the advancement of control systems in dynamic environments [2].

2. System Hardware

In this section, exploration focuses on the vital components constituting the hardware framework of the system under investigation. A robust control system necessitates not only advanced control algorithms but also relies on a well-structured hardware infrastructure capable of translating these algorithms into precise, real-world actions.

The core of the system hardware involves DC motors of the MAXON type. To effectively harness their capabilities, application relies on a dedicated hardware and software solution provided by EPOS. Chosen for their exceptional performance characteristics, these motors prove ideal for applications requiring precision and reliability [3].

Additionally, the discussion encompasses sensors and feedback mechanisms crucial for providing necessary data to the PID controller. The cornerstone of an efficient control system lies in accurate feedback, and the exploration focuses on how these components contribute to achieving desired levels of precision [3] [4].

Furthermore, attention is directed towards the physical setup of the platform and its mechanical elements. A profound understanding of the system's physical layout is imperative for effective control. Exploration extends to design considerations and mechanical aspects enabling the platform to move in two directions with the required stability [4].

The section aims to provide a comprehensive overview of the system's hardware components and their interplay in facilitating the application of PID controller technology. A strong hardware foundation is essential for realizing the full potential of the control system. By the section's conclusion, readers gain a clear understanding of critical elements constituting the experimental setup [3].

Figure 1: EPOS 70/10 position controllers (HARDWARE)[3]

3. System Software

In this section, the focus shifts to the software elements driving the control and operation of the system. While the hardware provides the physical infrastructure, the software breathes intelligence and precision into the system's movements.

Central to the investigation is a specialized software program developed by EPOS, tailored for controlling DC motors of the MAXON type. This software serves as the interface through which PID control algorithms are executed. The intricacies of this software will be explored, detailing how it accommodates the specific needs of the system and facilitates the translation of control commands into motor movements [3].

The software setup incorporates PID controller algorithms, playing a pivotal role in maintaining the desired system stability. Tuning and configuring PID controller parameters to align with the characteristics of MAXON DC motors and the platform's movement requirements will be discussed [3].

Furthermore, data acquisition and processing routines within the software are essential for gathering feedback from the system's sensors. The software is responsible for making real-time adjustments based on the feedback, ensuring that the platform's movements remain accurate and stable [5].

The programming and software architecture are fundamental aspects that enable the smooth integration of hardware and control algorithms. The code structure, logic, and any customizations made to the software to meet the unique demands of the system will be explored [6].
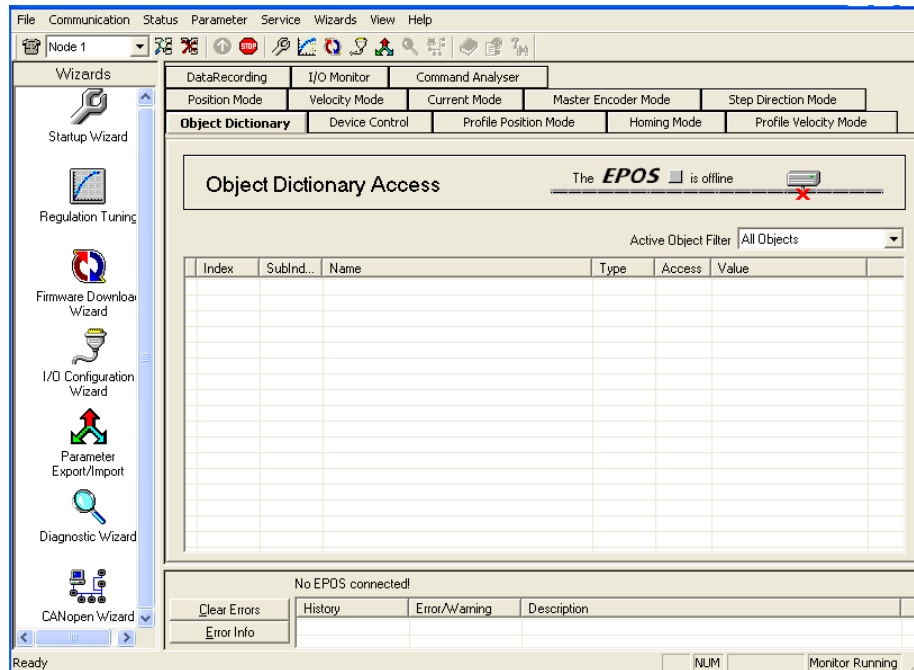
Figure 2: EPOS User Interface program (SOFTWARE)

4. PID controller and the DC motor system modelling

4.1 PID Proportional, Integrator, Derivative controllers

A closed loop control system is one that determines a difference in the desired and actual condition (the error) and creates a correction control command to remove this error, one form of controller widely used in industrial process control is called three terms, or PID controller, PID control demonstrates three ways of looking at this error and correcting it as shown in Figure 5.

The first way is the (P of PID), the proportional term, this term represents, the bigger the error, the bigger the correction. [4]

The (I in PID) is the second way which is for the integral of the error over time. The integral term produces a correction that considers the time where the error has been present. Stated in other words, the

longer the error continues, the bigger the correction. Lastly, the (D in PID) way which is stands for derivative. In the derivative term, the corrective action is related to the derivative or change of the error with respect to time [1].

In other words, the faster the error is changing, the bigger the correction. Control systems can use P, PI, PD, or PID in creating corrective actions. The problem generally is "tuning" the system by selecting the proper values in the terms [1].

The transfer function of the controller is:

$$Gc(s) = Kp + \frac{Ki}{s} + sKd \tag{1}$$

$$Gc(s) = \frac{Kds^2 + Kps + Ki}{s} \tag{2}$$

The controller provides a proportional term, an integration term, and a derivative term. The equation for the output in the time domain is:

$$u(t) = Kpe(t) + Ki \int e(t)dt + Kd\frac{de(t)}{dt} \tag{3}$$

The three-mode controller is also called a PID controller because it contains a proportional, an integral, and a derivative term [7].
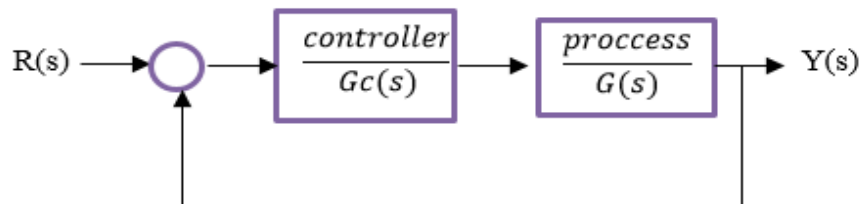
Figure 3: Closed-loop systems with a controller

4.2 DC motor modelling and PID controller

4.2.1 Physical setup

A common actuator in control systems is the DC motor which directly provides rotary, the electric equivalent circuit of the armature and the free-body diagram of the rotor are shown in Figure (6) [8] [4].
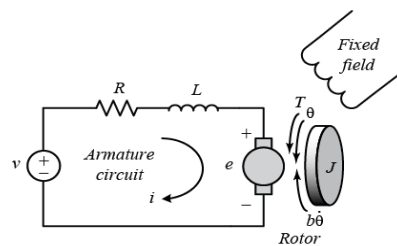
Figure 4: The electric DC motor equivalent circuit of the armature and the free-body diagram of the rotor

4.2.2 Plant to be controlled

The plant to be controlled as illustrated in Figure (5) is the actual DC motor base assembly with a simulated inertial load platform. The simulated moment of inertia is less than the actual DC motor moment of inertia. The effective gear ratio is 93:1 (from the motor armature shaft to the actual load).
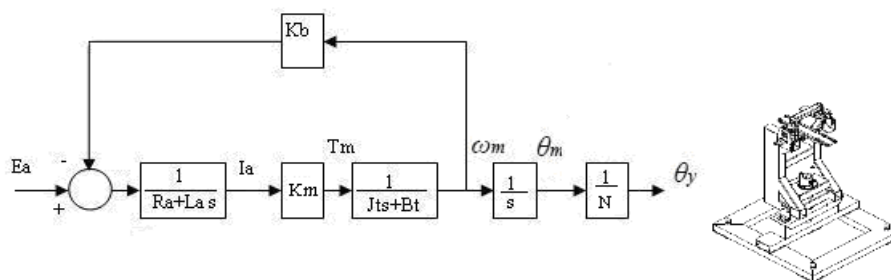
Figure 5: block diagram of integrated model for (YAW or PITCH axis rotation)

The sensor used is a 500--line optical encoder. It is directly mounted to the armature shaft, so that it rotates at the armature speed. Either of the two encoder signals, A~or~B can be used to measure velocity. Since there are 500 pulses per armature revolution, the number of pulses per load revolution is (93 shaft rev./1 load rev.) * (500 pulses /shaft rev.) . [4]

The open loop transfer function of single joint relating the angular displacement to the applied voltage of the joint platform is as follows [4]:

$$Gs = \frac{\theta y}{Ea} = \frac{Km}{Ns[Ra(Jts + b) + KbKm\,l}
\qquad (4)$$

SO:

$$Gs = \frac{\theta y}{Ea} = \frac{Km}{Ns[sRaJt + Rab + KbKm]}
\qquad (5)$$

$$Gs = \frac{Km}{Ns[Ra(Js + b) + KbKm]}
\qquad (6)$$

$$Gs = \frac{Km\,/(Ra + KbKm)}{N\,s(\tau 1\,s\ +\ 1)}
\qquad (7)$$

$$\tau 1 = \frac{RaJ}{Rab + KbKm}
\qquad (8)$$

And the relation between the angular velocity *ωm(s)* to the armature voltage *Ea* is given by:

$$\frac{\omega m(s)}{Ea(s)} = \frac{Km}{[s\,Ra\,Jt\ +\ Ra\,b\ +\ KbKm]}
\qquad (9)$$

Where:

Km= (Nm/A) torque constant

R= (ohm) resistance

L= (Hennery) inductance

Kb= (rad*sec/V) back emf

N= gear ratio

The transfer function of the Maxon Motor can be derived using data from Characteristics of brushless dc motor in the reference [4].

5. Results and Experiments

The comprehensive examination of the system's hardware and software, as detailed in the previous sections, lays the groundwork for the pivotal phase of the research results and experiments. Meticulously addressing the hardware components, from the high-performance MAXON DC motors to the intricate sensors, and exploring the intricacies of the specialized EPOS software and PID control algorithms, the focus is now on unveiling the outcome of their harmonious interplay.

In the subsequent section, the practical implementation of the control system on the two-directional platform will be delved into, and the results obtained will be assessed. The synergy between the hardware and software components sets the stage for the empirical validation of the research, where precision, stability, and performance are put to the test, and the real-world implications of PID controller technology become evident.

5.1 Current controller

- **Current Controller manual tuning:**

  $Kp\_c = 16\ \Omega\ ,\quad Ki\_c = 31.28\ k\ \Omega/s$

  $KP....EPOS = KP....SI\ /\ 0.00391\Omega\ \ = 4000$

  $KI....EPOS = KI....SI\ /\ 0.\ 0391k\Omega/s\ \ = 800$
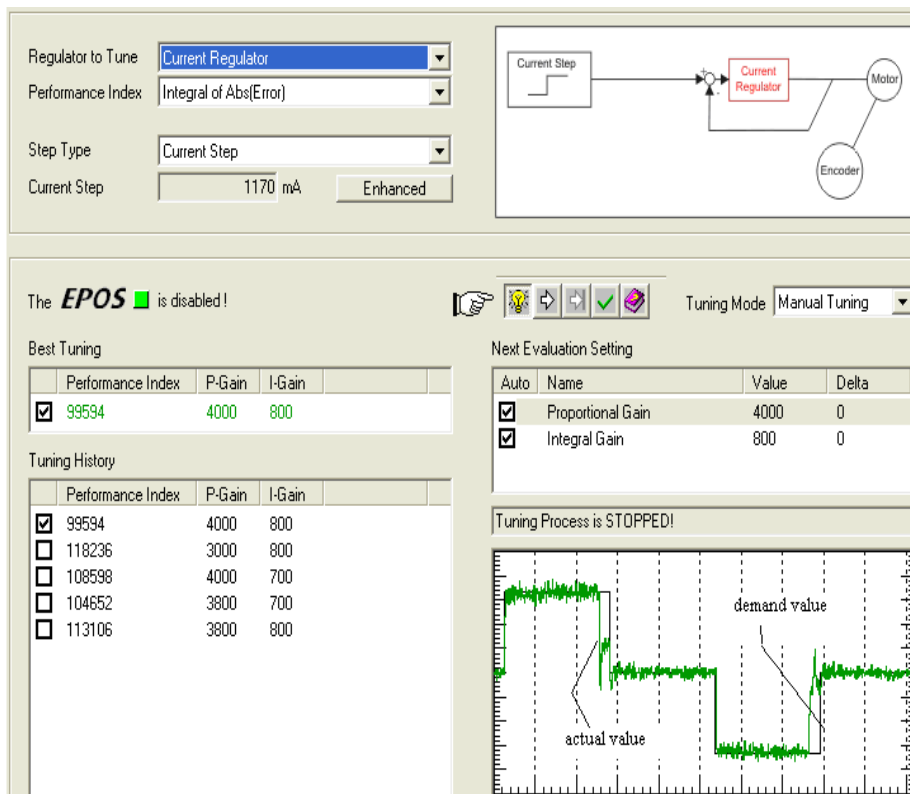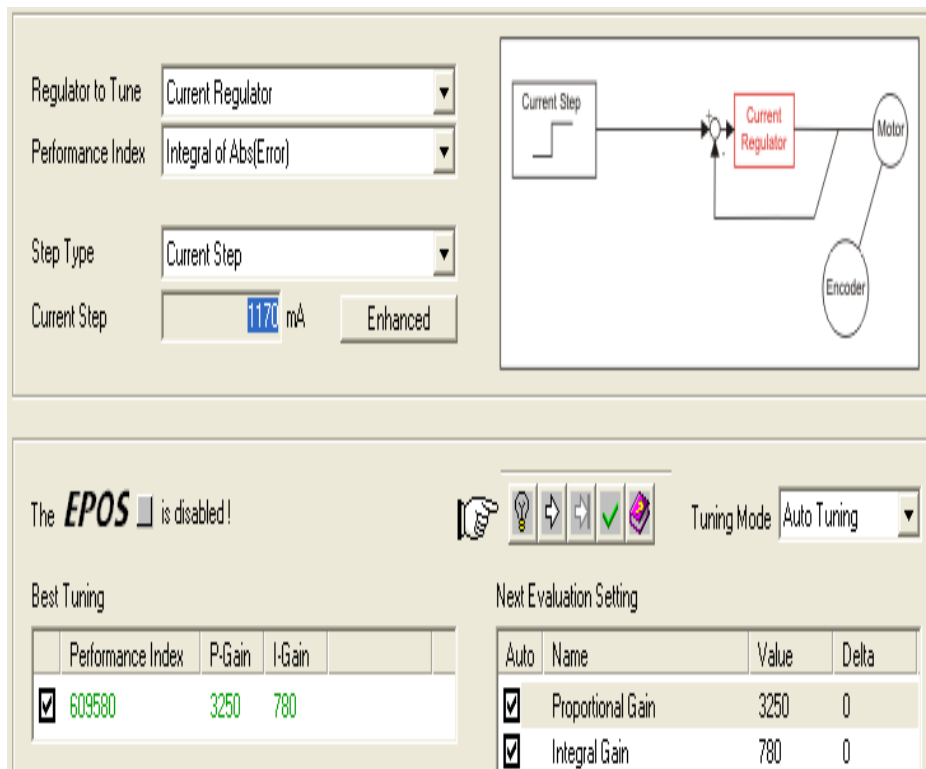
Figure 6: Current Controller Manual Tuning

- **Current Controller auto tuning by EPOS software**

Figure 7: Auto Tuning by EPOS Software
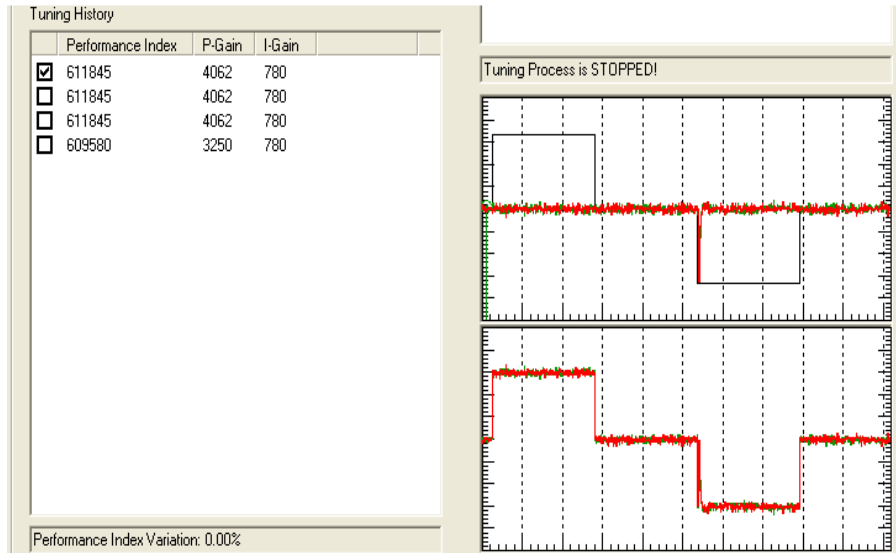
Figure 8: Current Controller Auto Tuning by EPOS Software
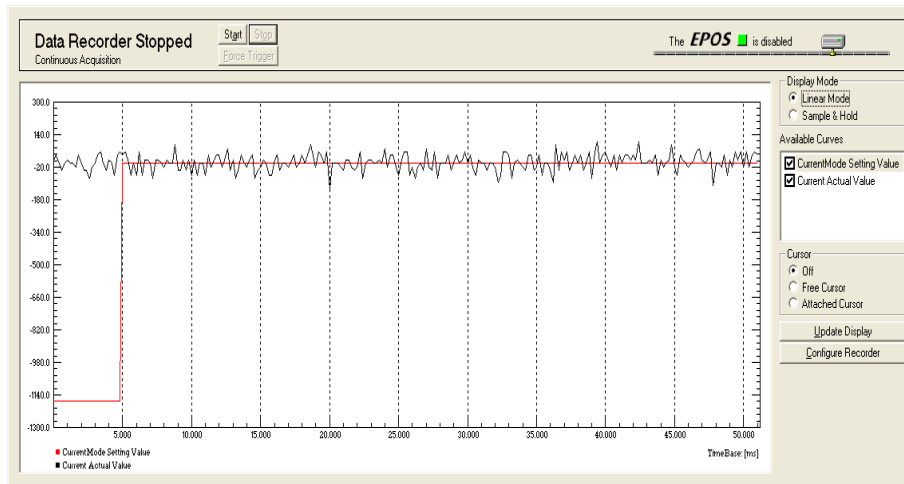
Figure 9: Current Step Response

5.2 Position controller

- **Position controller manual tuning:**

Kp = 31.25 , Ki = 1.17   , Kd = 286

KP....EPOS = KP....SI / 0.01 = 3125

KI....EPOS = KI....SI / 0.078 = 15

KD....EPOS = KD....SI / 0.08 = 3581. [6]
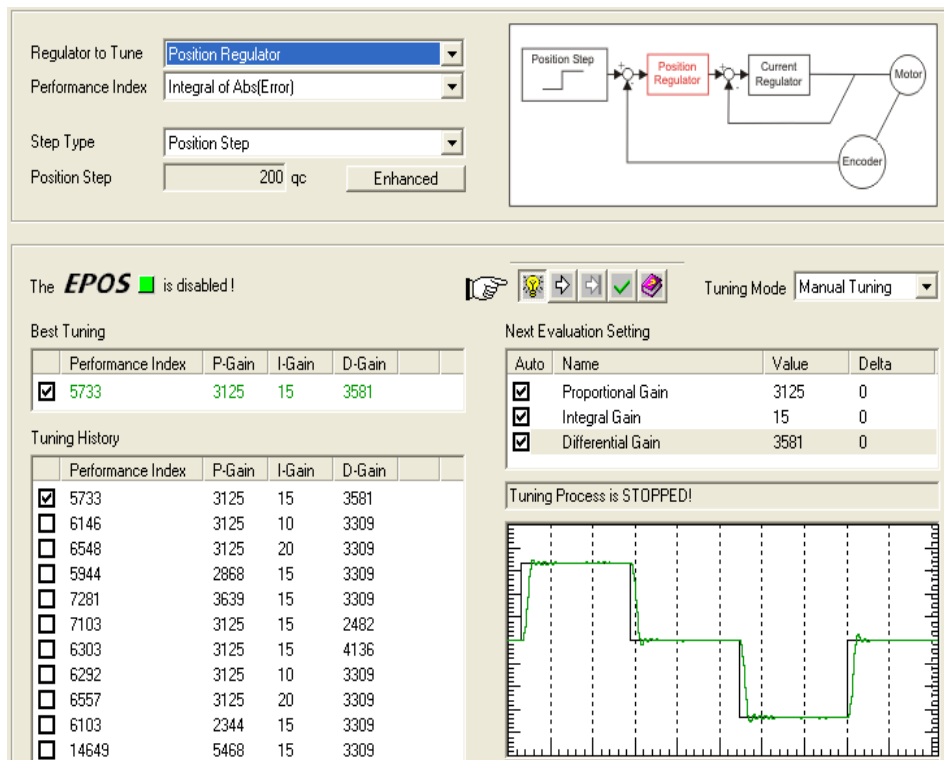
Figure 10: Position Controller Manual Tuning

- **Position controller auto tuning by EPOS software:**
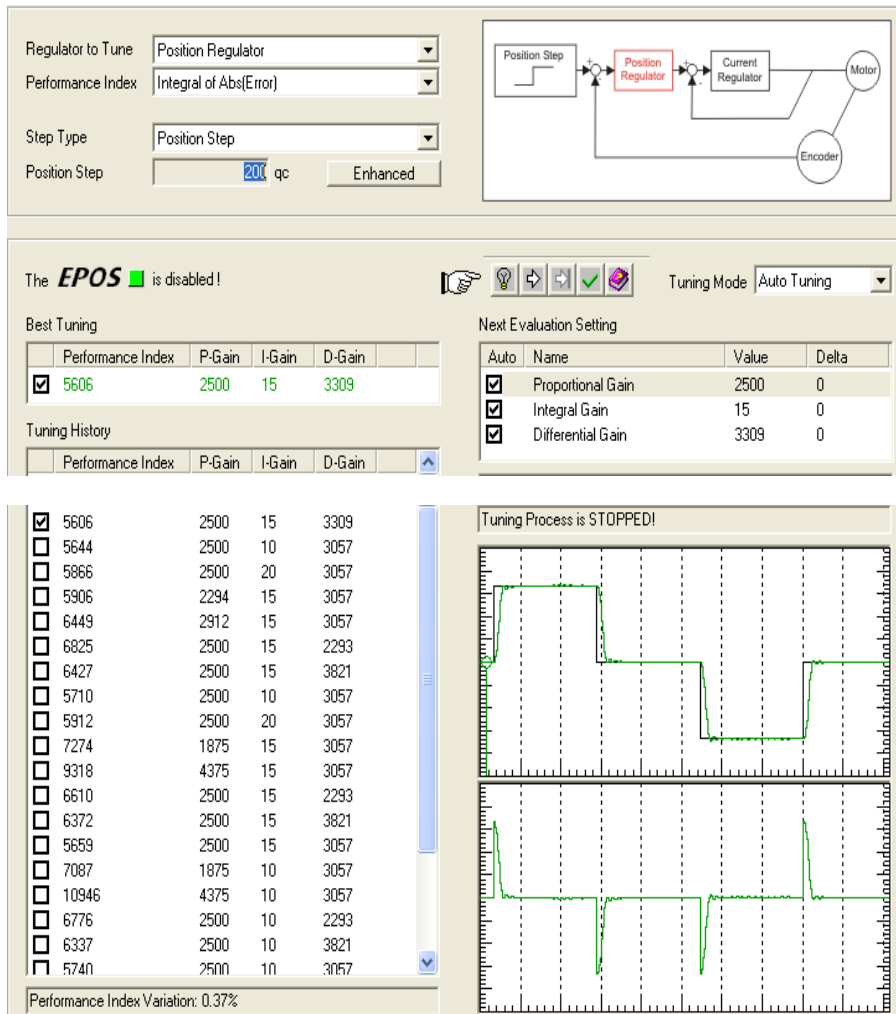
Figure 11: Position controller auto tuning by EPOS software

$KP....SI = 10 \ mA/rad \qquad . KP....EPOS = 25 \ mA/rad$

$KI....SI = 78 \ (mA/s \ )/rad \qquad . KI....EPOS = 1.17 \ (mA/s \ )/rad$

$KD....SI = 80 \ (\mu As)/rad \qquad . KD....EPOS = 264.72 \ (\ mAs)/rad. \ [6]$
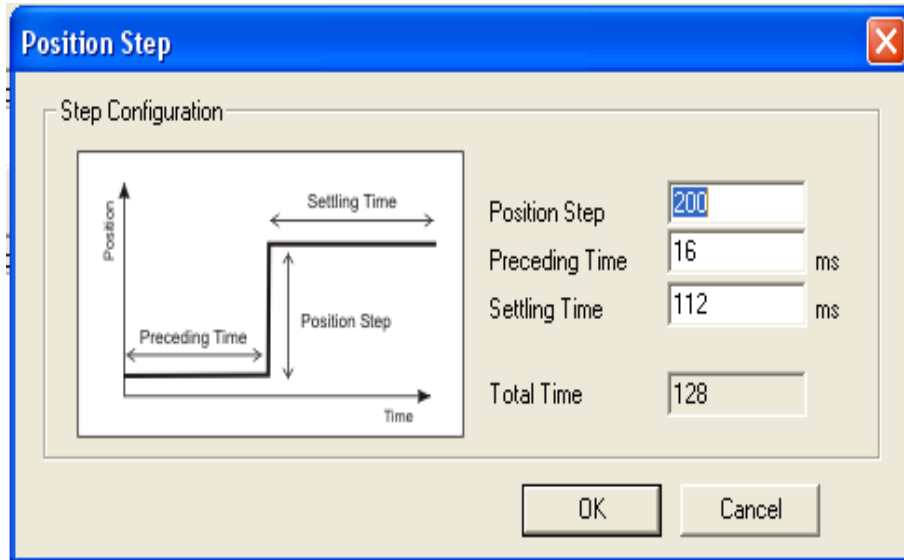
Figure 12: Position Step Input
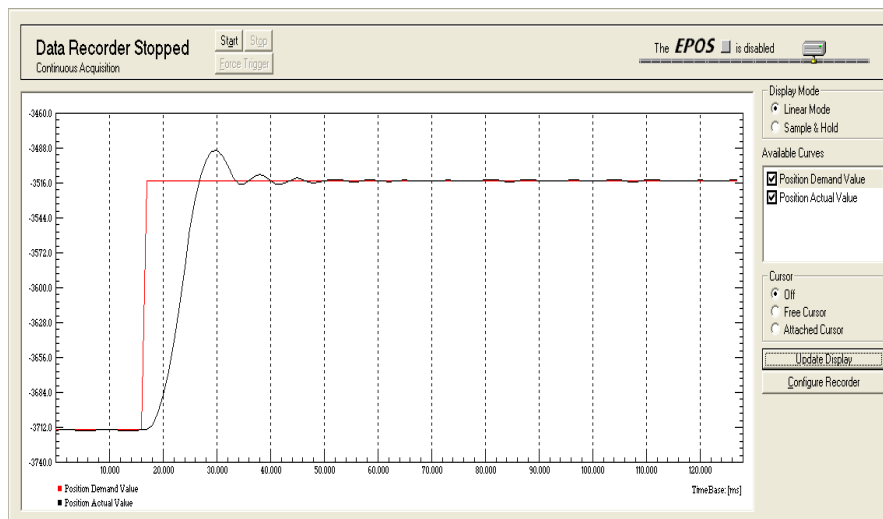
Figure 13: Position Step Response for yaw axis

6. Analysis of Results

Based on the experimental findings, it is clear that the implementation of the PID controller effectively governed the system. The primary goal was to establish a model for the two-axis platform and formulate control strategies for current, velocity, and position using classical control methods. These strategies were subsequently put into action by selecting suitable hardware

6.1 Current controller

The discussion and analysis of the current control results, as observed in Figure 10, reveal that the optimized system performs exceptionally well, surpassing the results obtained through the included EPOS software. Notably, the system exhibits minimal error in tracking the desired value, especially in terms of steady-state error.

It exhibited greater stability compared to the system in the calibrated or adjusted state through the EPOS MAXON MOTOR software, as depicted in Figures 7 and 8.

Figure 9 illustrates the step response of the implemented system on the platform, indicating that it was more stable and had a lower steady-state error.

6.2 Position controller

The examination and interpretation of the present control outcomes, as depicted in Figure 6, indicate that the enhanced system demonstrates outstanding performance, surpassing the outcomes achieved using the provided EPOS software. Noteworthy is the system's minimal deviation from the desired value, particularly in relation to steady-state error.

In Figure 11, it is observed that the system tracks the desired direction as a target or goal to be achieved.

As for Figure 13, it illustrates that the approach followed in system tuning has led to a highly stable system with minimal possible error.

The system reached stability at approximately 40 milliseconds.

It is noteworthy that the results obtained in this study surpassed those presented in our previous paper published in the same journal, focusing on the "two-axis platform controller." The components, resulting in a remarkable alignment with the expected outcomes. utilization of the PID controller led to a system that demonstrated even greater precision, stability, and efficiency, along with a significantly reduced steady-state error. This advancement underscores the notable impact of PID control technology in refining the system's response, enhancing its stability, speed, and minimizing steady-state error.

The chosen hardware for the system exhibited an outstanding level of performance, ultimately yielding satisfactory results during the experiments. Key performance metrics, including precision, stability, and tracking accuracy, closely aligned with the expected results.

An intriguing observation was the consistency between the experimental results and the outcomes of our controller tuning exercises. This coherence suggests that the theoretical models and tuning parameters successfully governed the behavior of the platform. The remarkable alignment between anticipated and observed results emphasizes the efficiency and effectiveness of PID controller technology when applied to the control of a bi-directional platform.

Furthermore, the system's robustness was tested under varying conditions and external disturbances, revealing its ability to maintain stability and perform with remarkable adaptability. This adaptability and resilience highlight the real-world applicability of PID controller technology in dynamic environments, affirming its potential for widespread use in applications requiring precise and stable control.

In conclusion, the analysis of the results not only confirms the practical viability of PID controller technology for the control of a two-axis platform but also underscores its substantial improvement over the results presented in paper under the title tow axis platform PID controller. The system exhibited impressive stability and precision, making it a promising solution for a range of applications where precise control of movement is crucial. These findings not only contribute to the field of control systems but also provide valuable insights for engineers and researchers aiming to leverage the potential of PID control.

7. Conclusion

Based on the compelling experimental findings, it is evident that the implementation of the PID controller has effectively governed the two-axis platform system. The primary objective was to establish a model for the platform and formulate control strategies for current, velocity, and position using classical control methods. These strategies were subsequently put into action through the careful selection of appropriate hardware.

In the realm of current control (Section 5.1), the optimized system exhibited exceptional performance, surpassing the results obtained through the included EPOS software. Figure 10 illustrates the minimized error in tracking the desired value, particularly in terms of steady-state error. Notably, the system demonstrated superior stability compared to the state calibrated or adjusted through the EPOS MAXON MOTOR software, as evidenced in Figures 7 and 8. The step response depicted in Figure 9 further underscores the system's enhanced stability and lower steady-state error.

Turning to the position control analysis (Section 5.2), the enhanced system showcased outstanding performance, surpassing the outcomes achieved using the provided EPOS software (Figure 3). The system exhibited minimal deviation from the desired value, especially in

terms of steady-state error. Figures 11 and 13 highlight the system's ability to track the desired direction as a target, achieving a highly stable state with minimal error within approximately 40 milliseconds. Notably, these results surpassed those presented in a previous paper, showcasing a remarkable alignment with the expected outcomes and emphasizing the significant impact of PID control technology in refining the system's response.

The chosen hardware demonstrated an outstanding level of performance, yielding results that closely aligned with expected precision, stability, and tracking accuracy metrics. An intriguing observation was the coherence between experimental results and controller tuning exercises, suggesting that theoretical models and tuning parameters successfully governed the platform's behavior. This alignment reinforces the efficiency and effectiveness of PID controller technology in the control of a bi-directional platform.

Furthermore, the system's robustness was tested under varying conditions and external disturbances, demonstrating its ability to maintain stability with remarkable adaptability. This adaptability and resilience affirm the real-world applicability of PID controller technology in dynamic environments, showcasing its potential for widespread use in applications requiring precise and stable control.

In conclusion, the analysis of the results not only confirms the practical viability of PID controller technology for the control of a two-axis platform but also highlights its substantial improvement over previous results. The system's impressive stability and precision position it as a promising solution for various applications where precise control of movement is paramount. These findings contribute not only to the field of control systems but also provide valuable insights for engineers and researchers aiming to harness the potential of PID control in their work.

8. References

[1] B. C. kuo, Automatic control systems, Seventh edition.

[2] J. J. Craig, Introduction to robotics mechanics & control, Stanford University.

[3] M. E. motor, May 2010 edition, EC 60 Ø60 mm, brushless, 400 Watt.

[4] R. C. Dorf ‹Robert H. Bishop Modern Control Systems ‹Eleventh Edition .

[5] https://docs.rs-online.com/55c7/0900766b811a334f.pdf.

[6] J. o. E. S. a. Programming, "Implementation of Two Axises Platform Using PID Controller," Issue NO:4 December 2021.

[7] A. D. Guillermo J. Silva, PID Controllers for Time-Delay Systems.

[8] B. Friedland ‹Control System Design: An Introduction to State-Space Methods .

Design and Performance Evaluation of tangular Microstrip Patch Antenna Based on Different Dielectric Materials for 5G Applications at 28 GHz

6

Design and Performance Evaluation of Rectangular Microstrip Patch Antenna Based on Different Dielectric Materials for 5G Applications at 28 GHz

Marai M. Abousetta
Dept. of Electrical & Computer Engineering, School of Applied Sciences and Engineering
Libyan Academy for Postgraduate Studies
Janzoor, Libya
m.abousetta@academy.edu.ly

Fatima A. Alazraq
Dept. of Electrical & Computer Engineering, School of Applied Sciences and Engineering
Libyan Academy for Postgraduate Studies
Janzoor, Libya
fatimaalzraq@gmail.com

Abstract

This paper provides a rectangular Microstrip patch antenna design and a comparison analysis using three different types of substrate materials—the Arlon CLTE-AT, Arlon AD450, and Taconic RF-60. The thickness of the dielectric substrate is constant at 0.8mm for all three antennas, and the resonance frequency is selected as 28 GHz. Arlon CLTE-AT (Antenna 1), Arlon AD450 (Antenna 2), and Taconic RF-60 (Antenna 3) are the three substrate materials, and their respective relative permittivity values are 3, 4.5, and 6.15. The High Frequency Structure Simulator (HFSS) program, was implemented to evaluate and investigate all of the performance parameters, including return loss, bandwidth, VSWR, gain. For Antenna-1, Antenna-2, and

Antenna-3, the gains were 6.59 dB, 6.32 dB, and 5.35 dB, respectively. The bandwidth of all the antennas offered is greater than 100 MHz, with Antenna-1 having a 3.24GHz bandwidth, Antenna-2 having a 2.05GHz bandwidth, and Antenna-3 having a 554.7MHz bandwidth.

Keywords: Microstrip antenna, Rectangular Patch ,5G, 28GHz, Dielectric Material, Dielectric Constant, HFSS.

1. INTRODUCTION

In the last decade, wireless communication systems have become an important part of our civilization, an antenna is an essential unit of wireless system. The antenna is the basis of wireless communication. Without antennas, the world could not reach the age of this technology [1].

The Microstrip patch antenna is one of the most desirable antenna structures for their low profile and easy manufacture. They are useful because they can be directly printed on the circuit boards. They have many applications, especially in wireless communication and in satellite communication [2].

Recently, there has been a lot of advanced wireless communication, with the latest of all 5G wireless [3]. 5G wireless is usually preferred for higher operating frequencies   compared to 4G exceeding 24 GHz. In 2015, the International Union of Telecommunications (ITU) implemented a possible millimeter wave frequency band from 24 GHz to 84 GHz at the World Radio Communication Conference [4]. In the new era of exponential Internet users, as well as the Internet of Things (IOT), include people's daily lives that 5G technology must be adapted to all modern devices. 4G technology could not meet these requirements due to lack of bandwidth. In addition, 5G communication systems have higher

permeability, higher bit speeds, lower power consumption (watt/bit) and better coverage, which is a necessity in this age of major data [5].

2. DESIGN PROCEDURE OF MICROSTRIP ANTENNA

The antenna design procedure involves designing the feed line, the matching element and the radiator patch. The dielectric constant (ε_r), substrate thickness (h), and resonant frequency (f_r) are the exact properties required to construct a Microstrip antenna [6].

A. Rectangular Patch

The following equations are used to calculate the patch width, Wp, and length, Lp:

$$W = \frac{c}{2 f_o \sqrt{\frac{(\varepsilon_r + 1)}{2}}} \qquad (1)$$

Where,
 c is the speed of light.
 ε_r is the dielectric constant
 f_r is the resonant frequency.

$$L = L_{eff} - 2\Delta\text{L} \qquad (2)$$

Where L_{eff} is the effective length, which can be calculated as follows?

$$L_{eff} = \frac{c}{2 f_o \sqrt{\varepsilon_{reff}}} \qquad (3)$$

Where, ε_{reff} is the effective permittivity of the dielectric?
As shown in the following formula, the effective dielectric constant is determined as follows:

$$\varepsilon_{reff} = \frac{\varepsilon_r+1}{2} + \frac{\varepsilon_r-1}{2}\left[1 + 12\frac{h}{W}\right]^{-\frac{1}{2}} \tag{4}$$

Furthermore, L is extended length and can be calculated using:

$$\Delta L = 0.412h \frac{(\varepsilon_{reff}+0.3)\left[\frac{W}{h}+0.264\right]}{(\varepsilon_{reff}-0.258)\left[\frac{W}{h}+0.8\right]} \tag{5}$$

B. Ground Plane

The length and width of the ground plane can be calculated using

$$W_g = W + 6h \tag{6}$$

$$L_g = L + 6h \tag{7}$$

Where, h is the substrate thickness.
Where the ground plane dimensions are the same as the length and width of the substrate.

C. Microstrip Feed Line

The following equation gives the feed line's length:

$$L_T = \frac{c}{2f_o\sqrt{\varepsilon_r}} \tag{8}$$

The ratio of W/h is calculated using a given characteristic impedance and dielectric constant as

$$\frac{W}{h} = \frac{2}{\pi}\left[B - 1 - \ln(2B - 1) + \frac{\varepsilon_r-1}{\varepsilon_r}\left\{\ln(B - 1) + 0.39 - \frac{0.6}{\varepsilon_r}\right\}\right] \; for \; \frac{W}{h} > 2 \tag{9}$$

$$\frac{W}{h} = \frac{8e^A}{e^{2A}-2} \qquad for \; \frac{W}{h} > 2 \tag{10}$$

Where:

$$A = \frac{Z_0}{60}\sqrt{\frac{\varepsilon_r + 1}{2}}$$
$$+ \frac{\varepsilon_r - 1}{\varepsilon_r + 1}\left(0.23\right.$$
$$\left.+ \frac{0.11}{\varepsilon_r}\right) \tag{11}$$

$$B = \frac{377\pi}{2Z_0\sqrt{\varepsilon_r}} \tag{12}$$

D. Quarter Wave Transformer

When an impedance mismatch is a possible, the quarter wave transformer is a Microstrip line that is used as an appropriate matching method. In order to match their impedances, for the width of a rectangular patch, a quarter wave transformer operates between the Microstrip line and the middle point. The quarter wave transformer length is equal to

$$L_T = \frac{\lambda g}{4} \tag{13}$$

Where λg is the guided wavelength ($\lambda g = \frac{\lambda o}{\sqrt{\varepsilon_r}}$)

The quarter wave transformer's impedance is given by

$$Z_T = \sqrt{Z_O Z_P} \tag{14}$$

The input impedance at the width center is [6].

$$Z_P = \frac{1}{2G_1} \tag{15}$$

Where

$$G_1 = \begin{cases} \dfrac{1}{90}\left(\dfrac{W}{\lambda o}\right)^2 & W \ll \lambda o \\ \dfrac{1}{120}\left(\dfrac{W}{\lambda o}\right) & W \gg \lambda o \end{cases} \qquad (16)$$

By substituting the obtained impedance (Z_P) in equation 9, the quarter-wave transformer width is determined.

3. ANTENNA DESIGN AND STRUCTURE

Although there are many various ways to construct Microstrip antennas, the rectangular Microstrip patch antenna is the most popular. In this paper, a rectangular Microstrip patch antenna with a quarter wave transformer. Thickness and relative permittivity should be taken into account while choosing the antenna substrate. These two elements are important in affecting how well the antenna performance. Three Microstrip patch antennas designed with three different dielectric constants are presented in this paper. Arlon CLTE-AT is the particular substrate material that was used for Antenna 1. This the material has a dielectric constant of 3 and a loss tangent of 0.0013. Arlon AD450 for Antenna -2, which has a dielectric constant of 4.5 and a loss tangent of 0.0028, and Taconic RF-60 for Antenna3, which has a dielectric constant of 6.15 and a loss tangent of 0.0035mm. To ensure all of the proposed antennas were of the same thickness for performance comparisons at 28 GHz, 0.8 mm was chosen for this paper.

3.1 Antenna I
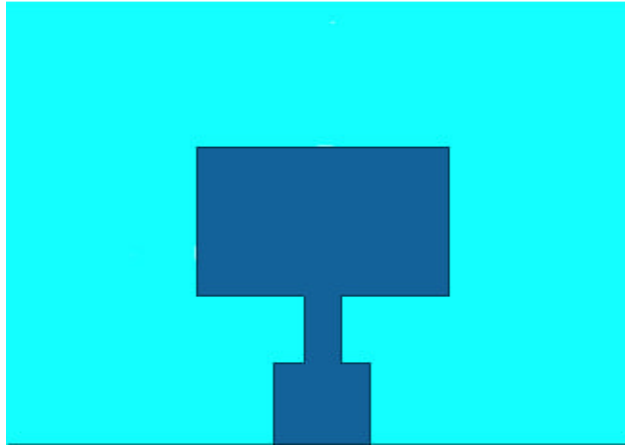
Figure 1: The designed rectangular patch of the *Arlon CLTE-AT* antenna.

TABLE I: Design parameters of the *Arlon CLTE-AT* antenna.

Parameter	Dimension
Patch length (L_p)	2.7mm
Patch width (W_p)	4mm
Feed line length (L_f)	1.529mm
Feed line width (W_f)	1.467mm
Substrate length (L_s)	10mm
Substrate width (W_s)	8mm
Ground plane width (W_g)	8mm
Ground plane length (L_g)	10mm
Transmission line length (L_T)	1.35mm
Transmission line width (W_T)	0.58275mm

3.2 Antenna II
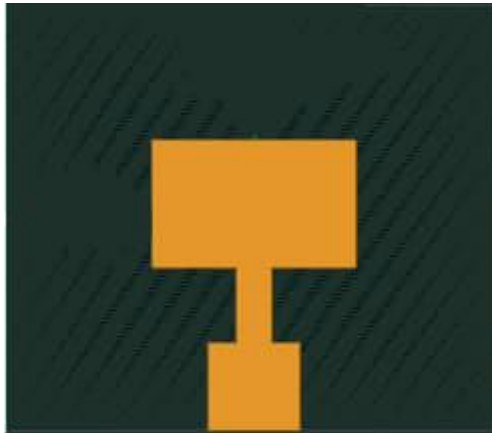
Figure 2: The designed rectangular patch of the *Arlon AD450* antenna.

TABLE II: Design parameters of the *Arlon AD450* antenna.

Parameter	Dimension
Patch length (L_p)	2.1mm
Patch width (W_p)	3.34mm
Feed line length (L_f)	1.529mm
Feed line width (W_f)	1.467mm
Substrate length (L_s)	8.06mm
Substrate width (W_s)	7mm
Ground plane width (W_g)	7mm
Ground plane length (L_g)	8.06mm
Transmission line length (L_T)	1.35mm
Transmission line width (W_T)	0.58275mm

3.3 Antenna III
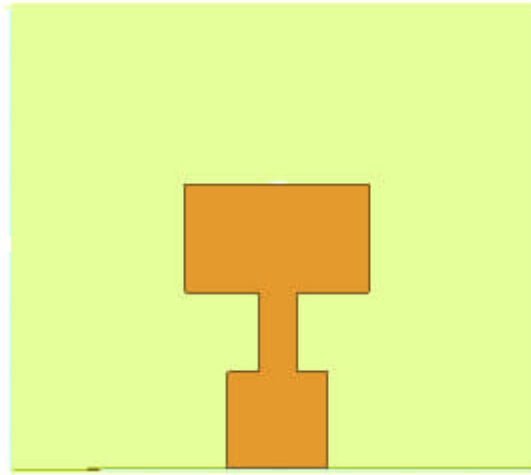
Figure 3: The designed rectangular patch of the *Taconic RF-60* antenna.

TABLE III: Design parameters of the *Taconic RF-60* antenna.

Parameter	Dimension
Patch length (L_p)	1.65mm
Patch width (W_p)	2.8mm
Feed line length (L_f)	1.529mm
Feed line width (W_f)	1.467mm
Substrate length (L_s)	8.06mm
Substrate width (W_s)	7mm
Ground plane width (W_g)	7mm
Ground plane length (L_g)	8.06mm
Transmission line length (L_T)	1.35mm
Transmission line width (W_T)	0.58275mm

4. RESULTS AND DISCUSSIONS

The return loss, bandwidth, VSWR and gain for each of the three antennas designed for 28GHz were used to express the results of the antenna performances.

4.1 Return Loss and Bandwidth of the Designed Antennas

Figures 4, 5, and 6 present the return loss graphs that were obtained for these designs, respectively.
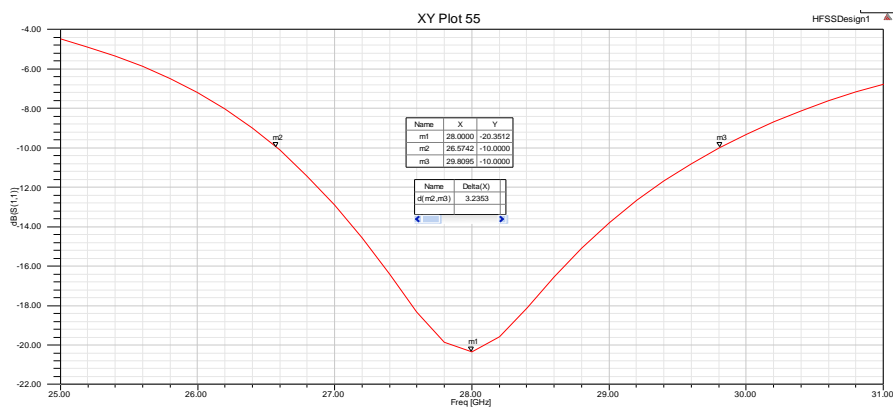
Figure 4: Return Loss VS Frequency of the designed Arlon CLTE-AT antenna.

According to Fig. 4, the simulated result of the Arlon CLTE-AT antenna at 28GHz resonant frequency and bandwidth is 3.24GHz with a maximum return loss value of -20.35dB.
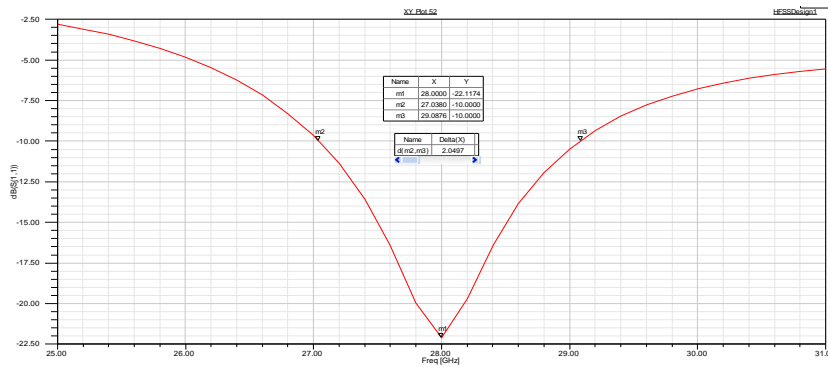
Figure 5: Return Loss VS Frequency of the designed Arlon AD450 antenna.

As shown in Fig. 5, the simulated result of the Arlon AD450 antenna at 28 GHz resonant frequency and bandwidth is 2.05 GHz, with a maximum return loss value of -22.12dB.
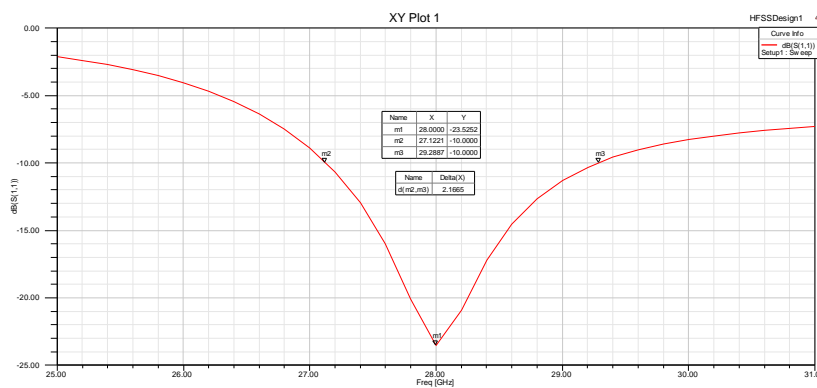
Figure 6: Return Loss VS Frequency of the designed Taconic RF-60 antenna.

Based on Fig. 6, it can be shown that the Taconic RF-60 antenna's simulated performance at 28GHz resonant frequency and bandwidth is 554.7 MHz, with a maximum return loss value of -23.52dB.

The Arlon CLTE-AT antenna got the highest value of the return loss, which was -20.35dB. The Taconic RF-60 antenna also produced the lowest value, -32.52dB. -10dB, or 11% of the antenna's reflected power, is the minimum acceptable value for the return. The Arlon CLTE-AT antenna had the maximum bandwidth value of 3.24GHz, while the Taconic RF-60 antenna had the minimum lowest value of 554.7MHz. An important parameter in achieving a high bandwidth value is the dielectric constant.

4.2 Voltage Standing Wave Ratio (VSWR)

Figures 7, 8, and 9 show the VSWR graphs that were obtained for these designs, respectively.
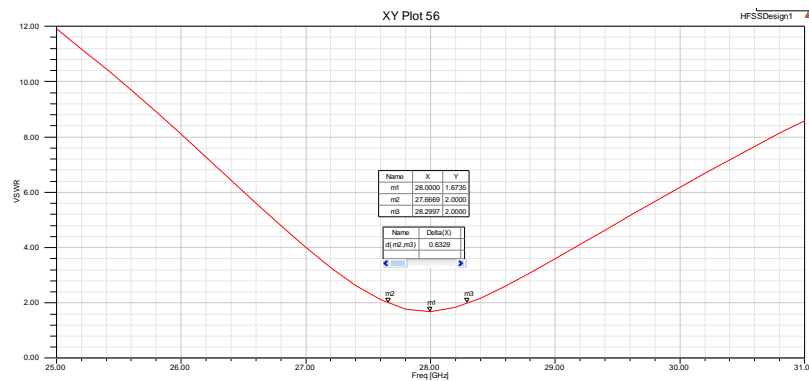
Figure 7: VSWR VS Frequency of the *Arlon CLTE-AT* antenna.
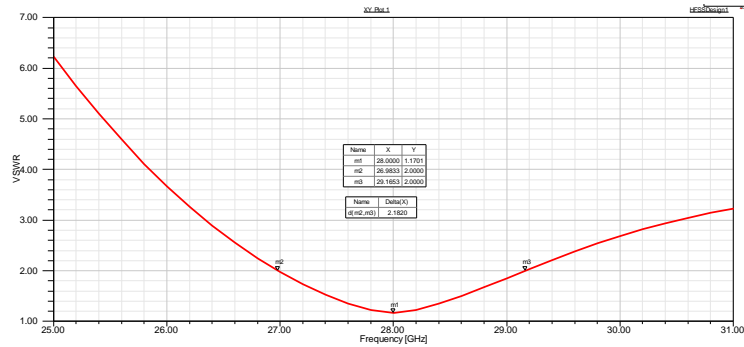
Figure 8: VSWR VS Frequency of the *Arlon AD450* antenna.
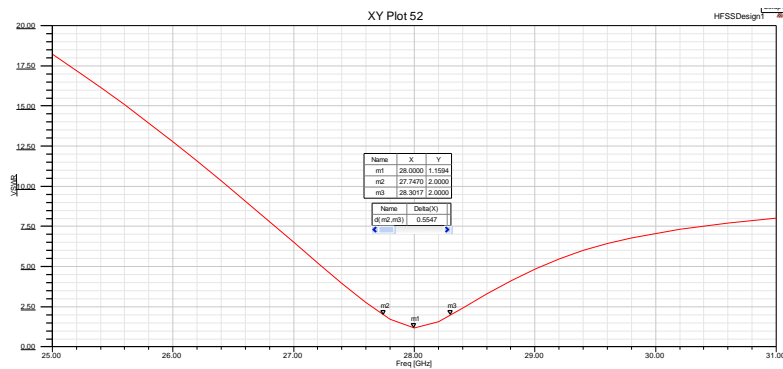
Figure 9: VSWR VS Frequency of the *Taconic RF-60 antenna*.

The simulated results of the Arlon CLTE-AT, Arlon AD450, RO4003, and Taconic RF-60 antennas at the operating frequency of 28GHz are shown in Figures 7 to 9, with values of 1.08, 1.17, and 1.14, respectively.

4.3 Gain

Figures 10-12 correspondingly show the gain achieved for the three designs.
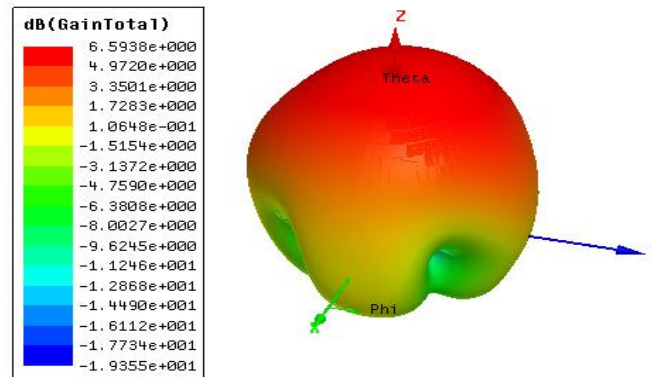
Figure 10: the gain of the *Arlon CLTE-AT* antenna.

Figure 10 shows the simulated result of the CLTE-AT antenna at the resonance frequency of 28GHz with gain value of 6.59dB.
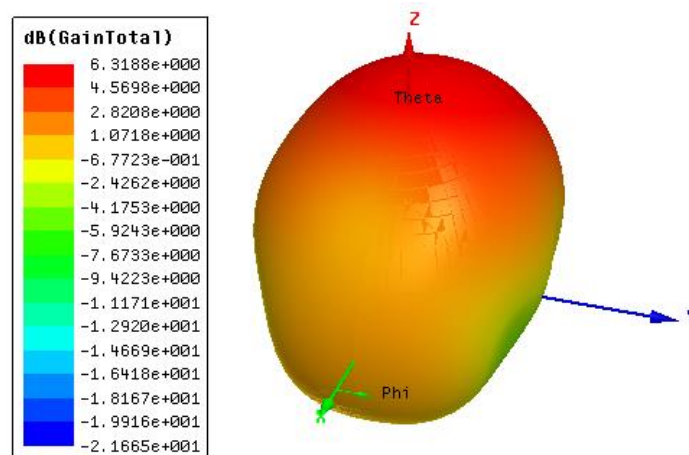
Figure 11: the gain of *Arlon AD450* antenna

Figure 11 shows the simulated performance of the Arlon AD450 antenna at the resonance frequency of 28GHz with gain value of 6.31dB.
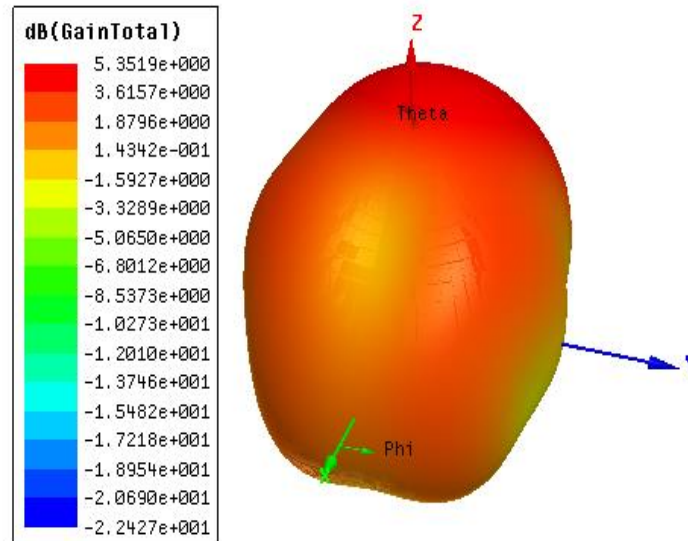
Figure 12: The gain of *Taconic RF-60* antenna

Figure 12 shows the simulated performance of the Taconic RF-60 antenna at the resonance frequency of 28GHz with gain value of 5.35dB. The Taconic RF-60 antenna given the least gain of 5.35dB at 28GHz and the Arlon CLTE-AT antenna produced the optimal gain of 6.59 at that frequency.

4.4 Comparison of the Proposed Antenna Designs

According to the performance indicators, which include return loss, bandwidth, VSWR, gain and size, the simulation results for all three antennas have been summarized and presented in TABLE IV below.

TABLE IV: Comparison of the proposed antennas performance at 28GHz

Parameter	*Arlon CLTE-AT*	*Arlon AD450*	*Taconic RF-60*
Resonant frequency (fr)	28GHz	28GHz	28GHz
Dielectric constant (εr)	3	4.5	6.15
Return loss (RL)	-20.35dB	-22.12dB	-23.52dB
Bandwidth (BW)	3.24GHz	2.05GHz	554.7MHz
VSWR	1.67	1.17	1.14
Gain (G)	6.59dB	6.32dB	5.35dB
Antenna size	10× 8 ×0.8mm^3	8.06× 7 ×0.8mm^3	8.06× 7 ×0.8mm^3

Antenna-1 was found to be efficient at its maximum in terms of bandwidth and gain. The fifth generation (5G) applications need a higher gain and a wider bandwidth. Antenna -1 was found to have a higher gain of 6.59 dB and a wider bandwidth of 3.24GHz. Antenna-3's had a lower, 5.35 dB, and its bandwidth was 554.7MHz. Antenna-2 then achieved a high gain of 6.31 dB with a 2.05 GHz bandwidth. The relative permittivity of the substrate was shown to have significant effects on the performance of the antennas. It was shown that an antenna could achieve a lower return loss with lower gains by using a substrate with a greater permittivity value.

TABLE V: Comparative of the proposed antenna with published research papers.

Reference	Dielectric constant	Antenna size (mm^3)	Return loss (dB)	Bandwidth (GHz)	Gain (dB)
[7]	2.2	14.71*7.9*0.254	-12.56	582MHz	6.69
[8]	4.4	7*7*0.8	-39.36	2.48GHz	6.37
[9]	4.4	7*7*0.8	-27.79	2.62GHz	6.59
Proposed antenna	3	10*8*0.8	-20.35	3.24GHz	6.59

5. CONCLUSIONS

The proposed antennas were designed to evaluate the Arlon CLTE-AT, Arlon AD450 and Taconic RF-60 substrate materials and comparison with the aim of achieving good performance in terms of bandwidth and gain while saving a return loss under -10dB and a VSWR below 2. While satisfying the return loss and VSWR requirements at 28 GHz, all of the proposed antennas showed good performance (bandwidth greater than 100 MHz and higher gains). Among the three antennas offered are the conclusion that Arlon CLTE-AT would be the best choice for 5G applications.

REFERENCES

[1] Khraisat, Yahya SH. "Design of 4 elements rectangular Microstrip patch antenna with high gain for 2.4 GHz applications." *Modern applied science* 6.1 (2012): 68.

[2] Khan, Anzar, and Rajesh Nema. "Analysis of five different dielectric substrates on microstrip patch antenna." *International journal of computer applications* 55.14 (2012).

[3] Vickers, R. I. C. H. A. R. D., and T. O. O. M. A. S. Vilmansen. "The evolution of telecommunications technology." *Proceedings of the IEEE* 74.9 (1986): 1231-1245.

[4] Nayak, Anurag, Shreya Dutta, and Sudip Mandal. "Design of Dual Band Microstrip Patch Antenna for 5G Communication Operating at 28 GHz and 46 GHz."

[5] Sagiroglu, Seref, and Duygu Sinanc. "Big data: A review." *2013 international conference on collaboration technologies and systems (CTS)*. IEEE, 2013.

[6] Balanis, Constantine A. "Antenna theory analysis and design, A JOHN WILEY & SONS." *Inc., Publication* 811 (2005).

[7] Mungur, Dheeraj, and Shankar Duraikannan. "Microstrip patch antenna at 28 GHz for 5G applications." *Journal of Science Technology Engineering and Management-Advanced Research & Innovation* 1.1 (2018): 20-22.

[8] Kaeib, Abdalnaser F., Nafaa M. Shebani, and Amer R. Zarek. "Design and analysis of a slotted microstrip antenna for 5G communication networks at 28 GHz." *2019 19th International Conference on Sciences and Techniques of Automatic Control and Computer Engineering (STA)*. IEEE, 2019.

[9] Merlin Teresa, P., and G. Umamaheswari. "Compact slotted microstrip antenna for 5G applications operating at 28 GHz." *IETE Journal of Research* 68.5 (2022): 3778-3785.

A Review of Building a Search Engine Using Image Recognition

7

A Review of Building a Search Engine Using Image Recognition

Amal Omar O.Saa
 Libyan Academy for Postgraduate Studies
Libya-Tripoli
amal.omar@cctt.edu.ly, amal.omar@gmail.com

Abstract

Image recognition is the process of identifying objects, places, persons, writing, and actions in images using software. It has been the subject of extensive research over the past decade and has found many new applications in e-commerce as intelligent assistants. Artificial Intelligence (AI) is replacing ordinary computers and machine learning is being used in various application areas such as disease prediction, weather forecasting, and image recognition. Convolutional Neural Network (CNN) models have been widely used to study images and retrieve the query image from a massive number of images saved in a dataset. CNN is one of the data mining (DM) techniques. Image recognition is based on the features of the image; it searches for the best patterns to get the required image in a short time. Image processing is not an easy concept; it needs to take all image features into account. That's why AI and DM are the best solution for building a great image search engine. This paper reviews the models and their algorithms that have been used to develop the Image search engine in terms of the best techniques to get images

queried. The models are ResNet30/50, ResNet30, Inception V3 and ConvNets.

Keywords: Image recognition, Pattern Recognition, CBIR, neuronal networks, CNN

1. INTRODUCTION

Image recognition has become more dominant, and search using image (image to image) is used in a search engine to find a product that adds the strongest support to e-commerce and online shopping. With so many alternatives available to buyers, it can take a lot of searching to locate one that meets their needs. Since there are so many options available to buyers, it may take some time for them to choose one that suits their needs. Many studies have tried to get the required image based on studying image properties. One of them, V. Ragatha et al. [7], proposed an image-based search engine using techniques for the detection of change of edge, sober filter design, and color coherence vectors (CCV). These techniques are called Content-Based Image Retrieval (CBIR). Y. C. Wahl et al., (2013), proposed a scheme to use the learning feature to include clothing image interpretation that widely used in e-commerce. Reverse image search is a technique for querying the internet for an image to see if any other exact examples are present. More technically, it is a CBIR query method that gives the CBIR system a sample image it will use to base its search. When you upload a picture, it goes through the reverse image search engine's fingerprinting algorithm. The search engine will then try to find the entries with the closest fingerprints, referred to as "image distance". Vissarut Surkarin et al. (2016) suggested a way to categorize and identify clothing types using feature extraction, Speed-Up

Robust Features (SURF) in combination with the Bag of Feature (BoF) [2]-based local discretions patterns (LDP). The query image is compared using a CBIR technique to find the most similar relevant photos between the database of feature vectors and the query image's feature vectors and arrive at the closest relevant images. It can use an image search engine to face many things such as clothing which is a major part of your everyday life; search for information in the server databases is useful in the modern world of fashion. On the other hand, Earth science researchers at NASA developed Worldview search engine tools which camper input satellite images with the saved image in the dataset [2]. Various algorithms have been proposed for the purpose of the feature extraction task by using data mining techniques that have proved to be the most efficient, interactional, flexible and quick image likeness search engine [3]. There are two approaches that can be used as search techniques which are metadata or features.

This paper presents some algorithms that have been proposed for the feature extraction task using a metadata approach. The contents of each image are identified using tags. The images with the metadata that most closely match the query metadata are returned to the user when they attempt to search for images (either using text or another image as input). On the other hand, the second approach is to search by the image features themselves. In this approach, a trained Convolutional Neural Network (CNN) model is used to search by features in the image. The database uses a flexible neural network to extract data using this deep neural network of image recognition, and pattern matching and is very effective in testing fabric prediction. CNN models have many algorithms like Residual Neural Network ResNet30/50 [3]-[5], VGGT16 [5] and InceptionV3 [6] which are based on features Image extraction. This deep neural network is particularly effective at pattern matching, picture

recognition, and fabric prediction testing based on looking for patterns in databases. The image recognition system consists of the standard operational features described in Fig.1.
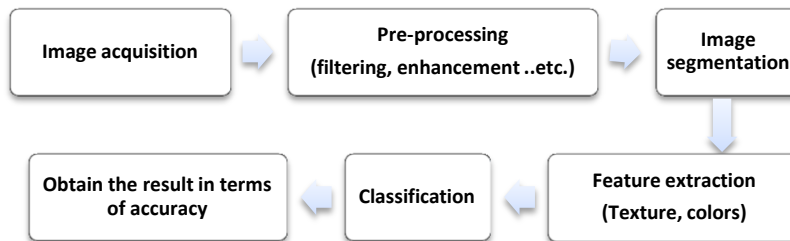
Figure 1: Image Recognition System Adapted from [4]

Image acquisition involves taking an image with the help of different units. A variety of sensors are available such as light sensors, ultrasound, radar, and so on. Before removing an object in image processing, which is based on certain assumptions and conditions like image format, image resolution, color, and size, part of the initial experience with the functionalities includes a histogram of balance conversion, noise reduction, etc.

Segmentation is when processing the image, different image regions are selected and suitable points for further treatment processing are displayed. Feature extraction deals with the information contained in the section that looks like a corresponding sphere for the size of the image or one specific element. Classification is when all elements are classified into multiple categories based on their assets. This paper discusses various techniques and approaches used in image search engines. Three search engines are

presented: Worldview search engine, Reverse Image Search Engine for Garment Industry, and Snapshop-An Image-Based Search Application. Finally, a table summarizing the models used to develop the search engine for the three studies is presented.

A. Snapshot Search Engine

In-depth searches are underway in the field of image recognition, based on the maxim that an image is worth 1000 words. This field of image recognition in visual search will continue to grow in the future. Using advanced computer techniques to achieve higher accuracy, Convolutional Neural Networks (CNNs) are deep learning algorithms capable of capturing the image entry, assigning values (tools and readable selections) to different elements/regions of the image, and separating them. The ConvNets model is used to develop this search engine; it is able to learn these filters/features with proper training. Figure 2 presents the main steps of the CNN process in this section. CNN consist of:

- Convergence (filter) layer: In this layer, the image is define as some of the pixel dimensions (e.g. 3×3, 5×5), and the convolution function is an output of the points defined by the value in the pixel filter.
- Activation layer: This creates a much smaller image size. This feature distributes a nonlinear boot layer to allow the network to train in the background. Sigmoid, SoftMax, Relu, and TANH have activation capabilities.
- Pool (merge) layer: This signifies additional reduction and reduction of matrix volume "remove redundancy." This allows the network to learn faster, focusing on the most significant details in every aspect of the image.

- Fully integrated layer: This is a standard format for multiple-layer perceptron. It works with a group of opportunities associated with anything (e.g., dog, cat, bird).

Every test has proven that CNN in the Image-Net dataset provides the most accurate results and performance. However, it still needs to know something in the form of small ants on a flower stalk. In addition, it finds it hard to distinguish images with filters similar to Instagram filters.   The main problem in image processing is that the image has some features or functionality. As a result, many kinds of image recognition are available for various purposes:

1. Object recognition: This is a way to see one or more previously investigated objects or their classes if they exist in uniform or three spatial dimensions. One example of a search engine is Google.
2. Identification: This is used for identifying a specific object like pointing up somebody's face or defining handwriting digitally.
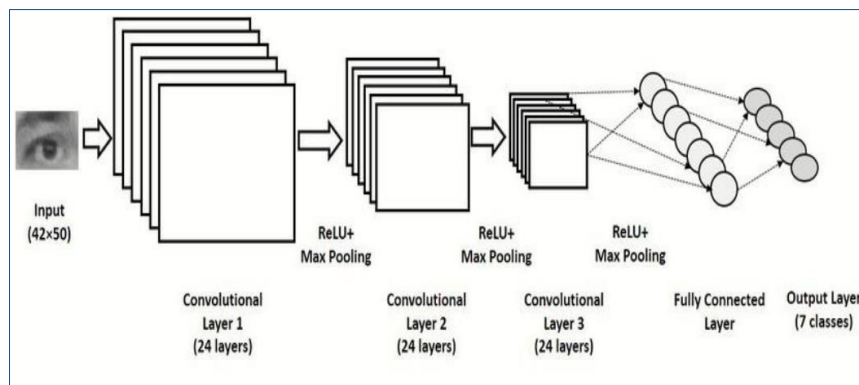
Figure 2: CNN's simple design for fashion

A range of request entry images of various types are taken. The top-4 similar images recovered by boring metric indexing (closest approximation) are tabulated with similarity scores. Similar images, as seen, correspond in terms of color, shape, pattern, texture, and style. The image search engine system can successfully capture features for a wide range of images and deliver accurate results.

Figure 3 shows the Architecture Snapshot-based Search Engine which consists of three layers:

1. **User Interface:** This is an essential part of any user-based application. It helps to engage the users and give them a great experience.
2. **Middle Layer:** This layer includes a web service based on picture recognition.
3. **Dataset Layer:** Dataset Layer: A collection of related data that is organized into some type of data structure.
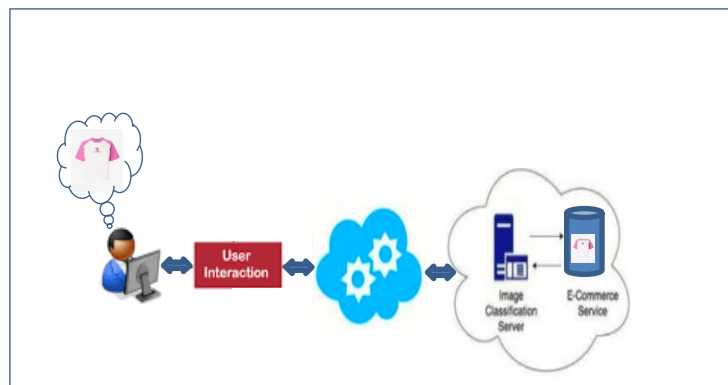
Figure 3: System Architecture Adapted from [4]

B. Worldview search engine

NASA's Earth Observing System Data and Information System (EOSDIS) created an appliance that contains over 52,000 satellite images and about 900 layers saved in a database [3]. This appliance helps users interface with the earth map as layers, which are updated daily. The Worldview search engine is a type of artificial neural network used in image recognition and processing that is specifically designed to process pixel data. The image data is saved as a list of integers called "features". These features are the key to searching for the image. ResNet50 is a CNN model that compares the 2048 data size to 128 features, and the storage data "Annoy library" speed can retrieve data for 5 seconds per query on a single virtual machine (VM) in the cloud. Additionally, the Worldview built UX helps search for the image relatively until it gets the required image. The UX takes a subset from the input image using snipping tool. The search engine in this study is called Pipeline. Pipeline works based on more than 52k images taken from NASA GIBS with zoom 8 and 200 images taken with zoom 4. The images are stored with path file (*.ann) as Annoy python library. The save data algorithm is designed based on binary tree, query speed and organized method. The Annoy search returns indexes of the features that most match the user's query image. These indexes can be converted into a NASA GIBS URL pointing towards the image that the characteristics represent. The application developed is called Flask app. Figure 3 below shows the image search engine steps.
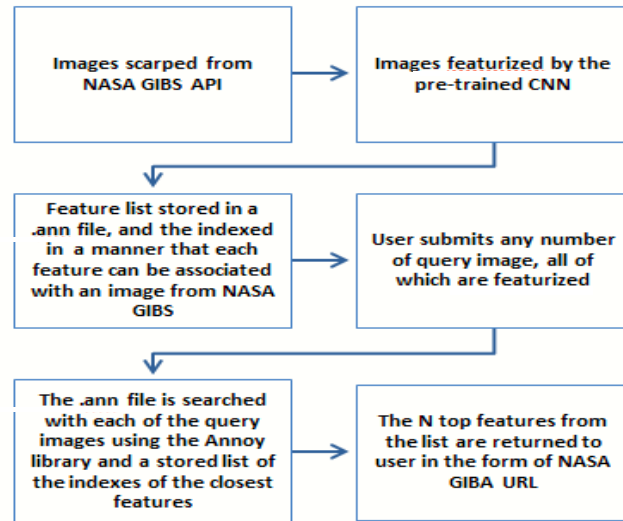
Figure 3: Pipeline of the Reverse Image Search Adapted from [3]

The researchers designed a scalable reverse imagery search system into a cloned version of NASA's Worldview. The ResNet30 model is capable of reversing the search for a larger number of image classes and having a database of several years of images. The current CNN is only applicable to the labeled image classes on which it was created. Further, it would be impractical to label images to form the pattern in a supervised mansion for reverse image research. Scientists would be required to store their image database as a collection of the characteristics of all images and deliver their custom pattern in this file code as (*.h5) because it cannot save all images and manage them.

The researchers have shown that creating a reverse image search system on Worldview is highly feasible. This has allowed us to speed up research while reducing the storage of massive databases of satellite images.

ResNet improved to speed up search along with shrinking the storage of the enormous 6 satellite image databases. Besides that, using a standard ResNet model was not ideal for searching reversed images, as the ResNet model was good when classifying for color but lacked detection of finer features.

C. Garment Industry Reverse Image Search Engine

The garment industry is aiming to enter the world of e-commerce aggressively. However, current search engines such as Google and Bing that search text to text and text to images do not achieve this goal. This study developed an approach consisting of four models for a search engine based on searching image to image, as shown in Figure 4. The four models are listed below:
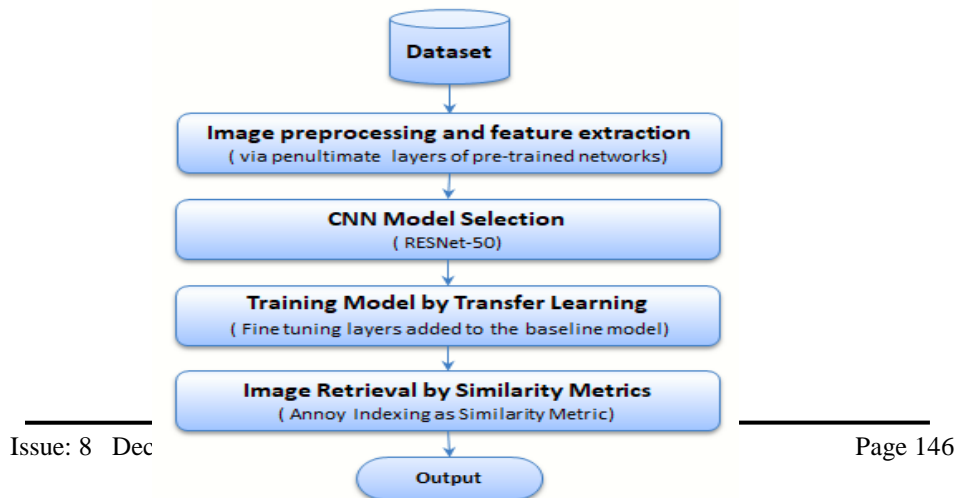
Figure 4: Basic Block Adapted from [3]

1. Image Pre-processing and Feature Extraction: The first module focuses on pre-processing the images in the clothing dataset and extracting relevant features to represent visual information. The images are first resized and then converted into RGB format. Then, they are converted into a numpy representation in 3 dimensions that are centered at zero using the RGB mean values specific to each model. Lastly, the numpy representations are transmitted through the model and the features are extracted from the pre-final layer, before the final classification layers. The feature files are saved in the (.npy) extension.

2. CNN Model Selection: The second module completely compares three pre-formed CNN models VGG16, Resnet50 and InceptionV3 to choose the optimal model for the clothing dataset. The selected CNN model has a significant effect on the extraction of characteristic vectors and the subsequent accuracy of retrieval of similar images.

3. Training Model using Transfer Learning: The third module is the application of transfer learning to refine the selected model to retrieve domain-specific items. The development of the CNN model aims at allowing the selection of layers in the pre-formed CNN model as well as fine adjustment of the CNN model for custom dataset. Viewing feature maps after each convolution block in ResNet-50 helps in deciding the optimal extraction layer. In terms of focus, the ResNet50

pattern until the fully connected layers head is used as the basic pattern to which additional layers are added. The base model is frozen prior to recycling, therefore only added layers are formed on the dataset. The focus process ensures that the model is more personalized to our data set and can capture more subtle features.

4. Fine tuning ResNet-50: The fourth module performs image retrieval for a given query image by using Annoy Indexing as a similarity measure. This example examines the approach. The dataset contains about 4200 images. Unique image identifiers, image URLs, alternative image texts, and product page URLs are also stored for access. ResNet50 displays similar images with better quality than those that are less similar. Elapsed time for extracting original functionality from a subset of the dataset is 1150 seconds. Elapsed time to extract an enhanced feature from a subset of the dataset is 1032 seconds. The similarity optimal metric for the models for accuracy and recovery time are factors that should be considered.

The recovery time is significant here. When it considers a similar search engine, scalability and capacity to process applications as quickly as possible should be implemented. Differences, although small, are more significant on a larger scale. The Annoy indexing process offers faster indexing and optimizes the comparison process by building a rough static tree indexing structure.

The three resulting images corresponding to the query images demonstrating the similarity search process of the image search engine are shown in Table I.

Table I: RESULTS OF SIMILAR IMAGE Adapted from [5]

The differences, although small, are large in scale over time:

- Euclidean Distance: The time elapsed for 10 images for 10 queries are 4.33 seconds.
- Manhattan Distance: The time elapsed for 10 images for 10 queries are 4.76 seconds.
- Cosine Similarity: The time elapsed for 10 images for 10 queries are 3.83 seconds.
- Annoy Indexing: The time elapsed for 10 images for 10 queries are 3.45 seconds.

2. Discussion

Deep convolutional neural networks (CNNs) are the dominant technology in computer vision nowadays. Unfortunately, it's not clear how different from each other the best CNNs really are. The results from processing algorithms are getting the same features. The selection of the training set may be more important than the selection of the algorithm.

The table below summarizes three studies that provided search engine images based on the model or algorithm used in search engine development and techniques.

Table II: Summery of Models

No	Study	Techniques (Model)	algorithms	Advantage	Disadvantage
1	A Worldview search engine	- CNN	-ResNet	-Using CNN enhancement features color in the satellite image. -High-speed and efficient storage.	The system is not able to generate rules without learning from datasets to generate rules.

2	A Reverse Image Search Engine for Garment Industry	- CNN - Boring indexing algorithm (non-supervisory, non-linear Spotify music recovery algorithm)	- ResNet -VGG16 - Inception V3	It successfully researched accurate similar images for the clothing industry.	CNN models extract image characteristics, including background, such that a noisy background leads to confusion.
3	A Snap-shop An Image Based Search Application	- CNN Classification (supervised)	- ResNet	- The features cover his ability to search for images at a much more specific level than metadata.	-

3. Conclusion

This paper tried to figure out the answer to our research question building a search engine using image recognition. It examined three studies showing the model and method used to build an image search engine. These studies are Worldview search engine, Reverse Image Search Engine for Garment Industry, and Snapshot-An Image-Based Search Application. However, the image recognition service is the basic functionality of the app that enables users to extract visual information from images.

The technology and models used in the image search engine in these studies are CNNs which are a subset of machine learning and are at the heart of deep learning algorithms. They are part of data mining techniques and create an adaptive system that computers use to learn from their mistakes and improve continuously. Thus, artificial neural networks attempt to solve complicated problems like summarizing documents or recognizing faces with greater accuracy. Their uses of the CNN models are successful, but the lack of exploration of similarity measures diminishes the limit for their implementation. Image recognition is a field of computer vision that has been growing rapidly in recent years. It has many applications, including building search engines based on image recognition. Future work, it can build an image search engine using deep learning models such as CLIP model. CLIP is a neural network built to learn image features through natural language supervision. The finished engine is quick and accurate.

References

[1]   S. Jain and J. Dhar "Image based search engine using deep learning" 2017 Tenth International Conference on Contemporary Computing (IC3), 2017, pp. 1-7, doi: 10.1109/IC3.2017.8284301.

[2]   M. Seeley, F. Civilini, N. Srishankar, S. Praveen, A. Koul, A. Berea, and H. El-Askary "Knowledge Discovery Framework"

2020.

[3]   A.Sodani ,M.Levy,A.Koul, M.An and K.Ganju "Scalable Reverse Image Search Engine for NASA Worldview" 10 Aug 2021.

[4]   Karan D. Argade , Dhanashree M. Gaware, Prajkta S. Umap, Savita P. Nalawade , Snehal Baravkar "Snapshop-An Image Based Search Application", International Journal of Scientific Research in Science and Technology Print ISSN: 2395-6011 | Online ISSN: 2395-602X,Published : 17 June 2021 , URL: https://www.academia.edu/4 9659377/Snapshop_An_Ima ge_Based_Search_Applicati on, accessed date:5 May 2022.

[5]   A.Eswaran and Varshini E "Reverse Image Search Engine for Garment Industry" 2022 8th International Conference on Advanced Computing and Communication Systems (ICACCS), Authorized licensed use limited to: UNIVERSITY OF STRATHCLYDE, Downloaded: July 16, 2022 at 09:35:38 UTC from IEEE Xplore. Restrictions apply.

[6]   C. Szegedy, V. Vanhoucke, S. Ioffe, J. Shlens and Z. Wojna, "Rethinking the Inception Architecture for Computer Vision" 2016 IEEE Conference on Computer Vision and Pattern Recognition (CVPR), 2016, pp. 2818- 2826, doi: 10.1109/CVPR.2016.

[7]   Venkata, Divya & Yadav, Divakar. (2012) "Image Query Based Search Engine Using Image Content Retrieval" International Conference on Modeling and Simulation .0.1109/UKSim.

2012.48.

[8]   Modeling and Simulation. 10.1109/UKSim.2012.48. [3] A. Nodari, M. Ghiringhelli, A. Zamberletti, M. Vanetti, S. Albertini and I. Gallo "A mobile visual search application for content based image retrieval in the fashion domain" 2012 10th International Workshop on Content-Based Multimedia Indexing (CBMI), 2012, pp.

[9]   J.Wu and LAMDA Group "Introduction to Convolutional Neural Networks" Namjing Universtity, China.

[10]   "Building a powerful Image Search Engine for your pictures using Deep Learning", published: 22Jul 2021,URL: Building a powerful Image Search Engine using DL | CodeX (medium.com), accessed 8 Jun 2023.

Analysis and Implementation of Video Compression using MPEG Standard

8

Analysis and Implementation of Video Compression using MPEG Standard

Elbahlul Fgee
Department of Electrical Engineering and Computer, Libyan Academy for Postgraduate Studies, Libya

 Aboagela Dogman
Department of Networking, Faculty of IT, University of Zintan, Zintan, Libya

Naima Agnash
Department of Electrical Engineering and Computer, Libyan Academy for Postgraduate Studies, Libya
agnashnaima@gmail.com

ABSTRACT

Multimedia applications have been growing rapidly over the past decades. Saving and transmitting uncompressed version of these applications may not be practical. This is because they require large storage space as well as dedicated bandwidth for transmission. Therefore, there was a need to compress these applications, in particular video applications in effective manner.

Video codec is defined as the process of compression and decompression of digital video files. Several standards were introduced for video compression. The most widely implemented standards are MPEG-x family, and H.26x family.

In this paper, the implementation of video MPEG codec was performed using MATLAB software. The results show the process of MPEG compression starting from splitting the video into sequences frame, converting each frame into $YCbCr$ format, applying motion

prediction, performing transformation and quantization, and finally applying entropy coding via Run Length Encoding, and Huffman algorithm. Although, the compression ratio was around 20%, the results show trivial difference between original frames and reconstructed frames. The Peak Signal-to-Noise Ratio PSNR is used to measure the quality between the original and a compressed frame. The average PSNR was around 41.02 which is showing good quality of compressed frame.

Keywords: MPEG, DCT, quantization, RLE, and Huffman algorithm.

1. INTRODUCTION

Over the past decade, there has been a rapidly increase in the use of video in digital form. This is due to the extensive use of the Internet world wide. Video can be seen as a sequence of images which are displayed in order. Each of these images is called a frame. However, there are minor changes in the consecutive frames such as a slight difference in the color. Therefore, video compression standards do not encode all the information in the video. some of this information are redundant and can be eliminated, some of them are not important and may loss during the compression [1].

Video compression techniques can be classified to lossy and lossless compression techniques. Lossless compression technique is used to encode computer originated data files whereas lossy compression is used to encode audio, and video files. There are a variety of lossy compression standards. The most widely implemented standards are MPEG-x family, and H.26x family [2]. In this paper, the implementation of video MPEG codec was performed and analyzed using MATLAB software.

1.1. MPEG STANDARD

MPEG stands for "Motion Picture Expert Group". As its name implies, MPEG is one of the most widely deployed compression schemes used for encoding video, movies, and motion pictures. The video files that have extensions of MP4, and audio files that have extensions of MP3 are compressed by MPEG standard [2].

MPEG has different set of standard. These includes: MPEG 1, 2, 4, and 7. MPEG-1 was published in 1992. MPEG-1 aimed to provide VHS quality with a bandwidth of 1,5 Mbps. MPEG-2 was released in 1994, which allowed a higher quality with a slightly higher bandwidth. MPEG-4 was released in 1998 which in turn provided lower bit rates (10Kb/s to 1Mb/s) with a good quality. MPEG-7 is well known as multimedia content description interface. It is a suite of standards for description and search of audio, visual and multimedia content [3] – [6].

MPEG applies similar techniques as JPEG expect the prediction of motion. This is because the video is a series of successive frames. Figure (1) illustrates the JPEG diagram. The process starts with converting each frame into $YCbCr$ format, performing transformation and quantization, and finally applying entropy coding via Run Length Encoding, and Huffman algorithm
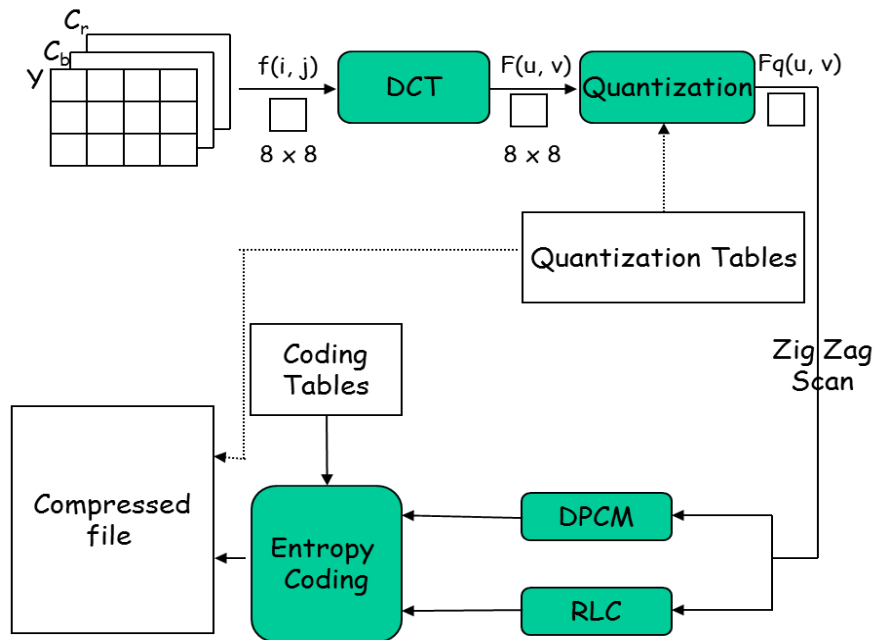
Figure 1: JPEG Pipe Line Diagram [7].

2. RELATED WORKS

Several studies have been carried out on video compression. For instance, performance evaluation of entropy coding for MPEG-4 video codec was studied. In their paper, algorithm for Context Adaptive Binary Arithmetic Coding (CABAC) is proposed for MPEG-4 Video Codec. They stated that the compression efficiency can be up to 30% better when compared to traditional entropy coding technique [4]. Performance analysis of various video compression standards were examined in [5], between MPEG, and H.264.

In [6], performance analysis of various video compression techniques was carried out. They compared MPEG-2, H.261, and H.264 video compression standards. the results showed that the compression of H.264 is better than MPEG-2 and H.261.

In this study, the implementation and analysis of MPEG video codec was examined using MATLAB. The following sections explain the MPEG compression steps, the experimental procedure for implementing and analysing MPEG by MATLAB, the discussion of obtained results, and the finally the study conclusion.

3. MPEG COMPRESSION STEPS

The encoding process of MPEG is performed in two main stages: first stage is to prepare data for MPEG compression. This includes the resolution reduction of video frames which results in dividing each frame into macroblocks.

The second stage is to apply MPEG compression on the prepared data. This stage includes: applying motion predication at macroblocks level. Then, the Discrete Cosine Transformation (DCT), quantization, and zig-zag operation are used to reduce the spatial redundancy. Finally, the entropy coding using the Run Length Encoding (RLE) and the Huffman coding algorithm are applied to the output of quantization [1] – [2].

3.1 DATA PREPARATION IN MPEG

Data preparation in MPEG includes: the resolution reduction which is the change of each video frame from Red, Green, Blue (RGB) format to YCbCr format (luminance and chrominance). YCbCr format is in turn divided into macroblocks [1]

3.1.1 CONVERT RGB TO YCbCr

The colour image is mainly composite of three colors Red, Green, and Blue. Each pixel of the image is a mixed from these colors with different scale. The RGB coordinates represents the three-dimensional of the point of the given color within the cube or its faces or along its edges as shown in Figure (2).
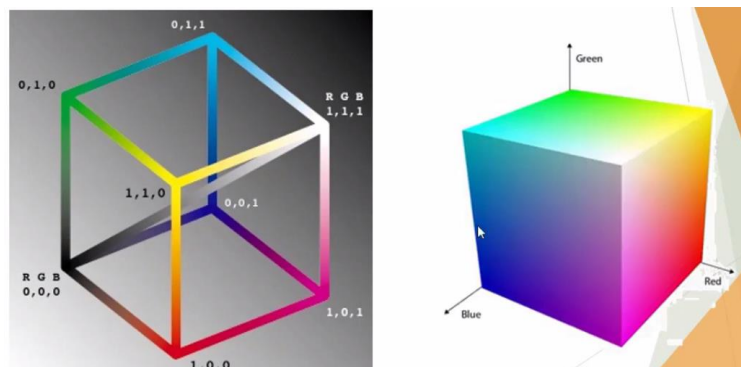
Figure 2: RGB coordinates [8].

Each frame (single image) in the video is represented in RGB model. This model must be changed to a digital form in order to be compressed. RGB model must be changed to YC_bC_r model. Where Y is the luminance of the image that represents the brightness. C_b is the chrominance of the image that represents the difference between gray and blue whereas C_r is the chrominance of the image that represents the difference between gray and red [7]. The following equation is used to covert the image from analog form (YUV) into digital form (YC_bC_r) [8].

$$\begin{bmatrix} Y \\ Cb \\ Cr \end{bmatrix} = \begin{bmatrix} 0.299 & 0.587 & 0.114 \\ -0.169 & -0.334 & 0.500 \\ 0.500 & -0.419 & -0.081 \end{bmatrix} \begin{bmatrix} R \\ G \\ B \end{bmatrix} + \begin{bmatrix} 0 \\ 128 \\ 128 \end{bmatrix} \qquad (1)$$

The advantage of YC_bC_r is that it can be compressed using a ratio of 4:2:2 or 4:2:0 in contrast with RGB which is compressed using 4:4:4 ratio.

There are two system of YC_bC_r. The NTSC system which has resolution of $Y = 352 * 240$ and $C_b = C_r = 176 * 120$, and PAL

system which has resolution of $Y = 352 * 288$ and $C_b = C_r = 176 * 144$ [9].

3.1.2 DIVISION INTO MACROBLOCKS

After each frame is converted into a digital form YC_bC_r, it is divided into many blocks called Macroblocks. The Macroblocks of 16*16 samples represent the luminance components whereas Macroblocks of 8*8 represent the chrominance components as shown in Figure (3). The macroblocks are then used as inputs to Discrete Cosine Transformer (DCT) at the compression stage [9].
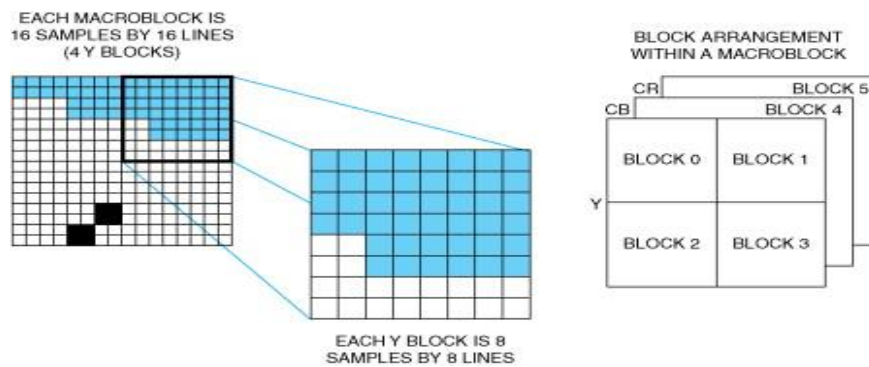
Figure 3: Macroblocks for luminance and chrominance

components [9]

3.2 DATA COMPRESSION IN MPEG

The compression process includes six operations: apply motion prediction, Discrete Cosine Transformer (DCT), Quantization, Zig-zag, and entropy coding using the Run Length Encoding (RLE) and the Huffman coding algorithm. The following subsections details these operations.

3.2.1 APPLY MOTION PREDICTION

An MPEG video is a sequence of frames which often have small differences between them. Thus, the MPEG-standard reduces this temporal redundancy by considering three types of frames: I-frames (intra), P-frames (predicted) and B-frames (bidirectional).

The I-frame is an independent frame which has no reference to other frames. It is composed onto blocks of 8x8 pixels and sent directly to DCT.

The P-frames can be predicted using forward prediction which is based on an earlier I-frame or P-frame. A motion vector is calculated to determine the value and direction of the prediction. A motion vector is composed to 8x8 pixels blocks and sent to the DCT.

The B-frames can be predicted using bidirectional prediction which used based on previous or next P-frame. Thus, two motion vectors are calculated. One to determine the value and direction of the forward prediction, and the other to determine the value and direction of the backward prediction. The motion vectors are composed to 16x16 pixels blocks and sent to the DCT. The set of I frame, P frame, and B frame makes Group of Picture GoP as shown in Figure (4) [2] [9].
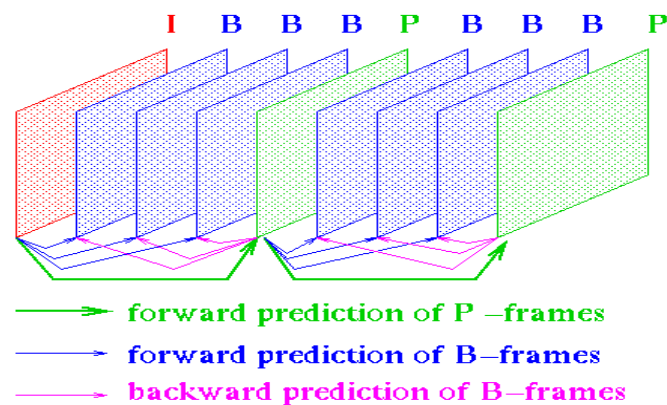
Figure 4: GoP in MPEG [2].

3.2.2 DISCRETE COSINE TRANSFORMER (DCT)

According to [8], DCT is linear transformer function which is used to convert sets of numbers $(a_0 + a_1 + a_2 + \cdots + a_{n-1})$ into frequency domain called coefficients $(w_0 + w_1 + w_2 + \cdots + w_{n-1})$. The results are data that can be represented by a set of coefficients $(w_0 + w_1 + w_2 + \cdots + w_{n-1})$.

The main advantage of DCT is that the power of original data $(a_0 + a_1 + a_2 + \cdots + a_{n-1})$ may be concentrated by few coefficients depending on the correlation of original data. In other words, most of DCT coefficients can be zero or values near to zero.

There are two main coefficients generated from DCT: DC coefficient, and ACs coefficients. The DC is the most important coefficient whereas ACs start from most important coefficients to the least important coefficients. Equation (2) is used to calculate the DC coefficient for $k = 0$

$$w_0 = \frac{(a_0 + a_1 + a_2 + \cdots + a_{n-1})}{\sqrt{n}} \qquad (2)$$

Where $a_0 \ldots a_{n-1}$ represent set of number , w_0 represent the weight of DC coefficient.

The rest of coefficients where $k > 0$ are called ACs coefficients. Equation (3) is used to calculate the AC coefficients for $k = 1{:}\,\mathrm{n} - 1$, Where $a_0 \ldots a_{n-1}$ represent set of number n , w_k represent the weight of k AC coefficient.

$$w_k = \sqrt{\frac{2}{n}} \sum_{t=0}^{n-1} a_t \cos\left[\frac{\pi}{n}\left(t + \frac{1}{2}\right)k\right] \; k$$
$$= 0, 1, \ldots \ldots n - 1 \qquad (3)$$

3.2.3 QUANTIZATION

Quantization is defined as the process of reducing the number of bits needed to store an integer value by reducing the precision of the integer. Quantization matrix is calculated by dividing each coefficient of the DCT output on the corresponding element of the quantization table [1]. Equation (4) is used to calculate the quantized matrix.

$$\text{Quantized matrix} = \frac{Output\ of\ DCT}{Quantization\ table} \qquad (4)$$

The elements of quantization arrays are constant for luminance and chrominance as shown in Table (1) [1].

Table 1: Quantization Table [1]

(a) For Luminance

16	11	10	16	24	40	51	61
12	12	14	19	26	58	60	55
14	13	16	24	40	57	69	56
14	17	22	29	51	87	80	62
18	22	37	56	68	109	103	77
24	35	55	64	81	104	113	92
49	64	78	87	103	121	120	101
72	92	95	98	112	100	103	99

(b) For Chrominance

17	18	24	47	99	99	99	99
18	21	26	66	99	99	99	99
24	26	56	99	99	99	99	99
47	66	99	99	99	99	99	99
99	99	99	99	99	99	99	99
99	99	99	99	99	99	99	99
99	99	99	99	99	99	99	99
99	99	99	99	99	99	99	99

3.2.4 ZIG-ZAG SCANNING

The zig-zag scanning as shown in Figure (5) is applied on the quantized DCT coefficients. The same pattern is used for luminance and chrominance matrix. The purpose of zig-zag is to organize the quantized DCT coefficients in such a way to be ready for conversion into single dimensional matrix by RLE [10].

Figure 5: Zig-zag pattern

3.2.5 RUN LENGTH ENCODING

Run-length encoding (RLE) is defined as a lossless compression method. RLE represents data sequences by displaying redundant data in a single data value representing the repeated block, and how many times it appears in the image. The outputs of zig-zag scanning are the inputs of RLE [10]. As an example of RLE, the string of AAAAAABBCCCDDD can be encoded using RLE to be A6B2C3D3.

3.2.6 ENTROPY CODING

In entropy coding in Ref [12], DC components are differentially coded as (Size, Value). The code for Value is derived from Size_and_Value Table as shown in Table (2) whereas the code for Size is derived from Huffman Table for DC component SIZE field as shown in Table (3).
AC components (range –1023 - 1023) are coded as pairs (S1, S2): S1 is (Run Length/SIZE), where Run Length is the length of the consecutive zero values [0..15], and SIZE is the number of bits needed to code the *next* nonzero AC component's value [0-A]. (0,0) is the End

of Block for the 8x8 block. S2: (Value) is the value of the AC component.

S1, and S2 are using Huffman Table for AC Run/Size Pairs as shown in Table (4) [12].

Table 2: size and value table [12]

SIZE	Value	Code
0	0	---
1	-1,1	0,1
2	-3, -2, 2,3	00,01,10,11
3	-7,…, -4, 4,…, 7	000,…, 011, 100,…111
4	-15,…, -8, 8,…, 15	0000,…, 0111, 1000,…, 1111
11	-2047,…, -1024, 1024,… 2047	…

Table 3: Huffman Table for DC component SIZE field [12]

SIZE	Code Length	Code
0	2	00
1	3	010
2	3	011
3	3	100
4	3	101
5	3	110
6	4	1110
7	5	11110

Table 4: Huffman Table for AC Run/Size Pairs [12]

R/S	Length	Code	R/S	Length	Code
0/0	4	1010			
0/1	2	00	1/1	4	1100
0/2	2	01	1/2	5	11011
0/3	3	100	1/3	7	1111001
0/4	4	1011	1/4	9	111110110
0/5	5	11010	1/5	11	11111110110
0/6	7	1111000	1/6	16	1111111110000100
0/7	8	11111000	1/7	16	1111111110000101
			1/8	16	1111111110000110

4. EXPERIMENTAL PROCEDURE

MPEG Codec introduced by [13] was implemented and further developed using MATLAB [14]. In MPEG Codec the functions of Encoder.m and Decoder.m were based on other helper functions which was written to perform a specific task for Encoder or Decoder function. Table (5) shows task for each helper functions.

Table 5: Helper function for MPEG codec [13]

Helper function	Task
exhaustiveSearchAlgorithm.m	This function is required for Motion Compensation
differentialCoding.m	This function is used to find the difference between successive frames
zigZag.m	This function function performs RLE
inverseZigZag.m	This is the inverse function of zigZag.m
inverseDifferentialCoding.m	This is the inverse function of differentialCoding.m
inverseDCT. M	This the inverse function of DCT
inbuildDecoder.m	This function is used in line with Decoder.m

The MPEG codec reads uncompressed video and split it into frames in RGB format. The RGB format is then converted to $YCbCr$ format. The luminance components that retains maximum information is left out of the compression whereas high compression is applied to chrominance components.

The Display.m function was added to MPEG codec in order to clearly identify each step of MPEG compression. The README.m can be run to invoke the whole project.

5. RESULTS AND DISCUSSION

In this study, Wildlife Windows 7 Sample Video found in [15] was compressed. The uncompressed video was read and split into frames in RGB format. Figure (5a) shows the original uncompressed frame in

RGB format whereas Figures (5b) – (5d) show the original uncompressed frame with the three colors red, green, and blue respectively. In order to transform frame through DCT, it must be changed to $YCbCr$ format. Figure (6a) shows the original frame in $YCbCr$ format. Figure (6b) shows the Luminance component of the frame that represents brightness whereas Figure (6c) shows the variance chrominance between gray and blue, and Figure (6d) shows the variance chrominance between gray and red.

After the frame is converted into a digital form YC_bC_r, it is divided into many blocks called Macroblocks. The Macroblocks of 16*16 samples represent the luminance components whereas Macroblocks of 8×8 represent the chrominance components.
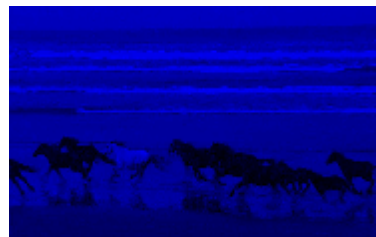

(a) Original frame in RGB

(b) Original frame in Red format

(c) Original frame in Green format

(d) Original frame in Blue

Figure 5: Original frame in: (a) RGB, (b) Red, (c) Green, (d) Blue

(a) Original frame in YCbCr format

(d) Luminance component Y

(b) Chrominance component Cb
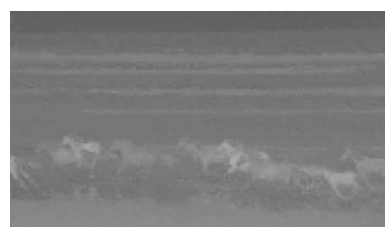
(c) Chrominance component Cr

Figure 6: (a) YCbCr format, (b) Luminance component Y, (c) Chrominance component Cb, (d) Chrominance component Cr

Table (6) represents sample of chrominance component Cb with Macroblock size of 8×8. The values of Macroblock represented in Table (6) were processed by DCT in order to produce DCT coefficients which are presented in Table (7). The output coefficients of DCT are further quantized to produce the quantized DCT coefficient which are presented in Table (8). The assumption is that the quantization table of chrominance has a value of 14.

Table 6: Sample Macroblock (8×8) of chrominance component Cb

126	126	127	120	118	121	125	122
121	119	123	114	113	117	120	119
121	120	125	117	114	119	121	119
128	128	132	124	122	129	130	127
128	126	135	125	124	129	131	130

119	119	130	120	119	126	127	125
117	118	129	122	125	133	135	131
122	123	134	130	130	138	139	137

Table 7: Corresponding DCT coefficients of Sample Macroblock in Table 6

-9.6243	14.4610	-12.2500	10.6860	-4.8039	14.4470	18.5000	0.9535
1.7381	-1.8370	13.9920	-1.7498	-6.8625	0.7866	1.4442	-1.4091
-0.3572	0.5194	-7.4471	-0.8878	6.9105	0.4036	2.3097	-0.4823
-0.5983	0.4884	-3.3931	-1.6237	-1.8615	0.2329	2.1243	-0.1370
0.5576	-0.3779	16.7500	0.2141	0.2310	0.5656	0.0000	0.0150
0.8659	-1.0106	-1.4986	-0.9634	1.0935	-0.4602	-0.6337	0.4010
-1.9053	1.9316	2.2729	0.1361	-3.1124	-0.7794	-0.9567	0.1836
1.2236	-1.2587	-4.4957	0.0794	1.6727	-0.1818	-0.0114	-0.7866

Table 8: Corresponding quantized values of DCT coefficients in Table 7

0	1	0	0	0	1	1	0
0	0	0	0	0	0	0	0
0	0	0	0	0	0	0	0
0	0	0	0	0	0	0	0
0	0	1	0	0	0	0	0
0	0	0	0	0	0	0	0
0	0	0	0	0	0	0	0
0	0	0	0	0	0	0	0

The values presented in Table (9) are the values of Macroblock (8×8) of chrominance component Cb for reconstructed frame. These values are corresponded to the values of Macroblock (8×8) of chrominance component Cb of the original frame presented in Table (6).

Figure (7a) shows the reconstructed frame in $YCbCr$ format whereas Figure (7b) – (7d) show Luminance and chrominance components ($CbCr$) for the reconstructed frame respectively. In Figures (8a) – (8d), the reconstructed frame in RGB format with the three colors red, green, and blue are presented.

Table 9: Macroblock (8×8) of chrominance component Cb for reconstructed frame

127	126	128	119	117	123	125	123
121	120	123	114	112	118	120	118
120	120	125	116	114	120	122	120
128	127	133	124	122	128	130	128
128	127	135	126	124	130	132	130
118	120	130	121	119	125	127	125
116	118	129	123	124	133	135	130
122	124	135	129	130	139	141	136

Figure (9) shows the difference between the original frame and the reconstructed frame. In this study, the Peak Signal-to-Noise Ratio PSNR is used to measure the quality between the original and a compressed image. PSNR was computed between the two frames shown in Figure (9). The value of PSNR is 41.02. Typical values for the PSNR (30 - 50) db [16]. Therefore, The higher the PSNR, the better quality of the compressed, or reconstructed frame.
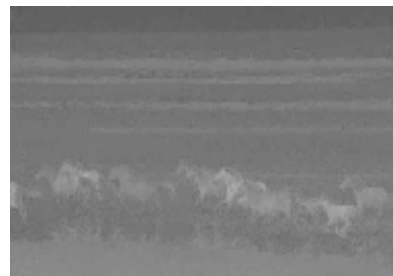
(a) reconstructed frame in YCbCr

(b) Luminance component Y

(c) Chrominance component

(d) Chrominance component Cr

Figure (7): (a) reconstructed YCbCr format, (b) Luminance component Y, (c) Chrominance component Cb, (d) Chrominance component Cr

(a) Reconstructed frame in RGB

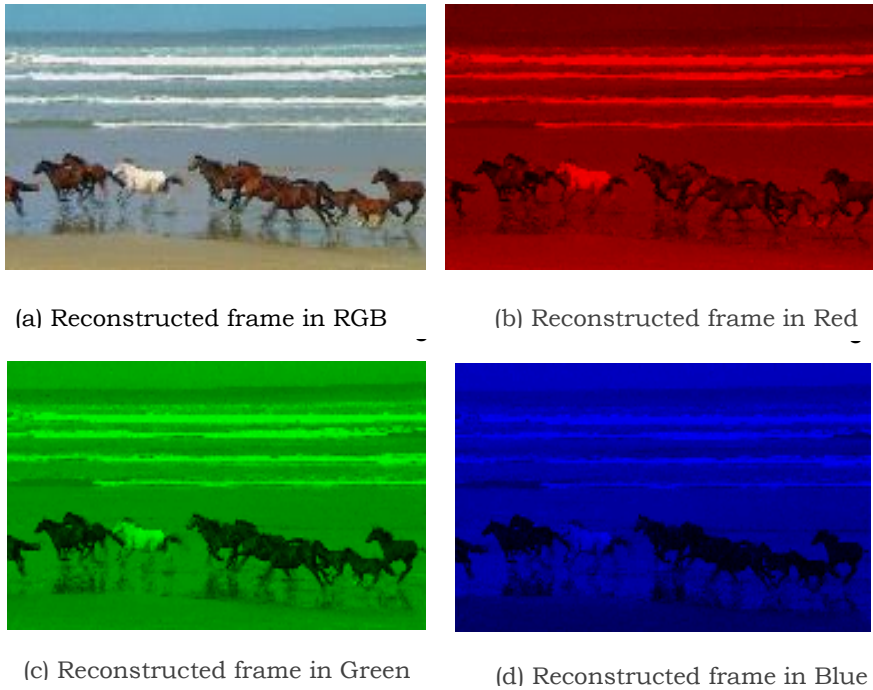(b) Reconstructed frame in Red

(c) Reconstructed frame in Green

(d) Reconstructed frame in Blue

Figure 8: Reconstructed frame in: (a) RGB, (b) Red, (c) Green, (d) Blue

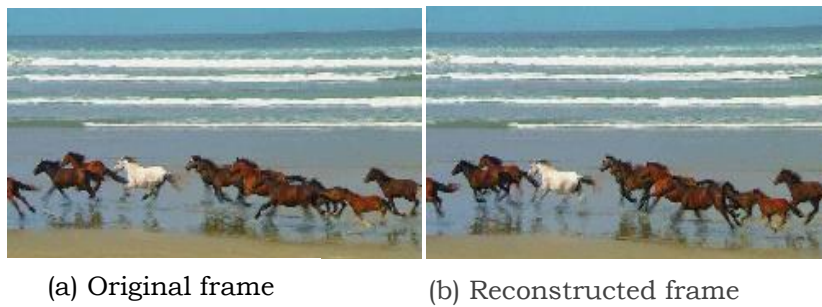
(a) Original frame

(b) Reconstructed frame

Figure 9: comparison between: (a) Original frame, and (b) reconstructed frame

Figure (10) shows the predicted motion vector which is associated with frame presented in figure (9a).
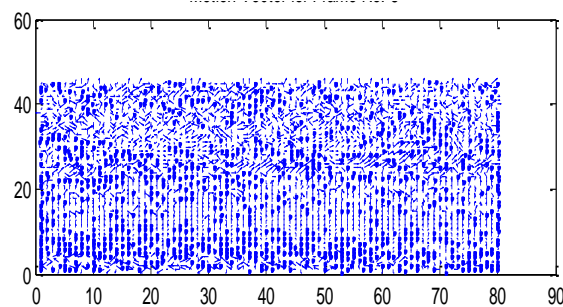
Figure (10): The motion vector of the frame in figure (9a)

6. CONCLUSION

In this study, an implementation of video MPEG codec was carried out. The results show the process of MPEG compression starting from splitting the video into sequences frames, converting each frame into $YCbCr$ format, applying motion prediction, performing transformation and quantization, and finally applying entropy coding via Run Length Encoding, and Huffman algorithm. The PSNR was used to measure the quality between the original and reconstructed frames as the higher PSNR represents better quality of the compressed frames. The average of PSNR was around 42.08.

REFERENCES

[1]   Z., Fan, and D. R. Bull "Intelligent image and video compression: communicating pictures". Academic Press, 2021.

[2]   A D Marshall, "MPEG compression", available online at https://users.cs.cf.ac.uk/dave/Multimedia/node255.html, accessed on 20/12/2022.

[3]   F. Chad, D. J. LeGall, J. L. Mitchell, and W. B. Pennebaker. " MPEG video compression standard ", Springer Science & Business Media, 2007.

[4]   R. Nigam, A. Mishra, A.K. Diwakar, " Performance evaluation of entropy coding for MPEG-4 video codec" International Advanced Research Journal in Science, Engineering and Technology, Vol. 1, Issue 4, December 2014

[5]   R. G. Deshpande and L. L. Ragha, "Performance analysis of various video compression standards," International Conference on Global Trends in Signal Processing, Information Computing and Communication (ICGTSPICC), Jalgaon, India, pp. 148-151, 2016.

[6]   A. Gupta, D. Goyal, and N. Hemrajani " Performance Analysis of Various Video Compression Techniques", International Journal of Science and Research (IJSR), Vol(2), Issue(8), pp 335 – 338, 2013.

[7]   S. Asadollah, R. Bahrampour, M. S. Rostami, and M. A. Mobarhan. "Evaluation of Huffman and arithmetic algorithms for multimedia compression standards." (IJCSEA), 2011.

[8]   Discrete Cosine Transform and Image Compression part 1, available online at: https://www.youtube.com/watch?v=gQHwvJ9Lvno, accessed on 29/12/2022.

[9]   Motion Picture Expert Group, MPEG compression steps, available online at:

https://www.youtube.com/watch?v=lAkuix41XJ8,   last accessed on 29/12/2022.

[10]   L. Tan, J. Jiang "Digital Signal Processing" Second Edition, 2013.

[11]   MPEG   Video   Compression,   available   online   at: http://www.bretl.com/mpeghtml/mpeg2vc.HTM last accessed on 29/12/2022

[12]   Image   Compression   Standards,   available   online   at: https://www.slideserve.com/rmoriarty/image-compression-standards-jpeg powerpoint-ppt-presentation, last accessed on 29/12/2022

[13]   C.   Prabhudesai   "MPEG/H.264/HEVC   Video   Codec   in MATLAB",   available   online   at https://github.com/rite2hhh/MPEG-Codec   last   accessed   on 21/12/2022

[14]   MATLAB R2013a Student Version (32-bit), available on at: https://uk.mathworks.com/matlabcentral/answers/98268-how-do-i-download-matlab-and-other-mathworks-products,   last accessed on 15/12/2022

[15]   Wildlife   Windows   7   Sample   Video,   available   online   at: https://www.youtube.com/watch?v=a3ICNMQW7Ok, accessed on 31/12/2022

[16]   K., Sergey, M. Zriakhov, V. Lukin, and B.Vozel. "MSE and PSNR prediction for ADCT coder applied to lossy image compression." IEEE 9th International Conference on Dependable Systems, Services and Technologies (DESSERT), pp. 613-618, 2018.

Designing a Control System for an Olive Squeezer Process Using the Controller PLC.

9

Designing a Control System for an Olive Squeezer Process Using the Controller PLC.

Monthir Mohammed Mafouth
Electronic Technology College Tripoli, Libya
mondiranwir@gmail.com

Abstract

Um alramel olive squeezer factory is investigated to turn over the old monitoring and control regime to the Programmable Logic Controller. New development was submitted especially in washing stage for environmental reason in which enabling the recycling of used water. And also to eliminate interference of human and machine that cause some difficulties in the process. The project presents a solution and a future upgrade process to the control task of the factory. It presents a set of solution to some technical difficulties in some parts of the factory. These solutions include the addition of certain components to the process. The project also allows full monitoring of the process that helps in controlling it from a central control unit contrarily to the old control process where works needed to relocate between different places for each stage. A Model is fabricated in a way to simulate the squeezer operation and explain its working principle. It also shows the additional tools and developments carried out on the squeezer to make it fully automatic. It includes the addition of sensors, switches and actuators. The fabricated model can also be used in real time monitoring of the system from a centralized location.

**Keywords**: Olive Squeezer Process – control system – Controller PLC.

1. Introduction

Olives are known to humans since ancient times. They are considered as one of the oldest foods known to mankind. The increased demand for olive oil led to the existing of olive squeezers. Old squeezers

require a certain number of labors to manually operate the squeezer. Nowadays, great developments have occurred on the fields of industry and production. These developments have a great impact on the industry allowing for a much improved productivity and reduced cost and risk. The olive oil industry can also benefit from these developments like the design and implementation of an automated olive oil squeezing machine which has a vital role in the area of olive derivatives production that can enhance productivity, reduce cost and allow future upgrading on the system. This machine works with a mechanism of taking olives and producing olive oil after passing through different processes such as; washing, suction, cracking, knead and many others.

In this study, many electrical components are added to the squeezer in order to ease monitoring for the production process.

The monitoring process of the squeezer is achieved automatically. Additional components are installed to connect the stages with each other and to ease the monitoring process allowing transition between stages to be more reliable when the system is controlled using PLC.
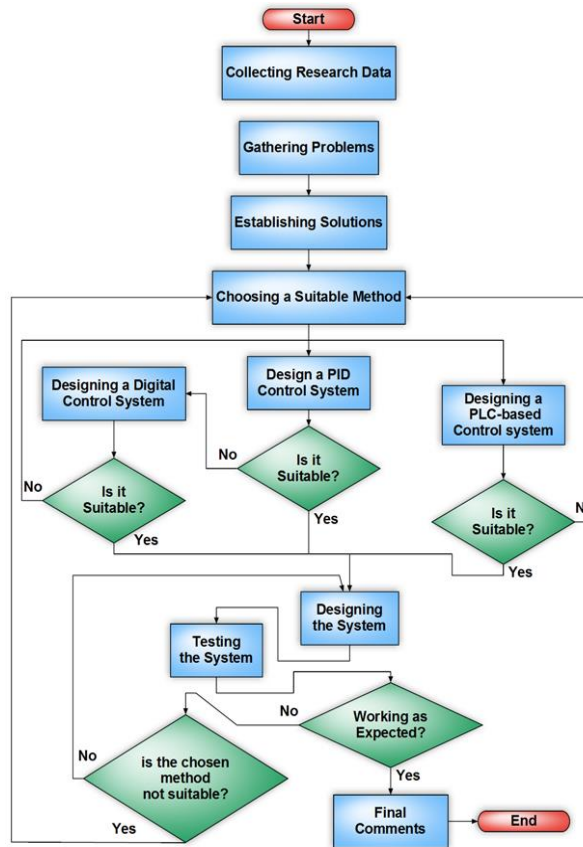
خطأ! لا يوجد نص من النمط المعين في المستند. Flow chart 1 project flow chart.

2. Olive manufacturing terminology

Olives pass through different stages within olive squeezers before finally producing olive oil. These stages include, and not limited to, washing, cracking, mixing and filtering.

- **Squeezing**: In this stage, squeezers wash and then crack olives to produce a paste that is ready to be mixed. After mixing the paste, it gets pressed to separate the fluids from solid

impurities before refining these fluids to produce pure olive oil.

- **Vegetal water**: The produced paste from squeezing olives consists of liquids and solid impurities. Solid impurities are called pomace and the liquids are mix between olive oil and vegetal water. The liquids get filtered using special filters to separate the oil from vegetal water to produce pure olive oil.

- **Pomace:** The solid impurities that result from the squeezing of the olive paste are called pomace. Pomace is used as heating fuel and also as manure in agriculture.

- **Filtration**: After washing and mixing the olives, the mix is ready for the separation process to separate the oil from other solids. The separation consists of two stages. The first is the separation of solids from liquids, The second is to separate oil from other liquids.

- **Refinery:** The fluids resulted from squeezing of the olive paste are filtered to separate oil from vegetal water. The vegetal and washing water are recycled to be used again. The washing water contains a small amount of the solid impurities resulted from filtering the oil. These impurities are considered a manure for agriculture and thus making the washing water a good choice to be used as irrigation water.

3. Stages of olive squeezer

- **Squeezer process:** The squeezer process performs many operations and in every stage which means that olive passes through different operations before producing oil, the operation will be divided into four stages such as startup stage, washing stage, mixing stage, filtering stage.

  Figure (1) shows the four stages of the manually controlled olive squeezer process. Each stage will be discussed in details.
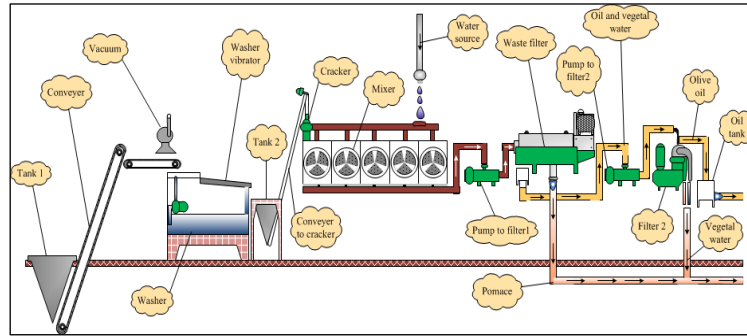
Figure خطأ! لا يوجد نص من النمط المعين في المستند. :The olive squeezer process.

- **Startup Stage:** At the beginning, it is necessary to maintain an appropriate water temperature to allow the squeezer to work in the range between 70 $^{\circ}$C to 80 $^{\circ}$C and it is also necessary to fill the tank with an appropriate amount of water to allow the washing process of the olive, therefore, the level inside the tank has to be specified.

- **Washing olive stage:** When the olive is poured inside a storage tank, the conveyer belt was powered on by the operator using a switch. This will transfer the olive from the storage tank to the washer tank. Olive passes through the vacuum that sucks the tree leaves and rods. Then the operator will switch on washer to wash and clean the olive.

  The washer pumps olive to the vibrator, and at the same moment the washer vibrator will be powered on, the vibrator will vibrate olive to dry it and then will transfer it to tank 2. The washing is shown in figure 3.
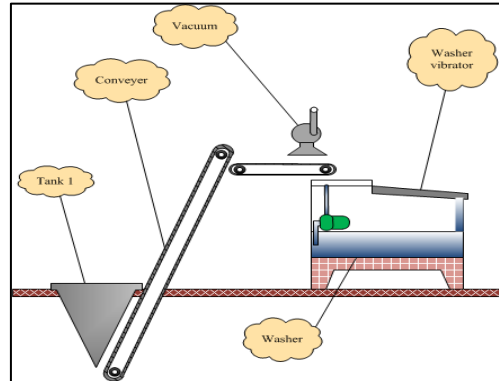
Figure 3: Washing Stage.

- **Mixing Stage:** When olive reaches tank 2, the operator will switch on the cracker and wait until rotational speed reaches the required value, which is in the range from 4100 rev/min to 4200 rev/ min. When the required speed was reached, an indication lamp is lit on. After that, the operator will switch on the conveyer. This conveyer transfers olive from tank 2 to cracker, where the olive will be cracked before passing to the next stage. After cracking olive, the operator will power on the mixer. That will mix the cracked olive until it's ready to transfer to the squeezer process as shown in figure 4.

Figure 4: mixing stage.

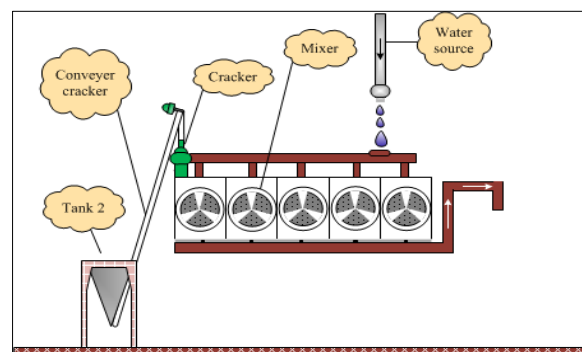- **Filtration Stage**: After the mixing, it will enter new stage, called filter stage. In this stage, the mix will pass through another wringer to separate oil and water from other impurities, the filter stage is divided into two parts as follow:

4. Liquid separation from other defects:

There is a pump that pumps the mixing olive to wringer, then the operator will power on the wringer to separate oil and water from other impurities.

- **Oil separation from water:** The operator powers on the filter and waits until it reaches the required velocity which equals to 3500 rev/min. There is a lamp to indicate if the filter reaches that required velocity. Then the operator will switch on the pump to send the oil to the filter. This filter will separate oil from other liquids. The figure 5 shows the filtration stage.
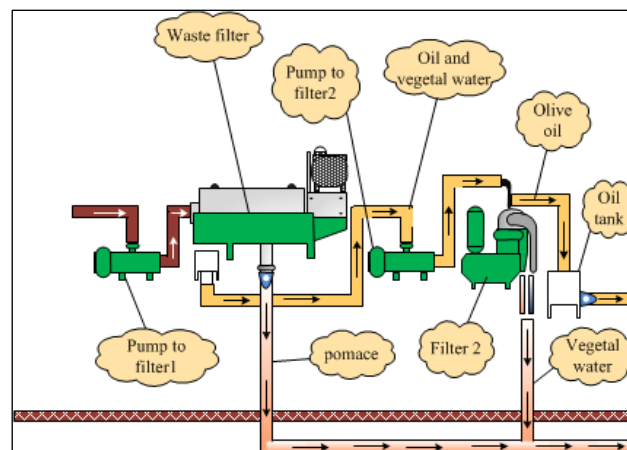
-

Figure 5: filtration stage.

- **Wrapping-up:** The process was fully manual, where operators had to move between different machines which

affects the work process and reduces productivity and increases the risk. And thus a solution must be proposed to solve this problem by adding modern technologies that can improve olive oil extraction. The addition of such technologies should make the process autonomous that allows the operator to easily control and monitor the process from a centralized location, and it can also help during error and fault identification.

- **Control Strategy definition:** This stage involves the definition of processing steps sequence that will lead to the desired output. The processing steps sequence is known as Instructions. The process of control design for systems controlled with PLCs needed the development of specific instructions to help in programing later.

  The instructions are implemented based on the goal required from the control process. Alternative approaches should be considered as a way to problem solving. The instructions of the process are:

```
-  START
-  Raw material (Olives) IN
-  Washing Water IN
-  START Washing
-  IF Washing is completed:
   o  START cracking stage
   o  Recycle washing water IF Water NOT clean
-  START separation stage, Olive Pomace OUT
-  IF separation is completed:
   o  START filtering stage, vegetal water OUT
-  Olive oil OUT
-  END
```

- **Flowchart:** Flowchart is a graphical representation of programming sequences involved in control process design. Flowcharts can be also called an algorithm.
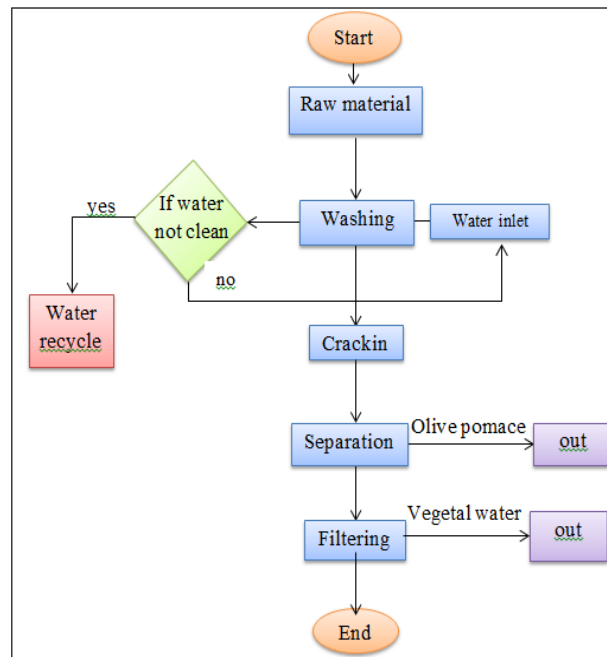

Figure 6: flow chart of process programing

5. Squeezer manufactory process

As mentioned earlier, the squeezer performs many operations on the olive before producing olive oil. Previously, it has been explained that the squeezer works manually; this method depends on labor to pass between stages of operations. Figure 7 shows the fully developed squeezer machine using PLCs.

Figure7: Development of olive squeezer system.

Now, the automatic operation of the squeezer will be discussed, and what modifications are needed to achieve that, and a set of sensors and limit switches will be coupled with some appropriate components to reach the required goal. Each stage will be discussed in details.

- **Stage of startup:** For the mixer to work, it is necessary to set its temperature between 70 $^\circ$C to 80°C, a thermistor will be added to achieve the required temperature range. The thermistor reads the temperature from a thermocouple and gives an output based on the temperature range. The operating temperature range to be programmed with the thermistor, as mentioned earlier.

  A level sensor was inserted inside the washer tank to monitor the water level required of the washing operation.

  There is another method which applying Predictive controller for olive oil squeezer applications to control the temperature of paste and flow of water used in mixing stage.[26]

Figure 8: program for startup.

Table 1: address assignment for startup.

Element	Function of element	Address
Start up switch	To start operating	X27
Heat sensor	On if temperature high	X22
heat sensor	Off if temperature low	X23
Level sensor lower in washer	On if level low	X5
Heating mixer	To heat the water for mixer.	Y21
Washer water	To pumping water to washer.	Y17

- **Olive Washing Stage:** At the moment of inserting olive in the tank, the operator will transfer the olive from the tank to the washer by conveyer belt. A Limit Switch was inserted behind this tank to monitor the presence of olive. The output of the limit switch is indicating to the presence of the olive, i. e. if there is olive in the tank, the limit switch will be ON and vice versa. This process simplifies the operation of the conveyer belt which transfers the olive to the washer and to automate the vacuum which separates the tree leaves and rods from the olive. A photo switch was fitted between the conveyer belt and the tank of washer to turn off the conveyer and the vacuum. Once the vacuum starts to work, the washer starts too as a sequence operation. And when the washer works, the vibrator also works which vibrates the olive to drain it from water.

Another photo switch is inserted beside washer to sense if there is olive still on vibrator or not. The washing stage is illustrated in figure 9.
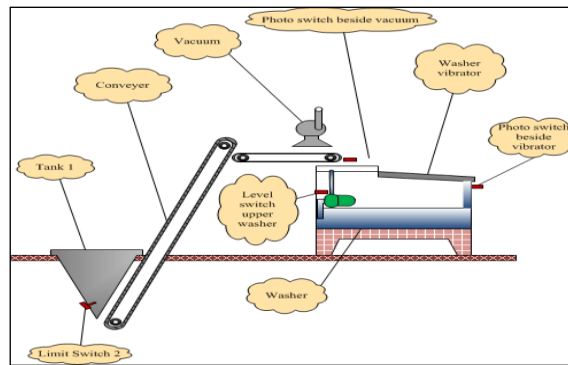

Figure 9: Washing Stage.

Table 2: address assignment of washing stage.

	Element	Function of element	Address
1.	Conveyor.	To transport olives to the washer.	Y0
2.	Vacuum.	To rack rods and leaves.	Y1
3.	Washer.	To clean olives.	Y2
4.	Vibrator.	To dry olives.	Y3
5.	Limit Switch 2.	On if olives in tank1.	X0
6.	Level switch upper washer.	On if water in washer is low.	X5

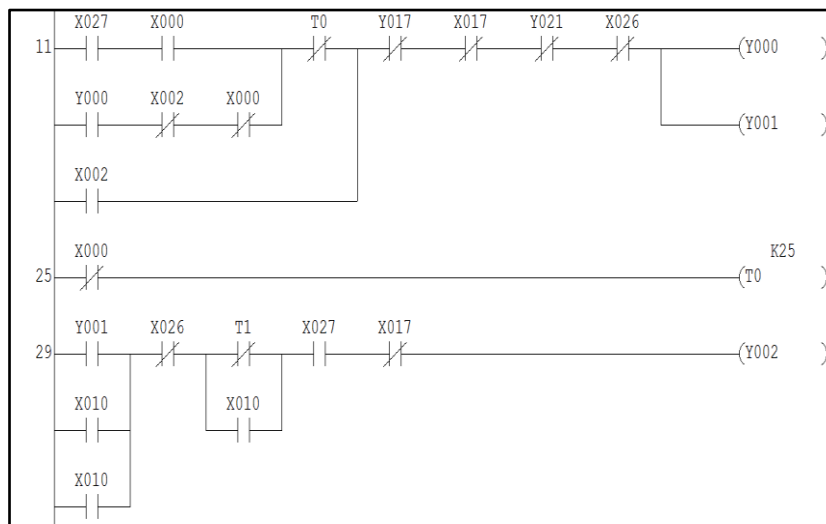| 7.	Photo switch beside vacuum.	On if there is olive bring down from vacuum.	X2
8.	Photo switch beside vibrator.	On if there is olives bring down from vibrator.	X10

Figure 10: program for washing stage.

- **Mixing Stage:** A Lower Limit Switch is added inside tank 2 between washer and conveyer cracker to ensure if there is olive in the tank or not. If there is olive in the tank, the state of limit switch will be on, and if there is no olive, the state of the Limit Switch stays off. There is another upper Limit Switch in tank 2 that indicates if the tank is full, and thus it will turn off the conveyer belt1 to avoid overloading of tank2. Moreover, we placed a photo switch upper the conveyer cracker to guarantee that the olive transfers from tank 2 to the cracker by

the conveyer. If the state of this photo switch is on, this means that the olives are transferring to the cracker, otherwise the state of this photo switch stays off. In addition, to know if there is olive shattered in the mixer, another lower limit switch is inserted inside the mixer. This switch will sense if there is still shattered olive in the mixer. Also, another upper limit switch is added inside the mixer to give an indication if the mixer is full or not.   A concentration sensor was added to measure the concentration of olive pasta in the mixer. If the mix becomes dry, the rotational speed of the motor drops below the required value, and thus water is added to the mixer through a valve connected to water pipe that controls the required amount of water to be added. When the mixing process finishes, the mix is transferred to the filter by the pump. The mixing process is illustrated in the following figure 11.
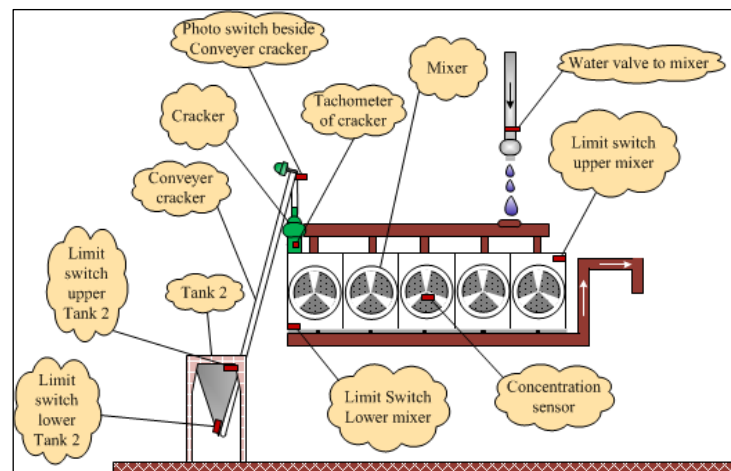

Figure 11: mixing stage.

Table 3: address assignment of mixing stage.

|	Element	Function of element	Address
1.	Conveyor Cracker	To transfer olives to cracker.	Y20
2.	Cracker	To crack olives.	Y3
3.	Mixer	To mix olives.	Y4
4.	Water Valve to mixer	To add water to the mixer.	Y5
5.	Pump mix to wringer	To pump olive paste to the wringer.	Y6
6.	Limit Switch lower tank2.	On if olives in tank2.	X20
7.	Limit Switch upper tank2.	On if tank2 is full.	X17
8.	Limit Switch lower mixer.	On if olives in mixer.	X4
9.	Limit Switch upper mixer.	On if mixer is full.	X6
10.	Concentration sensor.	Measure the concentration in the mixer.	X3
11.	Tachometer of cracker	To the measure speed of cracker motor.	X7
12.	Photo switch of the cracker.	On if there is olive bring down from conveyer cracker.	X25
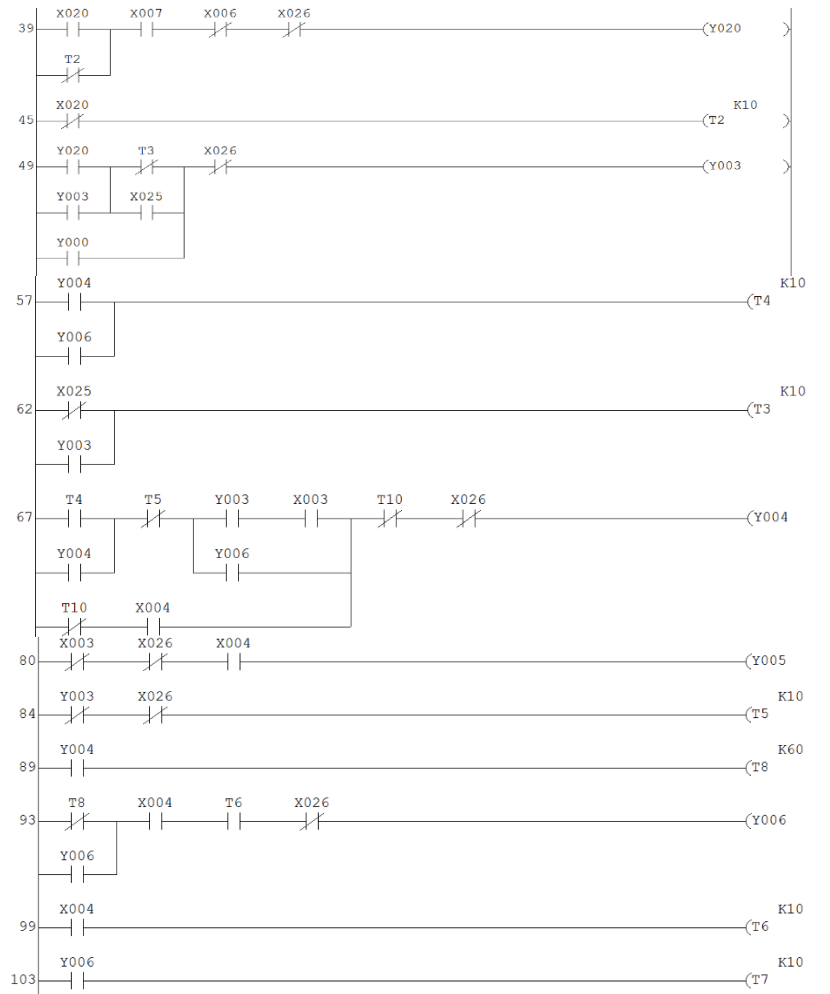
Figure 12: Program for mixing.

- Filtration Stage: An oil flow switch was added to start the wringer that extracts oil and water from mix. The waste is called pomace olive.

  Another oil flow switch was added to start filter 2 that separate oil from water. The extracted oil is transferred to the oil tank through a pump that starts by a level switch attached to the lower part of the tank.

  Finally, a second level switch was included oil to the upper part of the oil tank to prevent oil from overloading from the tank, by stopping the pump. The filtering process is illustrated in figure 13.
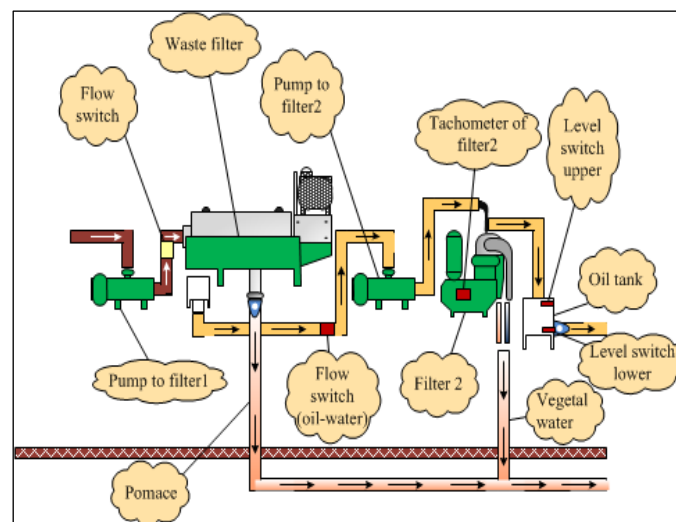

Figure: 13 filtering stage.

Table 1: address assignment of filtration stage.

|	**Element**	**Function of element**	**Address**
1.	Wringer (pomace)	To separate pomace.	Y7
2.	Vibrator oil-water	To remove oil from water.	Y7
3.	Pump to filter 2	To pump the mix to filter 2.	Y10
4.	Filter 2	To separate oil from water.	Y15
5.	Flow switch.	On if the mix is coming to waste filter.	X16
6.	Flow switch (oil-water)	On if the oil and water coming to filter 2.	X15
7.	Level switch lower	On if the clean oil in final tank.	X14
8.	Level switch upper.	On if final tank is full.	X12
9.	Tachometer of filter 2	To measure filter 2 rotation speed	X13
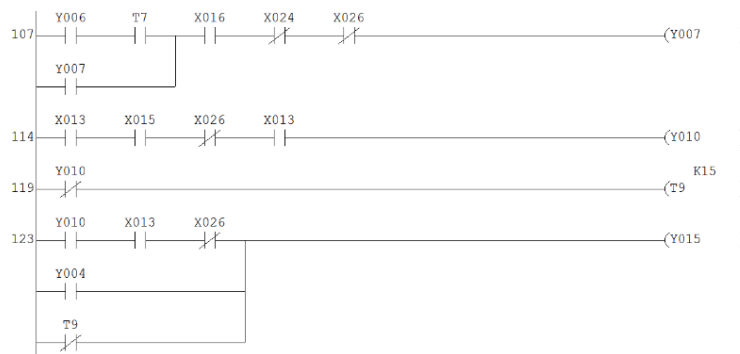
Figure 14: program of filtration stage.

- **Water Recycling Stage:** Another important stage has to be added was the water recycling stage. It was used to filter the water that is used to wash the olive.

  This process will be carried out by taking one sample from washer every 20 minutes. And test this sample by using capacitive sensor (Purity Sensor), this kind of sensor measures the cleanness of water in the washer. If state of the sensor is off, it indicates that the water is clean and thus open the "Valve Return" and close the "Valve to Filtration", and vice versa. When the "Valve to Filtration" is open, the water will flow down to the sieve. The imperfections (stones and rods) will be captured by the fence while the water will pass through.

  The fence was placed in a tilted position to allow the stones and rods to fall off the fence to allow more room for the sieve to catch more imperfections and not block the water from flowing through the fence as shown in the figure 4.9. Then, the pump will push the water to the filtering machine to be filtered. The recycled water will be sent back to the storage water to be used again.
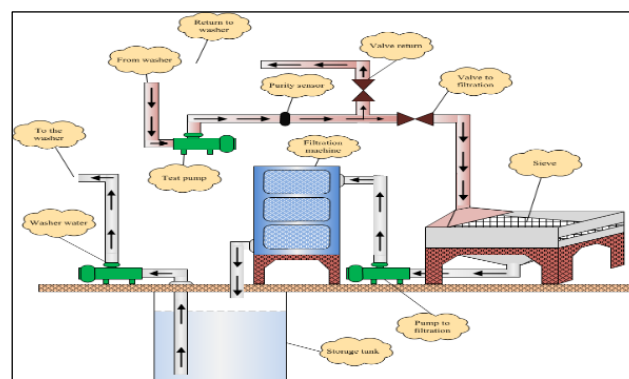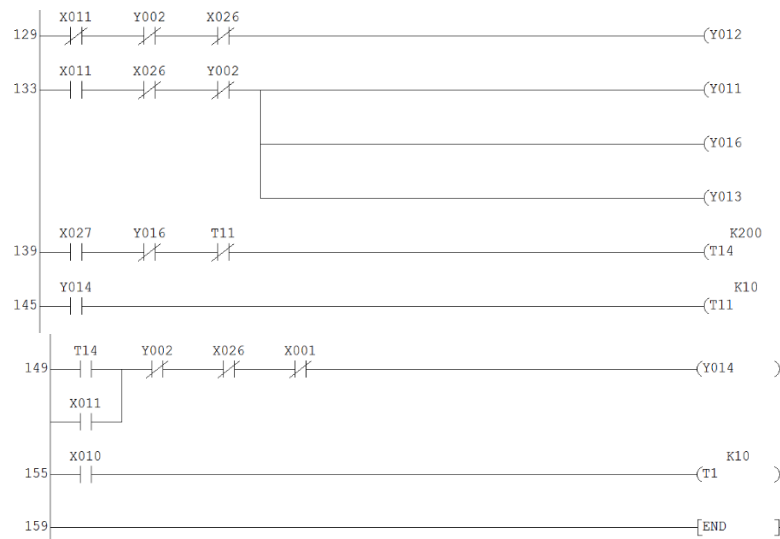

Figure 15: Water Recycling Stage.

Table 2: address assignment of water recycling.

	Element	Function of element	Address
1.	Return Valve.	To pass sample to the washer.	Y12
2.	Filtration valve.	To pass sample to filtration machine.	Y11
3.	Filtration machine.	To filter the water.	Y16
4.	Filtration pump.	To pump water to filtration machine.	Y13
5.	Test pump	To take water sample.	Y14
6.	Purity sensor.	On if water in washer is impure.	X11

Figure 16: program of water recycling.

6. Components used in this project

The components that are used in this project are:

- **photo switch:** are used to determine whether an object is present or not. Photo sensors are transmissive types where the object being detected breaks a beam of light, usually infrared radiation, and stops it reaching the detector. [22]. The photo switch is illustrated in figure 17.
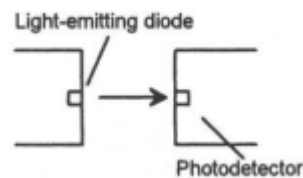
Figure 17: photo switch.

- **Level switch:** it measures the level of liquids and consists of a horizontal arm that is free to swing according to the liquid level. When the liquid reaches the required level, the arm gets lifted up which affects the state of the Reed Switch that is attached on the arm and thus changing the state of the sensor to ON. The level switch is illustrated in figure 18.
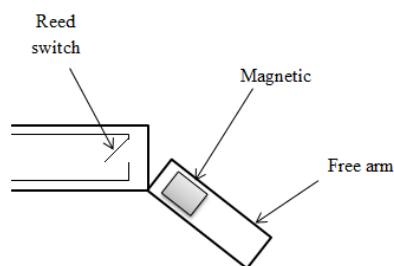
Figure 18: level switch.

- **Tachometer:** it is a device to measure rotational speeds of cracker and filter 2, and are installed in a specific position. When either of these devices starts rotating, the tachometer produces a voltage that is proportional to the rotational speed. The voltage that is produced at the required rotational speed is recorded to be used on an op-amp circuit. The op-amp circuit will compare between the input voltage from the tachometer with the voltage value consistent with the required rotational speed. If they match, the op-amp results a zero-voltage output. The output of the op-amp is connected to an inverter so that when the rotational speed reaches the required speed, the output from the inverter gives output of 1 which can be connected to a PLC to allow it to stop the cracker or filter 2 when the required rotational speeds are reached. As illustrated in figure 19.
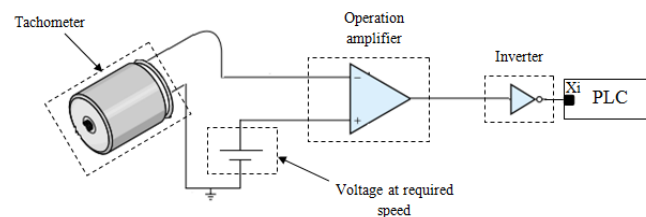
Figure 19: The cuircut between tachometer and PLC

- **Concentration sensor:** it is used to measure the softness of the mix. Sensor sends ultrasonic signals through the mix and receives the reflected signals. The nature of the reflected signals changes as the concentration of the mix changes. The signals that result from a perfectly concentrated mix is used a set point to test other concentrations. The set point will be compared with other signals from different concentrations using op-amp that results a zero output when the required concentration is reached, which is connected to an inverter that

gives output of 1. The ultrasonic Sensor is illustrated in figure 20.
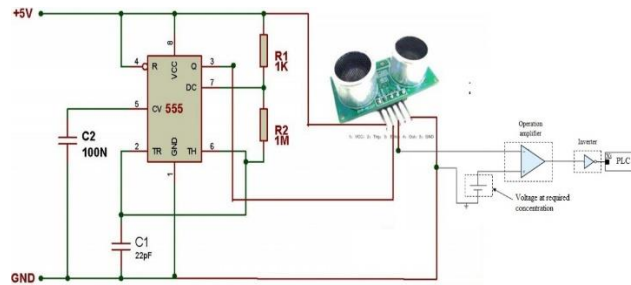
Figure 20: ultrasonic sensor

- **Solenoid valve:** it is used to open and close liquid channels. It is used to control the amount of water that is added to the mix to soften it. It consists of a barrier that is actuated by a coil. The barrier blocks the flow of liquids when the valve is not energized. When the valve is energized, the coil generates an electric field that pulls the barrier out allowing liquids to flow [22]. The solenoid valve is illustrated in figure 21.
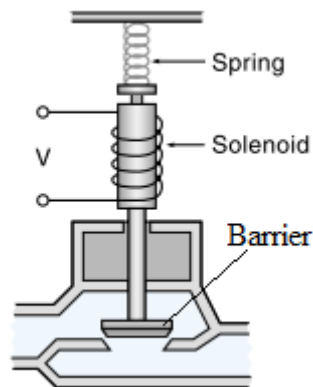
Figure 21: Solenoid Valve

- **Flow switch:** it senses the presence of liquid flow inside a pipe. It's a capacitive proximity sensor that has an oscillating electric field, sensitive to all materials. It consists of a retractable arm that is placed inside the pipe. When a liquid flows through the pipe, it pushes the arm out of its way which affects the oscillating electric field and thus changing the value of the sensor to ON. The flow switch is illustrated in figure 22.

Figure 22: flow switch

- **Limit switch:** it's a mechanical device that uses physical contact to detect the presence of an objects. A typical Limit Switch consists of a switch body and an operating head. The switch body includes electrical contacts to energized and de energized a circuit. The limit switch is illustrated in figure 23.
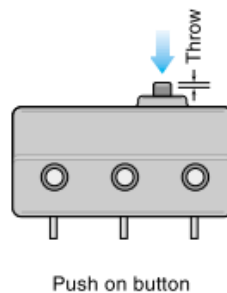
Figure 23: limit switch.

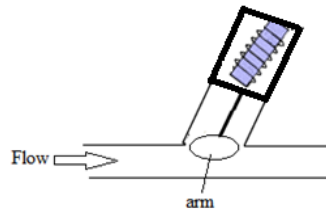- **Purity sensor:** it consists of a laser source and voltaic cell. Laser source sends laser to voltaic cell that transforms the beam to an electrical signal. When water passes through the purity sensor, the latter gives a certain voltage value based on water purity. As shown in figure 24.
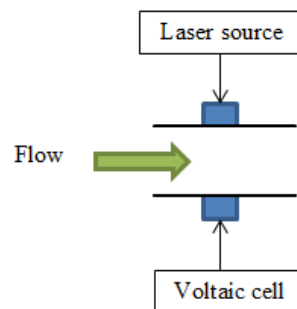
Figure 24: Purity Sensor

The voltage corresponding to the lowest water purity is recorded and used as set point on an op-amp circuit. The op-amp circuit will compare the input voltage from the sensor with the voltage value consistent with the required impurity of water. If they match, the op-amp results a zero-voltage output. The output of the op-amp is connected to an inverter so that when the water impurity reaches the required value, the output from the inverter gives output of 1 which can be connected to a PLC. As shown in figure 25.
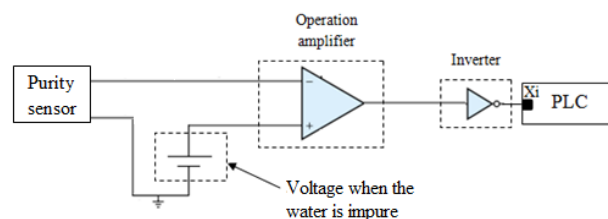
Figure 25: The circuit between purity sensor and PLC

- **Thermocouple:** since the thermocouple output is very small (mv), the output voltage is amplified using an op-amp circuit. The output voltages corresponding to temperatures of 70°C and 80°C are recorded as V1 and V2 respectively and used as set points. The output voltage from the op-amp will be compared with these two set points using two op-amp circuits, if the temperature is less than 70°C, the output from the first differential amplifier will be less than V1 and therefore comparator 1 will result an output of 1. And if the temperature is greater than 80°C, the output from the first differential amplifier will be greater than V2 and therefore comparator 2 will result an output of 1. The output pins of both comparators are connected to PLC. As shown in figure 26.
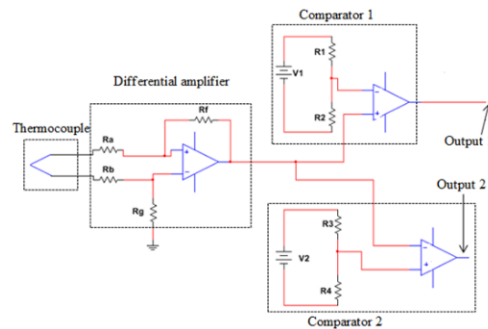
Figure 26: Temperature Switch

- **Model Fabrication**

  This model simulates the process of olive squeezer using hardware connection to each component. This model fabrication was done in order to ease the understanding of the process for users and to clarify all operation stages of the process.

This model was established to perform two main functions; the first function is to clearly demonstrate the squeezing process step by step according to the proposed of PLC software, and secondly, to use such model in real time as monitoring and control unit which gives the operator good observation for the whole process.

- **Optionality**

There are many simulation processes that can give a real time view of industrial processes like LabVIEW and WinCC. These applications take input signals and generate corresponding output signals, input signals are signals generated by sensors, limit switches and tachometers. And based on these sensors and the PLC program, an output signal is generated.

This model is designed to simulate the work principle of olive squeezer process and it consists of many input and output terminals. Input terminals for the olive squeezer process consist of sensors and tachometers that are replaced by a set of switches that simulate their functions. There are also a set of limit switches that are used to initiate the process and act if it's necessary to. There are a variety of output terminals including conveyors that run using motors. Other output terminals include washers, vacuums, mixers, valves and a set of pumps. These output terminals are replaced by indicators or lamps. Each indicator is used as a sign for one output terminal and it's placed directly behind its corresponding output terminal. The state of each output terminal (either ON or OFF) is presented by the lamp indicator that is simulating the corresponding real actuator.

- **The proposed model:** The system operation starts only if the Start switch is ON. The process starts by heating the required amount of water to a certain degree which ranges from 70°C to

80°C, and simultaneously the pump starts filling the washer with the required amount of warm water. The internal thermistor that is required to sense the water temperature is replaced by a switch in this model which can be activated manually. The switch status remains ON as long as the required temperature hasn't been reached, and then it changes to OFF indicating that the required temperature has been reached. These signals are sent to PLC which are the status of the heater ON and OFF according to water temperature.

The level sensor that is used to indicate the water level is replaced by a contact in this model. When the water reached desired level, the status of the contact is changed to ON indicting that desired water level has been reached and the PLC switch OFF the pump of the washer. The squeezer starts operation only when desired water level and temperature have been reached. Figure 27 shows the model fabrication of the system.
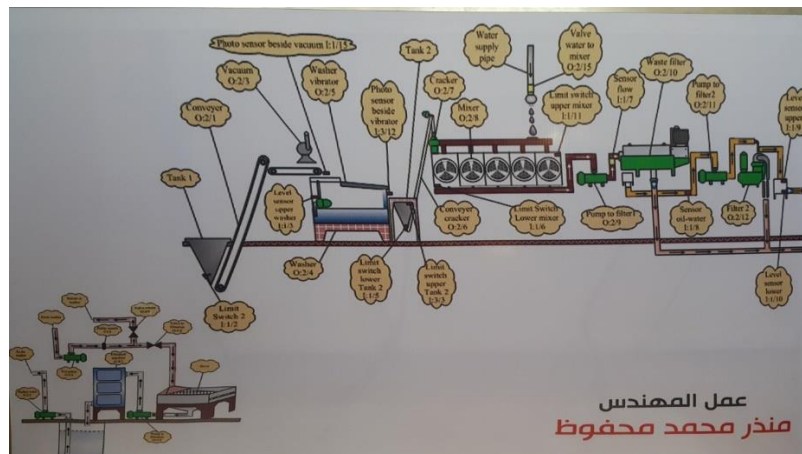
Figure 27: Model Fabricition.

- **Olive washing stage**: As stated earlier, there is a lower limit switch inside the tank1 that indicates the presence of olive inside it. In this model, the lower limit switch is replaced by a contact which is set ON to simulate the presence of olive inside the tank. The signal from this contact will trigger the conveyor that starts working and carry's olive to the vacuum machine. A photo-sensor was to be used along the conveyor to indicate the flow of olives on the conveyor. This photo-sensor was replaced by a contact in this model to simulate the state of the sensor either ON or OFF. The washer, vacuum and the washer vibrator are turn on alongside the conveyor.

  Another photo-sensor was to be placed on the washer vibrator, which has been replaced by a contact in this model. The contact is used to indicate the states of this photo-sensor. The status ON indicates that the olives are passing from the washer vibrator to the second tank and status OFF indicates the opposite case. Figure 28 shows the washing stage of the model fabrication.
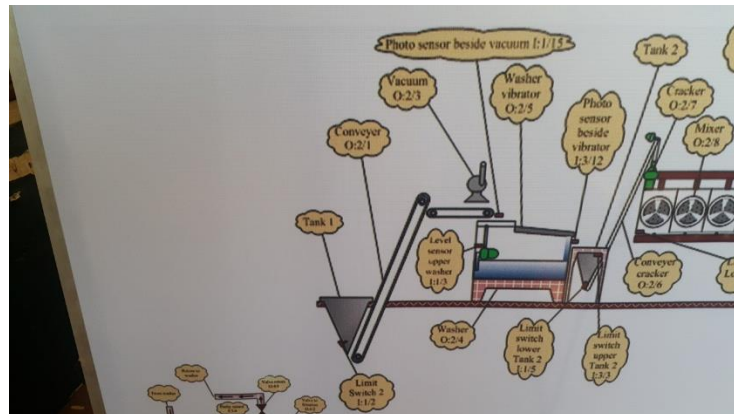
Figure 28: Washing Stage.

- **Mixing stage:** The 2nd stage starts when olive reaches the 2nd tank. When the olives reach the second tank, it triggers the limit switch at the bottom of the tank. Another limit switch was placed at the top of the second tank to indicate when the tank becomes full and in which case the conveyor of washing system is stopped. Then cracker conveyor doesn't start operating until the cracker motor reaches the required rotational speed of 2400 rpm. The cracker rotational speed is measured using a tachometer which is been represented by a contact in this model. The state of the contact is ON when the cracker reaches the required speed, otherwise the state is OFF. When the required rotational speed of the cracker is achieved, the cracker conveyor carries the olives to the cracker.

  After the olives have been cracked, the olives paste was passed to the mixer. The olives paste presence in the mixer is sensed by the limit switch placed inside the mixer. A concentration sensor is also placed inside the mixer to check whether the right concentration is met or not. The concentration sensor was replaced by a contact, if the right concentration is met, the state of the contact goes ON, otherwise, it goes OFF. A limit switch is place at the top of the mixer to indicate if the content of the mixer reaches over flooding. When that happens, the cracker conveyor stops its operation. Figure 29 shows the mixing stage of the model fabrication.
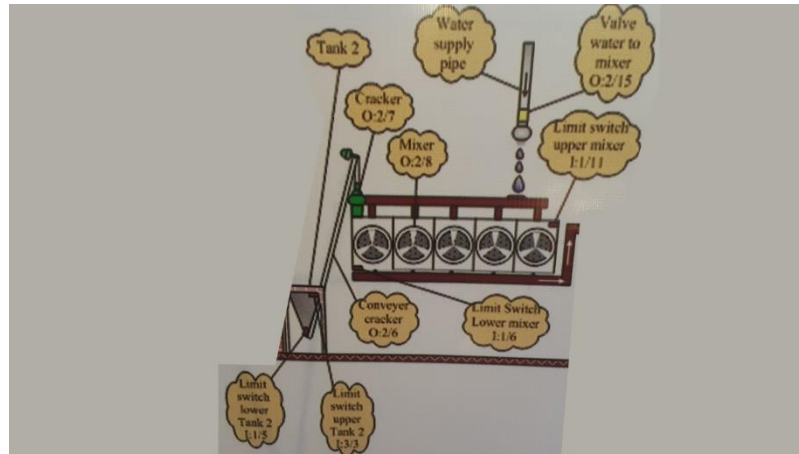
Figure 29: Mixing Stage.

- **Filtering stage:** The mix of olives paste was passed to Filter 1 through the pump 1. A flow switch was placed at the outlet of the pump to measure the flow rate. In this model, the flow switch was replaced by the contact that is used to indicate the state of the flow switch. If the mix is flowing near the switch, the switch state is set to ON, otherwise it's set to OFF. Mixer 1 separates the solid objects from the mixer, and each goes through different channel. Another flow sensor is placed in the liquid mix channel, to sense of the mix is flowing or not. This sensor is replaced by a switch to represent its state. When the state of this sensor goes ON, Filter 2 is started before also starting the second pump that will push the liquid mix to Filter 2. Before producing the desired results, Filter 2 has to reach 3500 rpm, which is monitored through a tachometer placed inside the filter. This tachometer is replaced by a switch that is used to indicate whether the required rotational speed is reached or not. When the required rotational speed is achieved, the pump pushes the liquid mix to Filter 2. The required rotational speed is the speed that separates the oil from other

liquids. The oil is stored in another tank and the waste gets discarded. Figure 30 shows the filtration stage of the model fabrication.
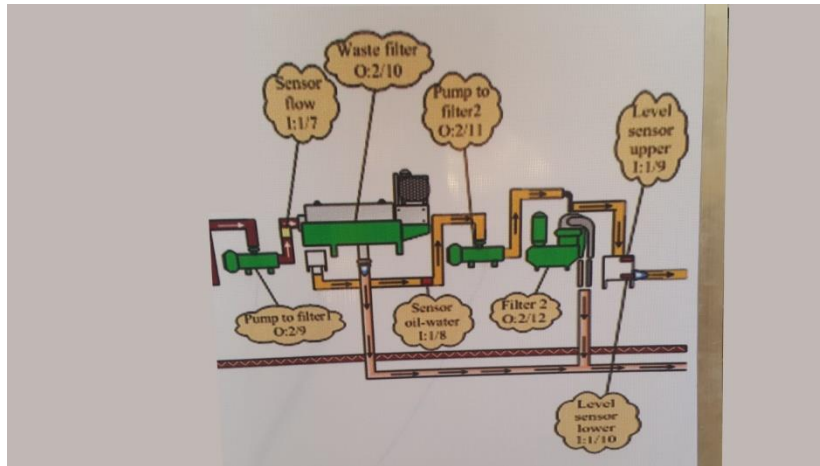
Figure 30: Filtering Stage.

Water recycling stage: A purity sensor is used to test a sample from the water that was used during the washing stage, the sensor checks if the water can be reused again or not. This sensor is replaced by a contact to indicate its state. The state ON if the water is clean to be used again or state OFF if it needs to be refined and recycled through water storage tank again. Figure 31 shows the water recycling stage of the model.
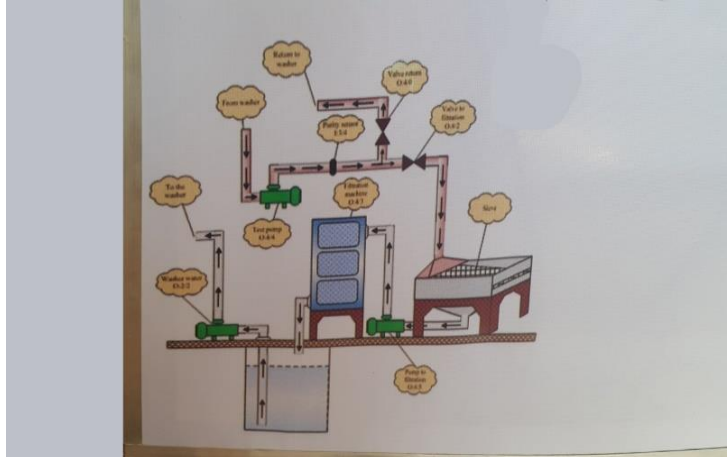
Figure 31: Water Recycling Stage.

Connections in Real Time:

As stated earlier, the PLC reads input signals from input devices which are; sensors, limit switches and tachometers. The PLC then executes the stored program and gives output signals to the actuators (e.g. motor, pumps, etc). These input devices were replaced with contacts and their connection setup will be discussed in this part.

- **PLC Input Connection:**

In order for the switch to function, the switch has to be connected to a power source to draw enough power. The PLC that is used with this model is equipped with build-in terminal that provide enough power. One terminal of each switch is connected to the power source pin on the PLC while other terminal is connected to its corresponding signal input pin on the PLC. When the switch is activated (pressed) the two terminals of the switch gets connected together causing its corresponding input pin to be turned ON.

- **PLC Output Connection:**

  The output devices need an activation signal to be turned on. The activation signals can be sent to output devices from the output pins on the PLC. Each set of output terminals can be activated using certain pin corresponding to them. For example; y0, y1, y2 and y3 are activated using V0 pin. The same concept applies to other set of output pins. To activate or turn a lamp ON, one of its terminals is connected to the 24V pin while the other is connected to its corresponding signal output pin (y0, y1, …..). If another type of output device is to be connected to the PLC, like motors or actuators, an interface is needed as they require more power than the PLC can deliver. There are various types of interfaces that can be used, for example; relays. Relay can be interfaced with PLC by connecting the output terminal from the PLC to one terminal of the relay coil while the other terminal is connected to ground. The contact of the relay is connected in series with the actuator and power source that can handle actuators. When the relay coil was energized, then the contact goes ON and connects the power source with the actuator.

  This model can be connected to a real squeezer (Um Alraml squeezer) in order to monitor the system, and it's done by connecting switches to the real system which now simulate only the functions of real components such as switches and actuators.

  One advantage of the developed system is that it allows the monitoring and control of the system from one computer station and no need to relocate between different places.

  As stated earlier, the model can be used to monitor and control the real squeezer system which only requires few sensors and interface between the model and the real components.
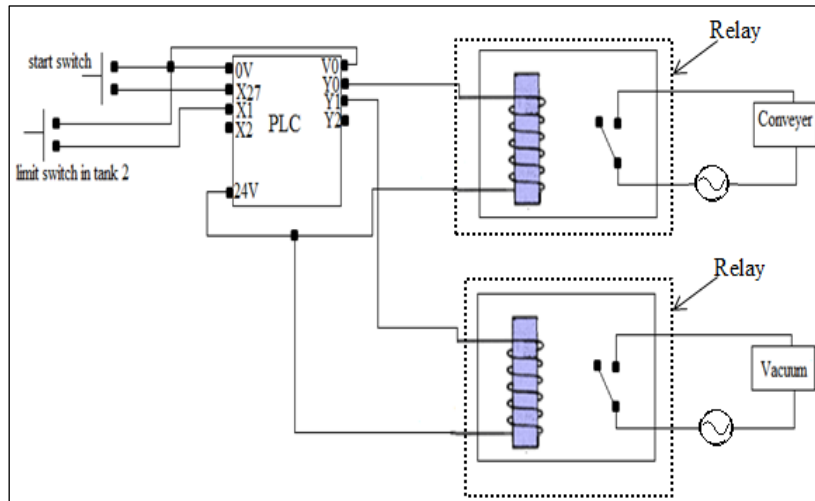
Figure 32: real connections of PLC and I/O devices

7. Conclusion

When adding various components as monitoring components such as sensors, limit switches and tachometers, the efficiency is increased and errors are reduces, and it can also save energy and time. Components are turned ON or OFF only when needed. The addition of sensors increased monitoring efficiency and helped in achieving fully automated control system for the squeezer.

In manual control of squeezers of olive oil, the human is essential part of the control, this costs time and effort. To overcome this problem, the system was modified to automatic control system by using PLC controller and ladder programing to simulate the squeezer operation with full automatic steps.

The control system which was designed by using PLC handled many problems in manual control. The PLC system was able to decrease the errors of human operators and increase the component efficiency and then the productivity. The proposed solution can be implemented in real time operation and expecting the same results as in the simulation.

The model was fabricated to show the work steps of the squeezer. This model can be used as GUI graphical unit interface to monitor the real system and identify for any errors or faults in the squeezer from a centralized station. The model gives an easy-to-understand UI (User Interface) that helps newly recruited operators.

The model helped in reducing risk and saved time and effort for the operators by showing an overall diagram of the whole squeezer system allowing the operator to monitor all stages from one place without the need to visit them one by one.

References

[1]   Feedback Control System, John Van De Vegta, Prentice Hall, 1990.

[2]   Automatic Control Systems, B. Kuo, Prentice Hall.

[3]   Bateson, R. N. Introduction to Control Systems Technology, Prentice Hall, 2002.

[4]   Programmable Logic Controllers, J. W. Wabb and R. A. Reis,1994.

[5]   Programmable Logic Controllers, C.Simpson, 1993.

[6]   Programmable Logic Controllers and their Engineering Applicatios, A. Crispin, 1990.

[7]   The PLC workbook, Clement Jewery,1993.

[8]   Programmable Logic Controls (PLC I, II, III) By K. Haase. May 1992.

[9]   https://sites.google.com/site/mervatdaa/12.

[10]   https://Moaar.gov.sy/mog.

[11]   https://rapanelli.it/inglese/quadro_temperature.htm

[12]   History of automatic control ,http://www.springer.com/978-3-540-78830-0.

[13]   L.A. Bryan and E.A. Bryan , Programmable Controllers Theory and Implementation , Second Edition , Printed and bound in the United States of America prentice 1997.

[14]   Series 90™-30/20/Micro PLC CPU Instruction Set Reference Manual– May 2002

[15]   D. Morley, looks back on the 40th anniversary of the PLC Manufacturing Automation, 12 September, 2008.

[16   ]W. Bolton, Programmable Logic Controllers, Fifth Edition, Newnes, 2009.

[17]   Vishal Kumar Alok , Ajay Goel: To study the different industrial   applications of PLC through ladder diagrams ,prentice May, 2011.

[18]   Bateson, R. N. Introduction to Control Systems Technology, Prentice Hall, 2002.

[19]   E. A. Parr, Industrial Control Handbook, Industrial Press Inc., 1999.

[20]   Webb, J.W., Reis, R.A., "Programmable Logic Controllers, Principles And Applications", Prentice Hall, 1995.

[21]   John T.Bandy etal. Use of Programmable Logic Controllers To Automate Control and Monitoring of U.S. Army Wastewater Treatment Systems, USACERL Technical Report N-91/27 July 1991.

[22]   M. A. Adamski, J. L. Monteiro, "PLC Implementation of Logic Controllers", IEEE International Symposium on Industrial Electronics (ISIE 1995), 1995, pp. 706-711.

[23]   Jacob Fraden, Handbook of modern sensors : physics, designs, and applications, Springer 1996.

[24]   José, G.M. and K., Yousfi. The post harvest of mill olives. Grasas y Aceites, 57 (1), 16-24, 2006.

[25]   Carlos Bordons and Manuel L. Zafra. Inferential sensor for the olive oil industry,2001.

[26]   C. Bordons*, J.R. Cueli. Predictive controller with estimation of measurable disturbances, November 2002.

[27]   El-Sayed etal. "Hazard Analysis Critical Control Points (HACCP) Application during Olive oil centrifugal extraction" Desert Research Centre, Cairo, Egypt. (Jan. 2015).

Control of A Simple Micro-Mouse Robot Equipped With Stepper Motor and Bluetooth Technology

.

10

Control of A Simple Micro-Mouse Robot Equipped With Stepper Motor and Bluetooth Technology

Saad Eshtewi
High Institute of Science and Technology - Messallata
seshtewi129@gmail.com

Abdelhadi H. Aburwess
High Institute of Science and Technology - Messallata
Aaborwess522@gmail.com

Abstract

In today's world, many challenges have been encountered in the process of designing robotics. These challenges have increasingly become more and more complex; such as materials used, control and efficiency of performance. This study focuses on the initial development to design and build an Arduino based Micro-muse that can be controlled via Bluetooth and required sensors. The Micro-muse is able to move in different directions such as forward, backward, left, and right. In addition to this, the movement can be controlled by using a bluetooth-enabled device such as a smart phone or tablet. The system adapted here utilizes various electronic components such as sensors, motors, motor drivers and Bluetooth modules. This design also includes encoding the Arduino board using the Arduino Integrated Development Environment (IDE) as well as writing the code using the C++ programming part. This study also aims to provide a hands-on learning experience for student, researchers and enthusiasts interested in robotics and electronics.

Keywords: Integrated Development Environment (IDE) – Micro-Mouse – Bluetooth – Arduino – C++ Programming.

1. Introduction

Currently, the complexity of designing robotics has a rapid increase and has become difficult to control due to the growing tasks in the field of engineering, which lead to the high necessity of designing an ideal method for robotic control [1]. The research especially concentrates on the navigation of the micro-mouse through its path. This micro-mouse is required to move safely through the path in its design-environments, wherein it would complete its goal with the expectation of some obstacles that might appear.

The rest of this paper is organized as follows: the system model is presented in section 2. After that, a performance analysis is demonstrated in section 3. Finally, conclusions are made in7.

2. System Model

Essentially, to test validity of the design of our micro-mouse and make sure that is well-designed, it is important to cover all aspects of design to obtain the desired results. For instance; wheels, chassis, stepper motors, batteries and sensors will be designed through the following steps as illustrated in schematic of Figure 1.
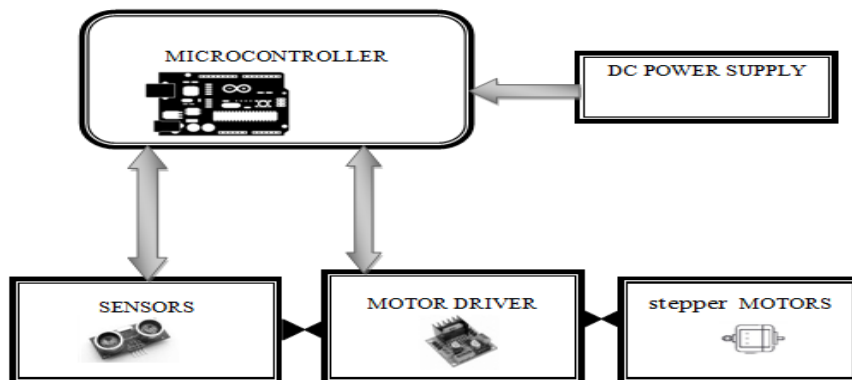
Figure 1: Block Diagram

The system shown above consists of stepper motors which are used to move the wheels in different directions. The differential drive degree has two independent motors in fixed positions (left and right) which also controls the speed. Arduino programs are used for driving stepper motors because of its ability to control the discrete movements of steppers and its ease and simplicity of programming to work with steppers of different types [2-3]. Sensors would also be needed in the robots' path, so Ultrasonic or Infrared sensor could be used in the system to take action to avoid barriers. For this, sensors and motors can be controlled wirelessly using Bluetooth, Wi-Fi, or other wireless [3]. A microcontroller board such as an Arduino was the best option for the Micro-mouse design owing to many advantages such as its programmability, which mean the ability to respond to the inputs and outputs of the system [4]. Stepper motors have input pins that allow current to move from a supply source into the coil windings of the motor. Pulsed waveforms in the correct pattern can be used to create the electromagnetic fields required to drive the motor. Figure 2 shows the block system diagram [5].
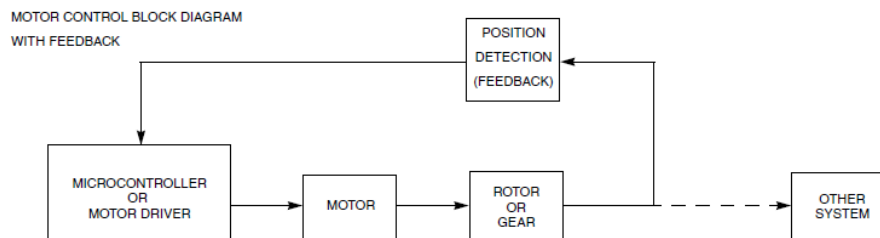
Figure 2: System with a Stepper Motor and Feedback

Each of these methods namely: Open Loop - Fixed Voltage, Open Loop-Fixed Current, Closed Loop Current Control; can be operated with a different granularity of voltage steps feed the motor windings [5-6]. The different granularity options available in this application noted here are: Full Step Mode (1/1 Step) Half Step Mode (1/2 Step)

which is divided into 1/4 Step, 1/8 Step,1/16 Step,1/32 Step, 1/64 Step as illustrated in table 1 and Figure 3.

Table 1: Steps of Stepper Motor [6]

stepSize value	Step Mode	Total of Steps Per Cycle
0	Full Step	4
1	Half Step	8
2	1/4 Step	16
3	1/8 Step	32
4	1/16 Step	64
5	1/32 Step	128
6	1/64 Step	256
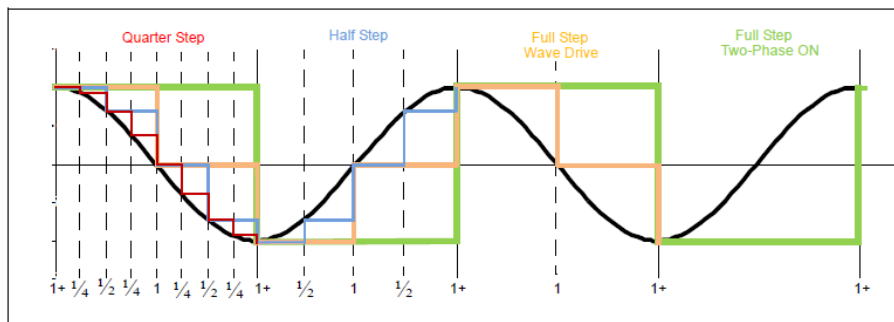
Figure 3: Pulsed Waveforms [6]

The majority of DC motors are operated in a closed loop, while DC stepper motor is operated in an open loop [7][11]. In order to control the stepper motor with Arduino, we choose the 4988 steeper motor version as a good stepper drive. It cannot control motor from Arduino as it required a minimum of 8-35 volts. Therefore, an external power supply is required. It is better to check the polarity in the manufacturer information and connect a decoupling capacitor to avoid any

unnecessary noise. The Arduino which uses 3.5-5v, which is not enough to operate the system. For this reason, a step-up convertor is needed. The program code is written using C++ language. Here motor winding equation is demonstrated.

$$V.u = R + L\,di \tag{1}$$

L = Motor resistance
R = Motor inductance
V = DC voltage
i = Instantaneous motor current
u = PWM duty cycle percentage

and motor transfer function is shown:

$$\frac{i(s)}{u(s)} = HM(S) = \frac{V}{L*S+R} = \frac{V/R}{\frac{L}{R}.S+1} \tag{2}$$

Each of the mechanical systems has a certain latency [9]. Therefore, Pulse Width Modulation (PWM) is a smart method to achieve the desired actual speed in a motor calibration shown in table 1. These pulses are generated a fixed frequency Instead of generating an analogue output signal.
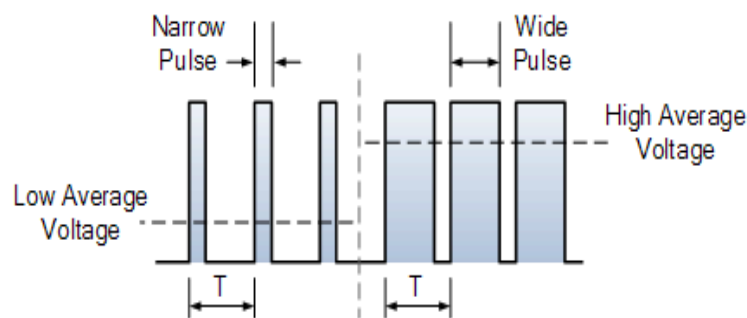
Figure 3: PWM method [10]

As seen from the above figure, motor speed depends on duty cycle (off and on switching). By using this technique, the Arduino board will be connected to the stepper motor board and the sensors. Infrared (IR) sensors are fast in measuring distances. That is to say, it has a high ability to receive and respond to changes according to their distance from the objects [7-8]. This type of sensor is available in both analogue and digital packages. The chosen micro-mouse sensor is Sharp GP2D 120 sensors; since this sensor could measure in an area of more than 25cm as demonstrates in Figure 4.
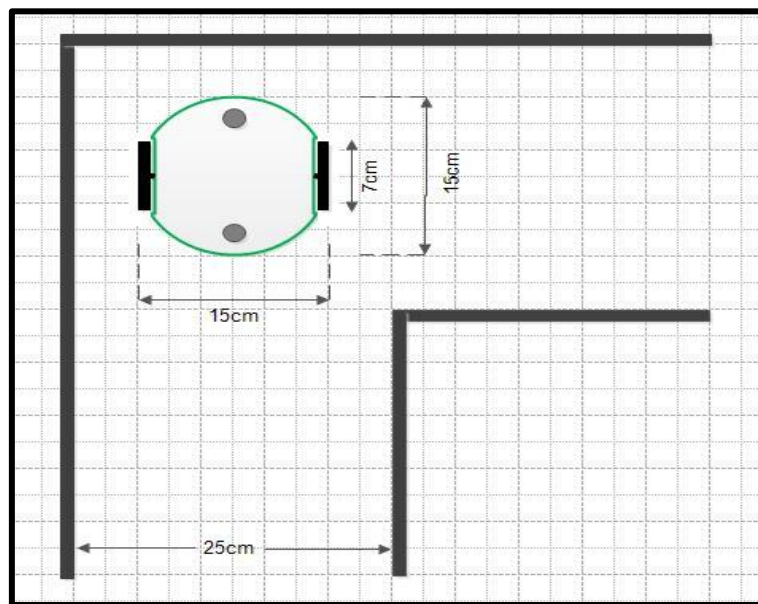
Figure 4:   Micro-Mouse Design

3. Performance Analysis

After completing the system of our micro-mouse and connected all the components with the Arduino board. The system would be as shown here in Figure 5.

Figure 5: Schematic Diagram Designed By Proteus Software

The adapted code was applied and our micro-mouse was traveling through the paths and faced some obstacles. This micro-mouse can either be controlled manually or automatically using Bluetooth technology. When the micro-mouse faced a certain object in the case of the automatic function, it turned back looking for another clear path until it reaches its target destination. When the wheels are moving around, it is noted that the same pulses will be applied to the stepper motors.

4. Conclusion

In conclusion, the design of Micro-Mouse is very useful for further advances where it becomes used in the most fields that require accuracy and speed to accomplish. In our robot design, we consider all

important aspects such as wheels, power source, motors, microcontroller, sensors and Bluetooth technology as well. This well-designed system enables us to gain the target and desired results in that the robotics were able to reach certain destinations which human beings cannot reach. It is hoped that this design could be improved by installing a camera and thus be used by government to save people during natural disasters such as earthquakes. It is also could be improved by using different type of wheels, so that it can go through difficult unpaved paths.

References

[1]   G. McComb, "Robot Builders Bonanza," McGraw-Hill Education, pp 190 - 210, 2001,   ISBN-10:0071362967. http://www.st.com/stonline/books/pdf/docs/1773.pdf

[2]   Max Embedded, "How To Build An IR Sensor - Maxembedded,"   2013, http://maxembedded.com/2013/08/how-to-build-an-ir-sensor/

[3]   Liptak, Bela G, "Instrument Engineers' Handbook: Process Control and Optimization. CRC Press. p. 2464, 2005.

[4]   R. Oberti *et al, "*Advances in robotic agriculture for crops," 2016.

[5]   W, Storr, "Pulse Width Modulation Used For Motor Control," (2013), [online] available from <http://www.electronics-tutorials.ws/blog/pulse-width-modulation.html> [30 March 2015]

[6]   J. Yan, "Research on STM32-based stepper motor control method for 3D printing [J]", *Manufacturing Automation*, vol. 43, no. 11, pp. 129-131, 2021.

[7]   Li, Y.; Ge, S.; Dai, S.; Zhao, L.; Yan, X.; Zheng, Y.; Shi, Y. Kinematic "Modeling of a Combined System of Multiple Mecanum-Wheeled Robots with Velocity Compensation Sensors," 2020.

[8]   Qu Jiwei, Guo Kangquan, Gao Hua et al., "Experimental study on cooperative control characteristics of driving and steering of agricultural flexible chassis based on PWM signal", *Transactions of the Chinese Society of Agricultural Engineering*, vol. 34, no. 7, pp. 7, 2018.

[9]   Pan Yue, Han Dongdong, Ji Shengyuan et al., "Modeling simulation and measurement analysis of active rear-wheel steering control strategy based on MATLAB," *Shanghai Automotive*, no. 3, pp. 5, 2020.

[10]   Qu Jiwei, Guo Kangquan, Gao Hua et al., "Experimental study on cooperative control characteristics of driving and steering of agricultural flexible chassis based on PWM signal," *Transactions of the Chinese Society of Agricultural Engineering*, vol. 34, no. 7, pp. 7, 2018.

[11]   Z. Hendzel, L. Rykała, "Description of kinematics of a wheeled mobile robot with mecanum wheels Model,". pp. 5–12, 2015.

Artificial Neural Network Estimation of the Effect of Varying Curing Conditions and Geopolymer Type on Compressive Strength

.

11

Artificial Neural Network Estimation of the Effect of Varying Curing Conditions and Geopolymer Type on Compressive Strength

Abdosalam ALNKAA
Department of Civil Engineering, Higher Institute of Science & Technology Yafren,
Libya

A B S T R A C T

To evaluate the compressive strength of three distinct geopolymer curing methods, artificial neural networks (ANN) have been developed in the current research. Chemical formulas are used in the development of ANN such as Al_2O_3, SiO_2, CaO, Fe_2O_3, MgO, Na_2O, K_2O, SO_3. Furthermore, three different type of curing were investigated to evaluate its effect on the compressive strength. Using an alkaline activator ($NaOH/Ma_2SiO_3=1$) and concentration of $NaOH(12M)$, waste activated alumina silicate may attain its ideal chemical composition, allowing for the production of high-quality paste. 52 input-target pairs were collected from the experiment and arbitrarily split into three groups: training, validation, and testing. Geopolymer strength is now available. The best performance was achieved by a system with three hidden layers, and its validation score was 0.3248, while the absolute percentage error was 0.025 and the root mean square error was 0.9895 during the training phase. In addition, the whole trained, verified, and tested network showed promising results in predicting the compressive strength of

geopolymers with reasonable execution in the considered range. In addition, ANN may be used to provide very accurate estimates of compressive strength, with projected values closely matching those obtained in experiments

Keywords: Geopolymer; Compressive strength; Artificial neural networks; Modeling

1. Introduction

In an effort to find a solution to the greenhouse problem and stabilize CO' emissions, 196 countries, including Turkey, signed the United Nations Convention on Greenhouse Gases in 1992 at the Rio Summit. The convention entered into effect in 1994. With these events, the international community attempts to create the means to reduce global warming by 2 ° C from now until 2100 [1]. Developing alternative cement materials, like as fly ash and crushed finely ground slag from a blast furnace, is one step toward realizing the goal of reducing CO_2 emissions. This approach has been shown to provide higher-quality results than OPC. A benefit of this waste material is that different forms of aluminosilicate (Al_2SiO_5) often emerge in fly ash, slag, and other industrial byproducts that might benefit from activation by an amorphous phase. Many activators, including sodium hydroxide, sodium silicate, potassium hydroxide, and potassium silicate, are available but not required. Alkali, especially Na or K, silicates help to create material with higher performance establishing these components as major industrial ingredients [2-6]. In any case, the low last expense and waste administration accomplishments could make up for this inadequacy. It has been calculated that increasing the quantity of silicon sodium-based soluble base enacting arrangement significantly improves the compressive quality of geopolymers formed from metal-kaolin. Increases in mechanical characteristics followed increases in volume of geopolymeric gel at a fixed nominal

density, leading to a more and more uniform microstructure. Alterations to the microstructure are traceable to the reaction's synthetic method, which takes place during the arrangement phase. It is known that geopolymers whose stability depends on alkali action exhibit tertiary differences [7–10]. It is important to tailor the properties of geopolymers to their intended use and the characteristics that will be required of them. The need to find suitable alternatives to Portland cement has led to the classification of geopolymer materials with a wide range of technical parameters and mechanical qualities. These characteristics are dependent on the combined influences of the Al_2O_3/SiO_2, Na_2O/Al_2O_3, Na_2O/H_2O, and $Na/[Na+K]$ molar proportions in the alumina silicate and antacid activators configurations [11]. Normal pozzolan, metakaolin, and pozzolanic byproducts such slags and fly powder react with very concentrated alkali hydroxide or silicate arrangement to form amorphous alumina silicate, discovered by Chelokovski in 1950 and later dubbed geopolymer by [12]. Excellent properties such as controllable setting time, moderate to high compressive strength, low shrinkage, and high sulfate resistance with minimal environmental impact make this material a strong contender for replacing conventional Portland cement in an effort to reduce greenhouse gas emissions in comparison to conventional concrete [13]. In recent years, artificial neural systems (ANNs) technology has been used to address a wide range of issues in civil engineering applications [14,15]. ANNs are a collection of massively parallel structures that solve complex problems through the cooperation of highly interconnected, yet fundamental processing components (or artificial neurons). " The ability of ANNs to learn precisely from data is their most valuable trait when applied to problems in civil engineering. Other is their appropriate (or mostly appropriate) responses to insufficient endeavors, their ability to glean information from outrageous or bad data, and their ability to get summing findings from the fresh circumstances. These features make ANNs a great tool for solving a wide range of civil engineering

problems, particularly in cases when there is either an overwhelming quantity of data or not enough of it [15]. Training ANNs frameworks on the results of a series of experiments using the material in question is the cornerstone of developing ANNs systems-based models for material behavior. If the results of the exploratory analysis provide relevant information about the material's behavior, then the resulting ANNs systems will be sufficiently informed to serve as a material model. These trained ANN systems wouldn't only be able to reproduce the trial findings, but also, because to their generalizability, get rather close to the outcomes in various studies [16]. Using artificial neural networks, researchers have produced predictions about the compressive strength of geopolymer concrete. Such as the work of Ozcan et al. [10]. Compressive strength predictions in silica fume concrete using artificial neural networks. Compressive strength of concrete with metakaolin and silica was predicted by ANNs [15]. In order to determine the compressive strength of concrete with fly ash particles, Topc-u and Sardemir [16] used ANNs. In addition, Bilim et al. also used ANNs. [17] research on the compressive strength of concrete made from ground granulated blast furnace slag. First, the system architecture needs to be designed, then initial weights and biases need to be determined, and finally, the best algorithm needs to be used to adjust these values throughout the learning process until they settle on the optimal values that will yield the desired results given the input design [18,19]. The back propagation approach is often used to train forward ANN by most experts [20]. After calculating the output from the input design with the current weights and biases, the method then employs a regressive algorithm to adjust the weights and biases. Changing the weights and biases one step at a time limits the execution capabilities, which usually refer to the square error or total square error. The system's ability to generalize and the learning process it employs are both sensitive to the data provided. Geopolymer mortar bond with w/c ratios of 0.33 was used to transport specimens for this investigation. After 28 days of curing, compressive

strength tests were performed on mortar that had been water-cured (WC), oven-cured (AC), or steam-cured (SC). ASTM standards were followed in making the mortar. The experimental data was used to train an ANN demonstration, which in turn was used to provide estimates of compressive strength.

2. Experimental program

2.1. Materials

In this experiment, three types of garbage were employed. The granulated blast furnace slag (GBFS) produced at Turkey's Ereli Iron-Steel Plant. GBFS had a fineness of about 4250 cm^2/g and a specific gravity of 2.81 g/cm^3. Atalaz, Zonguldak, Turkey-based thermal power plants supplied the Fly ash. The fineness is 6000 cm2/g, and the specific gravity is 2.39g/cm3. This is Class F fly ash. The finer ash will be produced by grinding the glass powder from the Los Angeles machine. Particles average about 13 m in diameter, have a fineness of 5320 cm2/g, and weigh 2.56 g/cm3. The GGBFS, FA, and GP chemical makeups are listed in Table 3. The alkaline solution phase used to activate the fly ash, GP, and GGBFS geopolymer concrete was a pre-blended mixture of sodium silicate (Na$_2$SiO$_3$) and 12 M sodium hydroxide (NaOH), with a 1:1 ratio of Na$_2$SiO$_3$ to NaOH. The aggregate in all of the mixtures was standard size as defined by TS EN196-1. For this, you may look at [Set imento Sanayi ve Ticaret A.. Trakya imento Fabrikas tarafndan üretilen]. The conventional aggregate mix, having a maximum particle size of 2 millimeters. Table 3 provides a comprehensive breakdown of concrete mix proportions for all mixtures.

Table 1: Fly ash, slag, and glass powder chemical composition

Oxide	FA %	GP %	GGDFS
SiO_2	61.81	36.7	36.7
Al_2O_3	9.54	5.2	5.2
Fe_2O_3	7.01	0.98	.98
CaO	1.77	32.61	32.61
MgO	2.56	10.12	10.12
SO_3	0.31	0.99	,99
K_2O	0.99	0.76	.76
Na_2O	2.43	0.42	0.42

2.2. Concrete mixes

This paper reports the results of a comprehensive experimental examination of the mechanical properties of geopolymer concrete mixes made using an aggregate of fly ash, glass powder, and slag, and cured under three distinct conditions. Two types of curing were discussed: (1) steam curing (SC) at 85 °C for 12 hours, followed by conventional curing at 20 ± 3 °C till testing; (2) the water curing (curing (WC); casted specimens were placed straight into a water tank after remolding and curing persisted until the age of test. In the third oven, the air-cured (AC) collection was restored in an oven at 65 °C for twenty-four hours, while the water curing temperature was maintained at 20 ± 2 °C. The examination will occur after the curing time. The samples were then demoulded after being kept in the molds for at least six hours. After being removed from their molds, the specimens were air-dried at 21°C and 70% humidity at the laboratory

facility until the day of the test. In this research, we looked into alkali activated mortars made from a mixture of slag, glass powder, and fly ash. Production conformance with TS-EN196-1 [25] has been achieved using the standard combination of GGBFS, GP, FA, water, NaOH, and Na_2SiO_3. It is well knowledge that the ratio of water to binder (W/B) affects several mortar characteristics. As a result, a fixed ratio of 0.33 between water and binder was chosen in compliance with TS-EN196-1 [25]. Coarse aggregates/binder ratio [A/B] is 1.23, while the Sodium Metasilicate/binder ratio [S/B] is 0.4. As part of the experiment, 5 different mixtures were used to create 425 different concrete samples. Table 2 lists the study's experimental variables. Compressive strength tests were performed on concrete samples made with different types of trash at 3, 7, and 28 days. Compressive strength testing was performed on concrete samples measuring 40mm x 40mm x 160mm after 3, 7, and 28 days of cure.

Table 2: Experimental study variables.

N0	1	2	3
Waste Aterial	FA	GGBFS	GP
Curing Conditions	Water-cured (WC)	Steam-cured (SC)	Oven air-cured (AC)

Table 3: Components of the concrete mix and their relative amounts (g/cm^3)

Mix No		S1	S2	S3	S4	S5
S gm	Na$_2$SiO$_3$	65	65	65	65	65
	NaOH	99	99	99	99	99
	water	104	104	104	104	104
A gm	Aggregate	1000	1000	1000	1000	1000
(B) gm	GGBF	810.5	0	567.35	688.93	688.93
	FA	0	810.5	121.58	121.58	0
	GP	0	0	121.58	0	121.58
Na$_2$SiO$_3$ gm		162	162	162	162	162
NaOH gm		162	162	162	162	162

2.3. Parameters and architecture of artificial neural networks

To handle complex problems, artificial neural networks (ANNs) rely on the collaboration of a large number of relatively simple computational elements organized in a hierarchical network (or synthetic neurons). Neural networks are oversimplified representations of the brain and nervous system. The capacity to learn from its surroundings and improve its performance thanks to this analysis is at the heart of every artificial neural network. An interactive method of adjusting synaptic weights and bias degree

allows the neural network to learn about its surroundings. The neurons in an artificial neural network (ANN) allow it to function as a parallel distributed processing device with an input layer, an output layer, and maybe additional hidden layers. Each neuron receives information from other neurons with varying weights and sends its own signal to other neurons using an activation function. The goal of any training set of rules is to maintain the excellent generality of the community while decreasing the MSE (mean square error) between expected and actual outputs. The data for the input-target pairs came from the experiments. The information has been gathered in such a way that its component elements come from a variety of places and in varying amounts. Materials as aluminosilicate sources were also investigated, as was the possibility of a resemblance between the gathered data.

This research makes use of a feed-forward architecture with three hidden layers and a back propagation training logarithmic. The back propagation calculation is a gradient drop system used to minimize the inaccuracy of a particular preparing design, and it is widely regarded as one of the best preparing calculations for the multilayer perceptron. The neuron outputs in the output layer and the hidden layer both used a logarithmic sigmoid function. Through a series of iterations, we were able to arrive at an acceptable value for both the model's momentum and learning rates. The pre-built model was simply tested with the input values, and the results closely matched the actual outcomes of the experiments. Experimentally made concrete mixtures amounted to 52, and their data was used in the presentation. Forty of the experimental data were used to build the model, six were used to put it to the test, and the remaining two were used to confirm it. Initiation work logarithmic sigmoid was also selected as the exchange function. In this study, we tested ANN examples for a range of neuron and layer counts. In honor of the top ANN demonstration, we capped the model's iterations at 5,000. As can be shown in Table 6, the

highest results for compressive strength were achieved by network designs with 3 hidden layers and 51 neurons.

Table 4: Variables that may be used as inputs and outputs for ANN

Variable	Range
SiO_2	295.65- 500.58
Al_2O_3	35.986- 76.95
Fe_2O_3	7.225- 15.256
CaO	13.77- 264.06
MgO	1.102- 82.458
SO_3	1.233- 8.019
K_2O	5.89- 41.04
Na_2O	1.037- 20.996
WC	1
SC	1

Table 5: Parameter settings in a model of a neural network

Parameters	ANN
Number of input layer units	9
Number of hidden layer	3
Number of output layer units	1

Table6: A review of ANNs for estimating compressive strength

| Designation	Number of neurons in hidden layers			Termination epoch
ANN	Hidden layer 1	Hidden layer 2	Hidden layer 3	20000
	31	17	3	

3. Results and discussion

Figure 1 shows how compressive strength varies with curing conditions. that compressive strength which cured by steam curing (SC) increases with the age of mortar gradually. This may due to the early strength gain by the specimens that GPM gained in the first 2 days. Figure 1(a) shows that over the first three days, there was a decline in compressive strength. and then increased up to 72 MPa at the age of 28 days. Therefore, fly ash is essential for achieving optimal water curing conditions while slag is being mixed.

Geopolymer mortar gained maximum strength in initial age, about 85% of 90 days strength can be achieved in 2 days with steam cured. In case of GPM mix which cured by SC, 7 days strength increased from 2% to 31%, while at 28 days strength increased between 2% to 30%, and at 90 days strength increased between 7% to 40% when compared to 2 days test results. Similarly, the GPM mix which cured by WC, 7 days strength increased between 81% to 178%, and at 28 days strength increased from 207% to 489%, while at 90 days strength increased from 318% to 1331% compared to 3 days strength.

The maximum compressive strength achieved by the specimens cured in steam is greater than that achieved by specimens treated in water or air. The loss of hydrating water due to evaporation is linked to this

problem. This results in a 12-hour total response time. Compressive strength development over time was studied for water-cured alkali activated mortars. All mortars have compressive strength ratings that rise as they cure. From the figures, it is clear that fly ash, slag, and glass powder undergo a negligible Geopolymeric reaction during water curing. Similar findings have been found in the past while studying Class F fly ash systems that were alkali activated. Mortar with a high final strength cannot be produced at room temperature because the activation processes do not proceed quickly enough. The reactions can only be sped up by increasing the temperature. In addition, the high Ca and Al_2O_3 content of the M1 and M11 combination increased its compressive strength. Compressive strength was also improved by adding GGBS to GP, despite GP's lower Al_2O_3 content. These results show that Ca and Al_2O_3 affected the mortar's compressive strength.
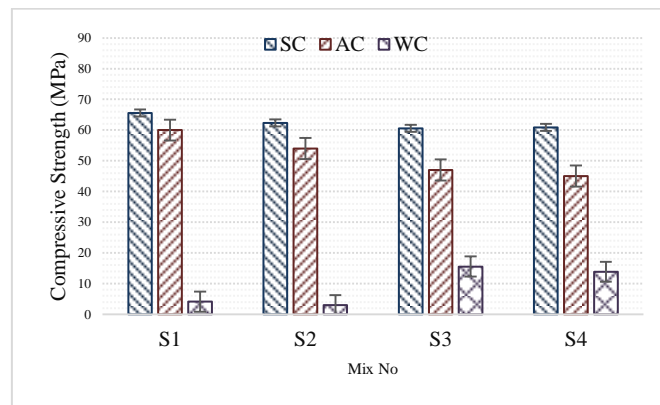
(a) steam-cured
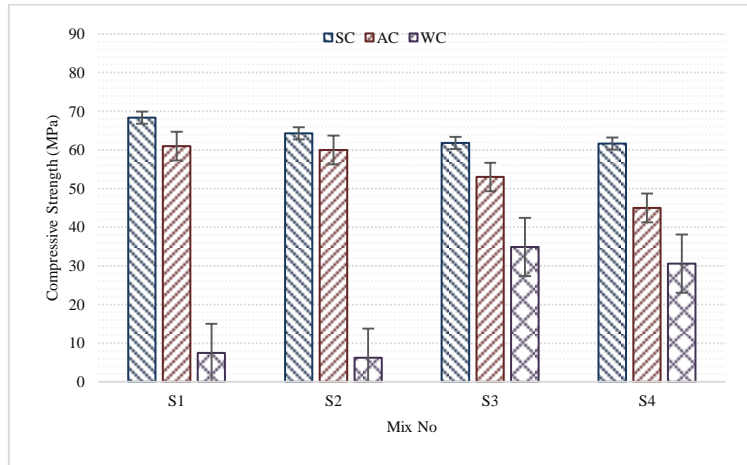
(b) Air oven-cured
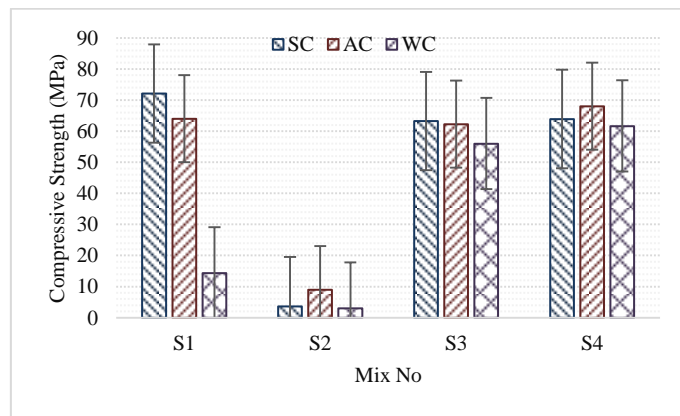
(c) water-cured

Fig. 1: Changes in compressive strength over time as a function of mortar mixture component ratio and curing condition.

Table 7: The relative amounts of oxides in slag, glass powder, and fly ash

Chemical compounds	Mix No				
	S1	S2	S3	S4	S5
SiO_2	295.65	500.58	370.47	326.54	339.73
CaO	264.06	13.77	200.90	226.65	238.44
Al_2O_3	42.12	76.95	42.95	47.37	37.73
Fe_2O_3	7.94	56.70	14.54	15.26	7.23
MgO	82.46	20.74	62.38	73.24	71.64
Na_2O	3.40	19.68	21.00	5.85	18.55
K_2O	6.16	8.02	6.17	6.44	5.89
SO_3	8.02	2.51	6.08	7.20	6.91
SiO_2/Al_2O_3	7.02	6.51	8.62	6.89	9.00
CaO/Al_2O_3	6.27	0.18	4.68	4.79	6.32

Diagrammatically contrast the relative amounts of the three most abundant oxides in GGBS, GP, and FA. Mixes S1 and S5 had the most strength, whereas mix S2 had the weakest. As can be seen in Fig. 1, mix S1 includes more lime than mix 2, leading to greater strength, although mix 2 has a larger SiO_2 concentration and a higher SiO_2/Al_2O_3 ratio, coming in at 6.51. (Table 7). The SiO_2/Al_2O_3 ratio for S1 is 7.02, whereas it is 6.51 for S2. Table 7 shows that the CaO_2/Al_2O_3 ratio is lowest in the mix S2, which includes 100% FA, and this may explain why this mixture has the lowest compressive strength. Also crucial is the presence of calcium hydroxide, or CaO

(Ca(OH)$_2$). It regulates the strength and soundness of the fabric, but too much lime (CaO) will make it swell and fall apart. Mortar's hardening process boils down to an abundance of lime (CaO) [7].

3.1. Estimation of Compressive Strength Using ANN

Data collected throughout the experiment has been evaluated using ANN. The model was created using the actual value of compressive strength acquired by crushing concrete cubes as the aim, with the output data serving as input to the ANN model.
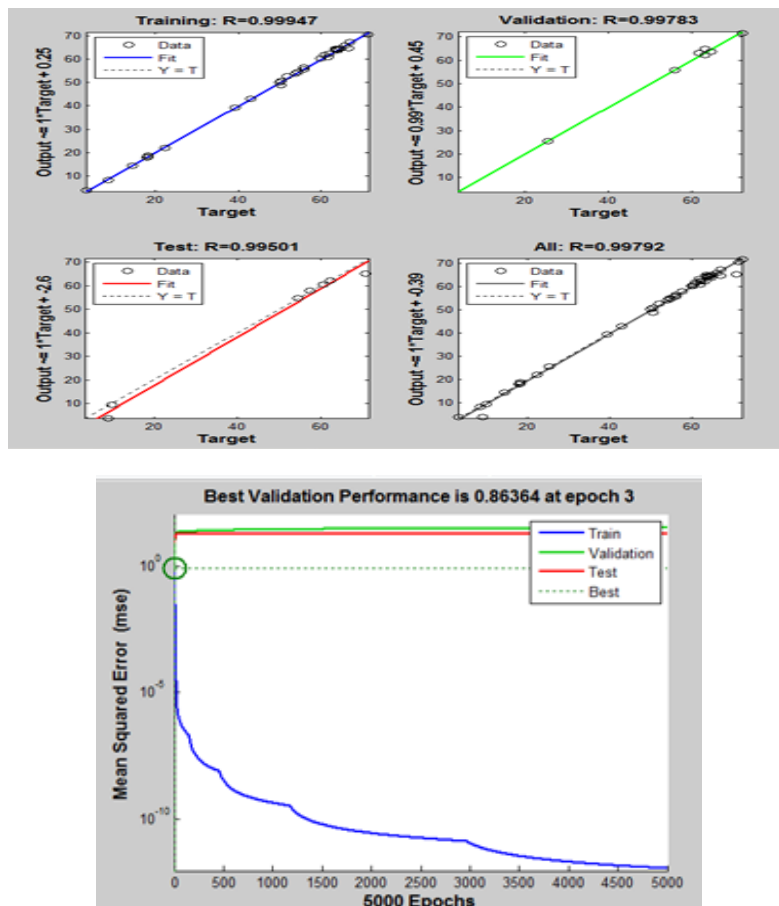

Fig. 2: Values of ANN model regression.

The estimated compressive strength has a mean squared error of 0.22389. The relapse values obtained at the end of the ANN training are shown in Fig. 2. Forty mixtures were selected to recreate the ANN show, and the predictive power of the model was examined. The model proved to be highly useful in estimating compressive strength values, as seen in Fig. 3. This is another proof that the ANN structure was well presented.
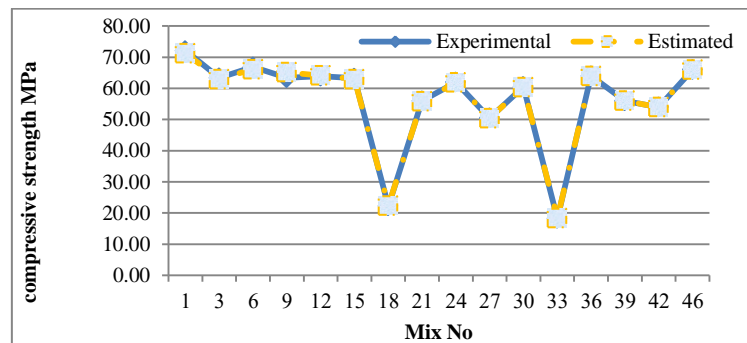

Fig. 3: Compressive strength data are compared between experiments and estimates.

4. Conclusions

This research presented an alternative, high-quality approach to determining the compressive strength of several geopolymers. In order to forecast compressive strength estimates of different geopolymers with three cured state, an ANN method display was provided. The suggested model relied on empirical data collected via experiments. This research's model was meant to be novel in terms of its use of neurons in 3-layer feed forward-back propagation systems and its approach to cutting off the training phase. The outcomes obtained from ANN display demonstrated sensible concurrence with gathered test results from the experimental test when the preparation stage was halted when the base level of square error was gotten. The factual estimations of $R2$ uncovered this circumstance. The ANN model was

discovered to be a viable alternative approach for evaluating geopolymer compressive strength. Thus, it was shown that ANN display can be relied upon to provide compressive strength predictions of different geopolymers in a very short amount of time with low error rates.

References

[1]   Yamin, F. and J. Depledge, The international climate change regime: a guide to rules, institutions and procedures. 2004: Cambridge University Press.

[2]   Wang, S.-D., et al., Alkali-activated slag cement and concrete: a review of properties and problems. Advances in cement research, 1995. 7(27): p. 93-102.

[3]   Yang, K.-H., et al., Properties of cementless mortars activated by sodium silicate. Construction and Building Materials, 2008. 22(9): p. 1981-1989.

[4]   Fernández-Jiménez, A. and A. Palomo, Composition and microstructure of alkali activated fly ash binder: Effect of the activator. Cement and concrete research, 2005. 35(10): p. 1984-1992

[5]   5.   Palomo, A., M. Grutzeck, and M. Blanco, Alkali-activated fly ashes: a cement for the future. Cement and concrete research, 1999. 29(8): p. 1323-1329.

[6]   6.   Provis, J., Activating solution chemistry for geopolymers, in Geopolymers. 2009, Elsevier. p. 50-71..

[7]   Duxson, S.W. Mallicoat, G.C. Lukey, W.M. Kriven, J.S.J. van Deventer, The effect of alkali and Si/Al ratio on the development of mechanical properties of metakaolin-based geopolymers, Colloids and Surfaces A: Physicochemical and Engineering Aspects 292 (2007) 8–20.

[8]   F. Pacheco-Torgal, D. Moura, Yining Ding, S. Jalali, Composition, strength and workability of alkali-activated metakaolin based mor- tars, Construction and Building Materials 25 (2011) 3732–3745.

[9]   J. He, J. Zhang, Y. Yu, G. Zhang, The strength and microstructure of two geopolymers derived from metakaolin and red mud-fly ash admixture: a comparative study, Construction and Building Materi- als 30 (2012) 80–91.

[10]   A. Poulesquen, F. Frizon, D. Lambertin, Rheological behavior of alkali-activated metakaolin during geopolymerization, Journal of Non-Crystalline Solids 357 (2011) 3565–3571.

[11]   Barbosa, V.F.F., MacKenzie, K.J.D., and Thaumaturgo, C., "Synthesis and characterisation of aterials based on inorganic polymers of alumina and silica: sodium polysialate polymers",International Journal of Inorganic Materials, Vol. 2, pp. 309-317, 2000

[12]   10.   Devidovits, J., "Geopolymers: inorganic polymeric new materials". Journal of Thermal Analysis,Vol. 37 (1991), 1633-1656

[13]   Devidovits, J., "Properties of geopolymer cements". First International Conference on AlkaliCements Concretes, Kiev, Ukrain, 1994

[14]   F.Öˇzcan, C.D. Atis-, O. Karahan, E. Uncuoˇ glu, H.Tanyildizi, Comparison of artificial neural network and fuzzy logic model for prediction of long-term compressive strength of silica fume concrete, Advances in Engineering Software 40(2009)856–863

[15] M.Sarıdemir, Prediction of compressive strength of concretes containing metakaolin and silica fume by artificial neural networks, Advances in Engineering Software 4 0(2009)350–355

[16] I.B.Topc-u, M.Sarıdemir, Prediction of compressive strength of concrete containing fly ash using artificial neural networks and fuzzy logic, Computational Materials Science 41(2008)305–311

[17] C.Bilim,C.D.Atis-, H.Tanyildizi, O.Karahan,P predicting the compressive strength of ground granulated blast furnace slag concrete sing artificial neural network ,Advances in Engineering Soft- ware 40(2009)334–340.

[18] Topalov, A. V., Kayanak, O., "Neural network modelling and control of cement mills using avariable structure systems theory based on-line learning mechanism", Journal of Process Control,Vol. 14, 581-589, 2004

[19] Topcu, I. B., Saridemir, M., "Prediction of compressive strength of concrete containing fly ash using artificial neural networks and fuzzy logic", Computational Materials Science, Vol. 41, 305-311, 2008

[20] Mandal, A., Roy, P., "Modeling the compressive strength of molasses-cement sand system using design of experiments and back propagation neural network", Journal of Materials Processing Technology, Vol. 180, 167-173, 2006

[21] TS-EN196-1: Methods of Testing Cement – Part 1: Strength Determination, Ankara: TSE-Turkish Standards Institution, 2009.